UNIVERSITÉ DE STRASBOURG

École doctorale
Physique, chimie-physique
ED 182
Université de Strasbourg

ÉCOLE DOCTORALE 182

Institut de Physique et Chimie des Matériaux de Strasbourg

THÈSE présentée par :

Icare MORROT-WOISARD

soutenue le : **26 Septembre 2025**

pour obtenir le grade de : **Docteur de l'université de Strasbourg**

Discipline/ Spécialité : Matière condensée et nano physique

TITRE de la thèse

First-principles modeling of carbon-based materials for electronic-magnetic applications

THÈSE dirigée par :

Mr **Mauro BOERO**	Directeur de Recherches, ICube – Université de Strasbourg
Mr **Guido ORI**	Chargé de Recherches, IPCMS – Université de Strasbourg

RAPPORTEURES :

Mme **Émilie GAUDRY**	Professeure des universités, IJL – Université de Lorraine
Mme **Marie-Pierre GAIGEOT**	Professeure des universités, lambe – Université d'Evry Val d'Essonne

---

AUTRES MEMBRES DU JURY :

Mr **Philippe POULIGUEN**	Responsable Innovation pour le pôle ATS, AID
Mr **Fabio PIETRUCCI**	Maîtres de conférence, IMPMC – Sorbonne Université
Mr **Nicolas VUKADINOVIC**	Expert Dassault Aviation en Électromagnétisme
Mr **Paul-Antoine HERVIEUX**	Professeur des universités, IPCMS – Université de Strasbourg (Président du jury)

Abstract

This thesis contributes to the development of carbon-based nanomaterials for electromagnetic wave absorption in the microwave frequency range, with applications in electronics and aeronautics in the context of the joint laboratory MOLIERE. The central question driving this work is whether current simulation tools and computational technologies have reach a sufficient level to predict and understand real-world performance of these materials at the nanoscale.

To address this issue, we focused on three representative systems: cobalt-decorated carbon nanotubes (CNTs), CNTs interacting with the polymer PMMA, and reduced graphene oxide (rGO). These reference systems, chosen for their scientific and industrial relevance, served as case studies to probe the interaction mechanisms at the atomic and electronic levels.

We make extensive use of first principles molecular dynamics (FPMD) simulations to describe atomic, electronic, and vibrational behavior of these systems, with te purpose of extracting macroscopic observables and useful guidelines for practical synthesis and realization. From the generated trajectories, we applied complementary analytical methods to deepen our understanding of structural organization and its influence on electromagnetic properties. The fluctuation-dissipation theorem was one of the useful tools to extract dielectric and electromagnetic responses, while the maximally localized Wannier functions (MLWF) provided insights into local dipole moments. Furthermore, perturbative approaches such as dynamical matrix analysis allowed us to access and visualize vibrational modes.

In the case of cobalt-decorated CNTs, we observed Co aggrgates undergoing migration along the nanotube surface, resulting in modifications of the local dipole moment and altered bonding patterns. This suggested to include CNTs in a medium prone to prevent this tupe of uncontrolled diffusion. To this aim, we moved to a system composed of CNTs and a polymer (specifically a PMMA one) to mimic what occurs if CNTs are inserted in a ploymer matrix. For the CNT–PMMA interface, studied to provide a rationale for the mutual interaction between the two building blocks, we highlighted deformation phenomena such as ovalization and intertube distance oscillations, affecting both phonon behavior and EM wave absorption modes. Finally, in the reduced graphene, the last system brought to our attention by experimental coworkers, we demonstrated that reduction of graphene significantly alters both the atomic level topology and the electronic structure, with strong implications for dipole dynamics and electromagnetic response.

Our multi-method approach enabled the identification of key physical features, fundamental atomic interactions, structural reorganization, charge redistribution, and vibrational coupling—underpinning the macroscopic behavior of these materials. These insights serve as a first pioneering step toward the understanding of the microscopic origin of microwave absorption and pave the route to future multi-scale simulation strategies.

Keywords : First-principles molecular dynamics, perturbative approach, dynamical matrix, vibrational properties, electromagnetic response, dielectric function

Résumé

Cette thèse s'inscrit dans le développement de nanomatériaux à base de carbone pour l'absorption des ondes électromagnétiques dans la gamme des micro-ondes, en lien avec des applications en électronique et en aéronautique, dans le cadre du laboratoire commun MOLIERE. La question centrale ayant guidé ce travail est la suivante : disposons-nous aujourd'hui des outils de simulation et de la technologie nécessaires pour prédire et comprendre les performances réelles de ces matériaux à l'échelle nanométrique ?

Pour y répondre, nous avons étudié trois systèmes représentatifs : des nanotubes de carbone (CNT) décorés de cobalt, des CNT en interaction avec le polymère PMMA, et de l'oxyde de graphène réduit (rGO). Ces systèmes, choisis pour leur pertinence scientifique et industrielle, ont permis d'explorer les mécanismes d'interaction à l'échelle atomique et électronique.

Nous avons utilisé des simulations ab initio via la dynamique moléculaire à premiers principes (FPMD) pour capturer les comportements atomiques, électroniques et vibrationnels. À partir des trajectoires obtenues, nous avons appliqué plusieurs méthodes complémentaires : le théorème fluctuation-dissipation pour obtenir les réponses diélectriques et électromagnétiques, les fonctions de Wannier maximales (MLWF) pour analyser le moment dipolaire local, et des approches perturbatives par matrices dynamiques pour accéder aux modes vibrationnels et les visualiser.

Pour les CNT décorés au cobalt, nous avons observé un déplacement des atomes de cobalt à la surface des nanotubes, modifiant les moments dipolaires locaux et la topologie des liaisons. L'interaction entre CNT et PMMA a mis en évidence des déformations telles que l'ovalisation et des oscillations de distance, influençant les phonons et les modes d'absorption électromagnétique. Concernant le graphène réduit, nous avons démontré que la réduction modifie significativement la structure et la distribution électronique, avec un impact fort sur la dynamique dipolaire.

Notre approche multi-méthode a permis d'identifier les phénomènes physiques clés – interactions atomiques, réorganisation structurelle, redistribution de charge, couplage vibrationnel – qui sous-tendent le comportement macroscopique de ces matériaux. Ces résultats posent les bases nécessaires pour une meilleure compréhension des mécanismes microscopiques de l'absorption dans la gamme des micro-ondes, et ouvrent la voie à des stratégies de simulation multi-échelle futures.

Mots clés : Dynamique moleculaire ab initio, méthode perturbative, matrice dynamique, propriétés vibrationnelles, réponse électromagnétiques,fonction diélectrique

Publications[1] **:**

[1] C. Massobrio, I.A. Essomba, M. Boero, C. Diarra, M. Guerboub, K. Ishisone, A. Lambrecht, E. Martin, **I. Morrot-Woisard**, G. Ori, C. Tugène, S.D. Wansi Wendji 'On the actual difference between the Nosé and the Nosé-Hoover thermostats: a

[1] A complete list of scientific contributions, including published articles, preprints, and works in preparation, is available at the end of this thesis on page 115

critical review of canonical temperature control by molecular dynamics' *Phys. Status Solidi B Basic Res.* **(2023)**. DOI: 10.1002/pssb.202300209; HAL: hal-04280276v1.

[2] **I. Morrot-Woisard**, E.K. Nguyen, N. Vukadinovic, and M. Boero. 'Structural, electronic and dielectric properties of carbon nanotubes interacting with Co nanoclusters.' *Carbon Trends* 17, 100410 **(2024)**. DOI: 10.1016/j.cartre.2024.100410; HAL: .

Contents

List of Figures

List of Tables

Acknowledgement

This thesis was conducted at the Institut de Physique et Chimie des Matériaux de Strasbourg (IPCMS – UMR 7504, CNRS) of the University of Strasbourg, France, under the direction of Mauro BOERO (Laboratoire des Sciences de l'Ingénieur, Informatique et Imagerie, ICUBE – UMR 7357) and in co-supervision with Guido ORI (IPCMS) from October 1, 2022 to September 26, 2025.
First and foremost, I would like to express my sincere gratitude to my supervisors for the trust they placed in me by entrusting me with this doctoral project, as well as for their constant support throughout its development. Their guidance, insightful discussions, and unwavering encouragement have been invaluable in helping me navigate the various stages of this thesis and bring it to completion.
I would also like to extend my warmest thanks to Christophe LEFEVRE and Nicolas VUKADINOVIC, whose support and involvement throughout the duration of this work were greatly appreciated. Their technical advice and human perspective have been of great help on numerous occasions, and I am truly grateful for their contribution.
I would like to thank the members of the AdynMAT consortium, which includes my supervisors as well as Evelyne MARTIN and Carlo MASSOBRIO. I am equally thankful to all the PhD students who have been part of this collaborative network, Dr. S. D. WANSI WENDJI, Dr. K. ISHISHONE, Dr. C. DIARRA and Dr. A LAMBRECHT. The discussions and scientific exchanges during the consortium meetings greatly enriched my thinking and significantly contributed to the development of this thesis.
I would like to express my sincere thanks to my office colleagues, Arnaud JABLONSKI and Lamiae EL KHABCHI, with whom I maintained a friendly and supportive relationship throughout my PhD, despite the differences in our research areas. More generally, I am also grateful to all my colleagues at DCMI for their kindness and collegial spirit. These positive and respectful interactions helped create a pleasant and serene working environment, which greatly contributed to the progress of my research.
This thesis could not have come to fruition without the establishment of the joint research laboratory MOLIERE, made possible by the collaboration of several key partners, including IJL, Dassault Aviation, the AID, and IPCMS. I would like to warmly thank all the stakeholders who contributed to making this project possible. I would also like to extend my special thanks to Maria Jose VAZQUEZ BERNARDEZ, my colleague at DCMI and an active member of the joint laboratory. Throughout my Ph.D., she accompanied me to various seminars and meetings related to the laboratory. Her constant presence during these trips was invaluable and allowed me to approach them with greater peace of mind.
I would also like to express my sincere gratitude to my family based in Strasbourg, who did everything they could to support me throughout these years. I am especially thankful to my aunt and uncle, Marie-Pierre and Hubert, as well as to my cousin, Lucile, for their kindness, availability, and unwavering support. Their presence offered me comfort and encouragement.
And finally, I would like to dedicate a few words to the people to whom I dedicate this thesis. They may not have contributed directly to the scientific content of this work, and at times I may have been distant during the intense three years of this Ph.D. journey. Yet,

it is they who have accompanied me throughout my academic path, from its beginnings to its culmination in this thesis. I wish to begin by acknowledging my mother, Anne WOISARD, my brothers and sister, Donald, Volnay, Mélisande, Ezio, whose unwavering support has meant everything. I also want to thank the friends who remained in my thoughts, even if life sometimes distanced us, Martin, Pierre, Charles, Adrien, Pierro, Ciara. Each of you has left a mark on this journey. My studies and this thesis have seen both highs and lows, but you have always been there. Thank you.

List of Acronyms

AIMD	Ab initio Molecular Dynamics
BLYP	Becke, Lee, Yang and Parr
BO	Born-Oppenheimer
BOMD	Born-Oppenheimer Molecular Dynamic at 300 K after full CMD
CMD	Classical Molecular Dynamics
CNT	Carbon NanoTube
CPMD	Car-Parrinello Molecular Dynamics
DFT	Density Functional Theory
DOS	Density Of State
EM	Electromagnetic
EMI	Electromagnetic Interference
EMW	Electromagnetic Wave
FPMD	First-Principles Molecular Dynamics
FT	Fourier transform
GGA	Generalized Gradient Approximation
GO	Graphen oxide
HF	Hartree-Fock
HPC	High performance computing
KS	Khon-Sham
LDA	Local Density Approximation
LSD	Local Spin Density Approximation
MC	Monte Carlo
MD	Molecular Dynamics
MEM	maximum entropy method
ML	Machine Learning
MLIP	Machine Learning Inter-atomic Potential
MLWF	Maximally-localized Wannier Functions
MSD	Mean-Square Displacement
MW	Microwave
NP	Nano Particle
PBCs	Periodic Boundary Conditions
PBE	Perdew-Burke-Ernzerhof
PBE0	Hybrid 0.75 PBE exchange + 0.25 Hartree-Fock exchange
PES	potential energy surface
PMMA	poly(methyl methacrylate)
PP	Pseudo-Potentials
PW	Plane Waves
rGO	reduced Graphene oxide
TM	Troullier and Martins
WF	Wannier function
WFC	Wannier function center
XC	Exchange-Correlation

Chapter 1

General Introduction

Summary

This chapter is dedicated to a survey of the present state of the art in the field of materials suitable for the realization of microwave absorption systems. The general framework and major motivation are applications in electronics, telecommunication and aeronautics, where problems related to electromagnetic shielding and absoprtion represent forefront issues in terms of safety and protection against undesired radiation. Keeping this overall scenario in mind, I start this Ph. D. dissertation with a brief introduction on developments of this field. The I shall move to a recall of the microwave absorption mechanism, where magnetic and/or dielectric properties are the dominant features, often difficult to disentangle into exclusively electric and exclusively magnetic. Some promising materials have been studied worldwide, with more or less promising performances often depending on a number of factors not always easy to identify, such as chemical composition, nature of the constituent building blocks, atomic-level interactions or synthesis and preparation conditions which determine the macroscopic properties and electromagnetic response. Among the materials proposed over the years, I shall focus carbon-based systems, being the most promising, economically affordable and with moderate environmental impact. This chapter will terminate with a brief description of different approaches suitable to model such systems in a context of computational science, being this specific aspect the main objective and central core of this research work.

1.1 Context

Since their discovery, during the XIX century, electromagnetic waves (EMWs) have been widely used in a wealth of fields including (but not limited to) telecommunication, electronics, medical diagnostics, radar detection and information processing [8]. Such a rich scenario implies a continuously growing technology to generate, absorb and handle EMWs. In the textbook example of telecommunication, the range of frequencies used, referred to as *band*, correspond to an interval between approximately 3 and 300 GHz, generally indicated as *microwave* region. Having devices and instruments able to operate in the microwave domain was the major motivation that boosted the field in material science toward this direction. Depending on the feature targeted, the search for suitable stand-alone materials or a combination of them able to produce a composed system with the desired properties is becoming a hot topic for electromagnetic shields or absorbers able to protect electronic devices, to reduce human exposure against unwanted radiations, to reduce electromagnetic interferences and to ensure stealth properties.

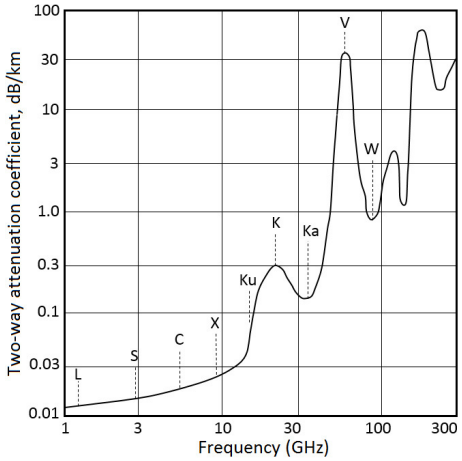

Figure 1.1. Atmospheric absorption spectra in the microwave range.[1]

For telecommunication, low Earth orbit (LEO) satellite systems, aircrafts, and radars the EMWs frequencies typically used are the Ku-band (12-18 GHz) and the Ka-band (27-40 GHz). The K band is generally avoided because water, which is omnipresent on the planet and in the atmosphere, has a resonance peak at 22 GHz as shown in 1.1, and thus has a high absorption rate that jeopardizes communication and detection. Lower frequency bands are also used in military applications from 100 MHz, the so-called Very High Frequency (VHF) band up to the X-band (8-12 GHz), although the military band of interest is rapidly evolving.

1.2 Microwave absorption

On a general ground, the interaction of EMWs with matter results in three different interactions, namely, an incident EMW can be reflected back into the incident medium, absorbed by the matter, or transmitted across it. These three processes can occur simultaneously, and the percentages of reflected, adsorbed, and transmitted EMW depend on the nature and composition of the material interacting with the incoming EMW.

In this thesis, I am specifically interested in absorption and materials prone to maximize or realize exclusively this type of interaction. To this aim, the targeted materials should be able to realize some fundamental physical characteristics such as low surface reflection and absorption enhanced in a specific selected frequency range to prevent interference and

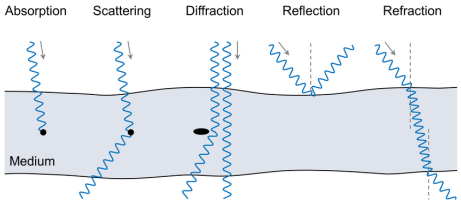

Figure 1.2. Schematic representation of the different possible interactions between light and matter as summarized in the text. Image taken from [2].

possible damage compromising, for instance, the safety of air navigation or the electronic devices operation.

1.2.1 Microwave absorption mechanism

Most of the information reported in this section can be found in major academic lectures and books [9–11].
The response of a given material to an incident EMW has been the target of intense research (and debate) since the very beginning of electromagnetism. Leaving aside recent development not related to the main subject of our research, such as all the quantum electrodynamics (QED) field, we restrict our survey to the basic theory directly related to the response of a condensed matter system to an electromagnetic field signal intended as a classical field. In this respect, our fundamental knowledge of electromagnetic (EM) absorption could be summarized as, in a lossy dispersive media, the energy transfer between the incoming EM field and the material. This process is mathematically described, in a classical electrodynamics context, by the Poynting theorem which is basically an extension of the energy conservation theorem well known in classical dynamics and analytical mechanics. The Poynting theorem is directly derived from the Maxwell-Ampere and the Maxwell-Faraday equations of the energy current $(\vec{E}.\vec{j})$ which has the physical dimensions of a power per unit-volume. In a non-magnetic media the related equation reads:

$$\frac{\partial}{\partial t}\frac{\epsilon_0}{2}[\vec{E}+c^2\vec{B}] = -\vec{E}.\vec{j} - \vec{\nabla}.(\epsilon_0 c^2 \vec{E}\times\vec{B}) - \vec{E}.\frac{\partial \vec{P}}{\partial t} \tag{1.1}$$

where the term on the left of the equation is the time derivative of the electromagnetic energy per unit volume. The first term on the second member of this same equation is called Joule heating and it represents the absorbed power per unit volume; I wish to remind that if $\vec{E}.\vec{j}$ is negative in a specific region, then that region acts as a source of energy. The second term of the second member is the power radiated through the surface that encloses the considered volume, and the last term on the same side is the power needed to modify the polarization. Since we are looking for materials having industrial applications, the heating part has to be minimized. This means that we want the last term to be the dominant one. A reformulation of the above equation useful for materials science and satisfying the requirements stated above, averaging on time and polarization, reads :

$$\langle \vec{E}.\frac{\partial \vec{P}}{\partial t}\rangle = \frac{1}{2}\epsilon_0\omega\chi''|\vec{E}|^2 \tag{1.2}$$

which means that the power needed to modify the polarization per volume is linearly dependent on the imaginary part of the complex dielectric susceptibility χ''. A similar conclusion could be done considering a magnetic medium, and in this case the power needed to modify the magnetization per volume is linearly dependent on the imaginary part of the complex magnetic susceptibility χ''_m . With this reformulation, we get two fundamental quantities that describe the EMW-matter interaction, (i) the dielectric permittivity $\epsilon(\omega) = \epsilon'(\omega) + i\epsilon''(\omega)$ and and the magnetic permeability $\mu(\omega) = \mu'(\omega) + i\mu''(\omega)$.

The real part ϵ' (μ') is associated to energy storage and the imaginary part ϵ'' (μ'') is associated to the energy loss resulting from conduction, resonance and relaxation mechanisms. In the case of magnetic permeability of ferromagnets, absorption is mainly due to internal resonances (domain wall resonance, natural gyromagnetic resonance) and eddy-current losses (electrical conductors) that occur in the microwave range. The resonance frequencies and the permeability level at low frequency are linked by the Snoek limit [12]. In the case of permittivity, in the low microwave frequency absorption range, dipolar polarization mechanisms are the predominant feature, while ionic polarization are weak, whereas in the high microwave frequency absorption range ionic polarization is the main absorption mechanism while dipolar polarization is weak [13], as shown in Fig. 1.3.

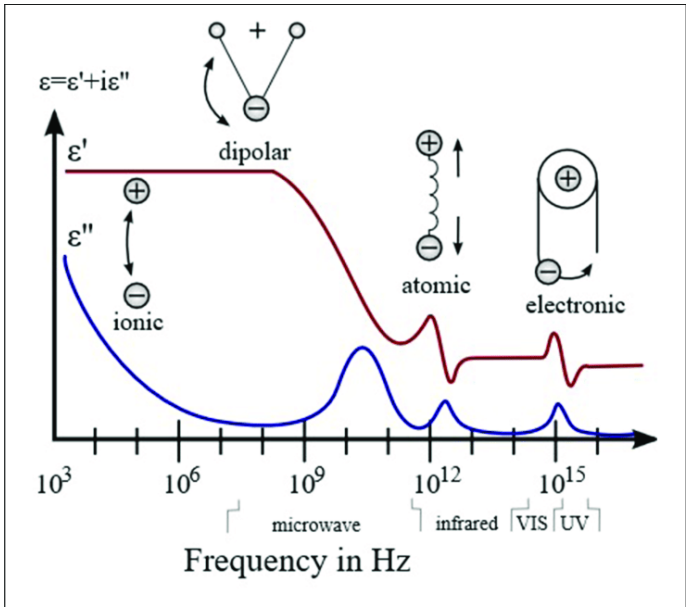

Figure 1.3. Schematic representation of the imaginary (ϵ") and real (ϵ') components of the dielectric function vs. frequency. This simple textbook example shows the predominance of different relaxation mechanism as a function of the frequency considered.

The dielectric loss tangent of a material provides an important absorption characteristic and is defined as :

$$\tan\delta = \frac{\epsilon''}{\epsilon'} \tag{1.3}$$

On a general ground, the higher the dielectric loss tangent for a given frequency, the higher the absorbing characteristics of the system. This parameters will be useful in Chapter 3 to provide a rationale for the outcome of our simulation and will be recalled in the ongoing discussion whenever needed to draw useful conclusions from the raw simulation data.

1.3 Materials for microwave absorption

Electronic devices in aeronautics applications, where electronic equipments are exposed to incoming radiation of various nature, either natural such as cosmic radiation and terrestrial radionuclides or due to human activities at ground level or via satellites, represent a main motivation pushing research worldwide toward suitable materials suitable to respond in a desired way to incoming electromagnetic waves. Attempts at removing or mitigate electromagnetic interference (EMI) have becoming a forefront activity, giving a renovated impulse to the search for materials with desired and tunable characteristic able to shield or deflect incoming radiation[14, 15]. In this general framework, the wide range of possible systems that could potentially provide an answer to the requirements mentioned has been

narrowed down to those granting accessible chemical elements, affordable realization costs and sustainability.

1.3.1 A brief overview

In the framework of aeronautics applications, a privileged system consists of a polymeric matrix loaded with absorbing materials as micro or nanometer-sized particles. This combination and the resulting fabrication technique has several advantage. One of them is that it can be used as paint to coat complex shaped objects. The choice of absorbing particles is guided by the targeted operating frequency band. Several families of materials have been explored as candidates for absorbing particles among them; ferro- or ferrimagnetic phases, carbon-based constituents and to a lesser degree, semi-conductor media. Magnetic materials For the case of magnetic particles, ferromagnetic alloys and ferrimagnetic oxydes have been extensively investigated. Good candidates to be used as a filler in a polymer matrix are spinel ferrites of the type indicated in the central circle of Fig. 1.4, which are able to enhance the absorption characteristic. A peculiar case having received attention is the one in which self-assembly properties at the molecular level give rise to the conglomerates termed nano-flakes[16]. Such a shape is generally a two-dimensional arrangement of atoms that can induce precession of the magnetization with a net effect of enhancing magnetization properties[17]. This has stimulated researchers to investigate the properties of metallic magnetic materials able to self-organize into nano-flake shape. I recall that metallic magnetic materials are generally characterized by a high permeability, phenomenologically is well described by the Snoek law, but, as a drawback, it is nearly impossible to increase simultaneously permeability and resonance frequency. This physical limitation could be overcome by coupling the efficiency of this class of materials with different compounds constitute of chemically different atoms, resulting in *composite* structures in the sense of made up of different building blocks able, as a whole, to break the Snoek law and allow for a fine tuning of the electromagnetic response [18]. A typical example is represented by Fe nano-flakes coated by SiO_2(Fe/SiO_2) nano shells, which have shown to be able to reach -2 0dB reflection loss on a large frequency band at 3.8-7.3 GHz, whereas pure Fe nano flakes can reach only -10 dB on the same frequency range [19]. This surface treatment was successfully applied as well to other ferromagnetic alloys [20]. Hereafter, with the term *composite* I indicate materials resulting from the assembly of different molecular building block in the sense described in this paragraph.

A more recent research line in the field of materials for EM field shielding is represented by nanocomposite systems integrated in a polymer matrix. This combination and the resulting fabrication technique has several advantage. One of them is that it can be used as paint to coat complex shaped objects. Good candidates to be used as a filler in a polymer matrix are spinel ferrites [21] of the type indicated in the central circle of Fig. 1.4. Spinel ferrites have a general formula MFe_2O_4 where M a divalent metal cation (Zn^{2+}, Co^{2+}, Fe^{2+},..). This class of compounds has remarkable magnetic and electronic properties, a chemical stability over a wide temperature range and a variety of applications almost in every field of materials science. Studies by several research groups worldwide have shown that those kind of materials are characterized by remarkable absorption in the MW range, and that increasing the density of filler is a practical way to enhance the absorption characteristic.

1.3.2 Carbon based materials

In the search for lightweight, available and economically affordable materials for the range of application targeted in this Ph. D. project, a premier role is played by carbon based systems. The reason is due to the versatility and tunable properties that this class of

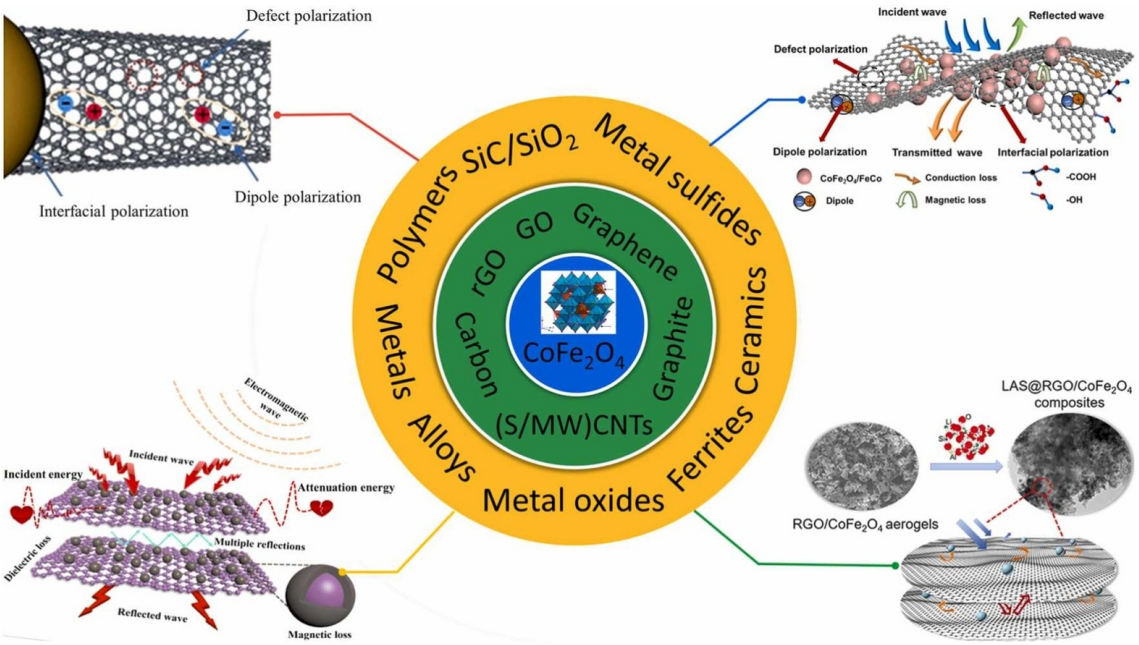

Figure 1.4. General overview of materials and mechanisms of interest in microwave absorption applications. In the inner circle the original well-assessed $CoFe_2O_4$ (spinel) is shown The middle circle shows the carbon-based nanocomposite, representing the next generation materials with respect to spinel, and the outer circle shows all the other materials studied or under investigation to date. Figure taken from [3]

system has shown over the years in a wealth of application. Just to cite a few of these advantages, we can mention the low fabrication cost, abundance of carbon and possibility of synthesis in several topologies, running from graphene to carbon nanotubes, flakes and even synthetic diamond[22, 23]. The rich panorama of carbon-based composites is generally subdivided and classified according to the hybridization of the C valence orbitals. Indeed, since the C atom has six electrons, namely $1s^2\ 2s^2\ 2p^2$, the formation of chemical bonds can result in double C=C bonds, single C-C bonds, aromatic bonds for ring structures as in benzene or graphene, although the majority of then is planar with an sp^2 hybridization, non-planar sp^3 hybridization are possible as in diamond with intermediate possibilities represented by fullerenes and nanotubes where bond angles can assume intermediate values between $\sim 109.5^o$ (sp^3) and 120° (sp^2) showing a flexibility rather uncommon with respect to other chemical elements.

The typical sp^2 hybridization results into a three-fold C site carrying 3 σ bonds as valence electronic orbitals and one additional π state. This specific state does not form actual chemical bonds, is orthogonal to the plane defined by the three σ bonds and can delocalize and overlap with analogous orbitals of other C sites as in the textbook case of graphene. This delocalization, in turn, brings a lot of interesting electronic properties such as the good charge carrier mobility [24], characterizing exactly graphene sheets [25]. The mentioned flexibility of the carbon bonding structure allows to roll up the sheets into cylindrical objects identified for the first time by Ijima and coworkers and nowadays termed carbon nanotubes (CNTs) [26] [27] or pseudo-spherical nano-objects known as fullerene, for which Curl and Smalley were awarded the Nobel prize in chemistry in 1996. These peculiar structures complement the traditional stacked graphene (graphite), naturally formed and widely used since the beginning of human civilization. As known, at high pressure sp^3 bonds are realizing resulting in the formation of diamond. To complement this brief summary, I wish to mention that an sp^1 (or simply sp)structure is also a viable possibility in which a C atom realizes two π states, instead of one, along with two σ bonds. In this

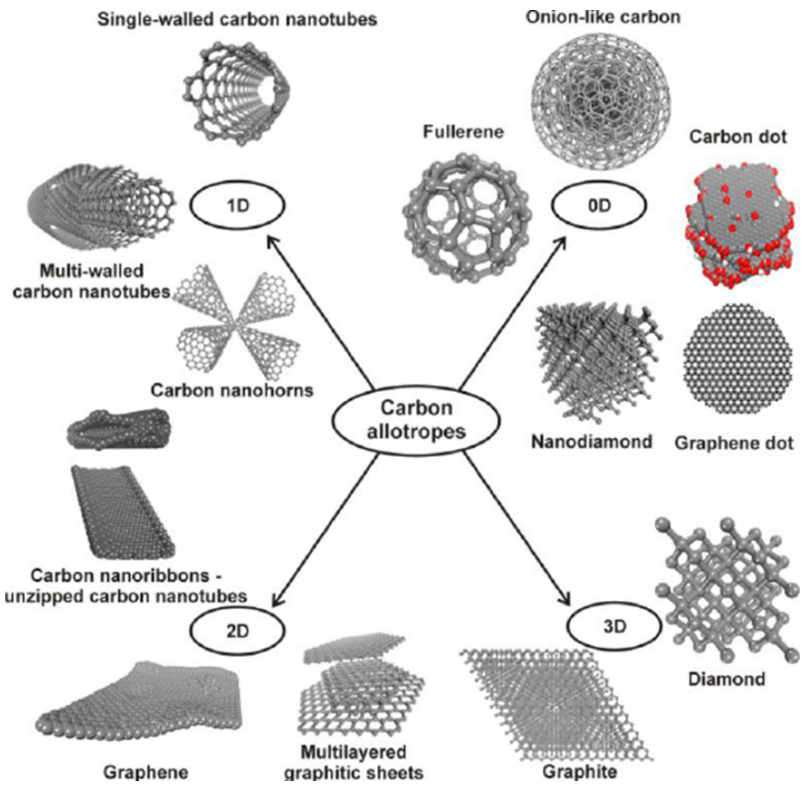

Figure 1.5. Classification of different carbon based systems. The quasi-0D ones consist of stacked carbon or rolled up graphene into fullerene, 1D structures are essentially rolled up graphene into carbon nanotubes (CNT), 2D are graphene layers or a limited number of stacked graphene, and 3D systems are essentially carbon black (graphite) and diamond.

case also, the π states undergo delocalization an,d since this configuration only allows forming a chain structure called carbon fiber (CF) [28, 29], the presence of the delocalized π orbitals can result in conducting polymers. A graphic summary of all these structures is presented in Fig. 1.5. Early studies considered only the less complicated and naturally abundant carbon structures due to difficulties or lack of fabrication processes and synthesis protocols, C-based systems syntheses being limited to evaporation and growing techniques [30]. This was refined later and nowadays new technologies make feasible a wide variety of carbon-based architectures, such as atomic printing able to produce complex shaped nanocomposites [31].

Polymers

In the context of the present work, polymers play an important role as support of molecular building blocks such as CNTs or fullerene. Now, beside being a support, whose role will be targeted and unraveled in a forthcoming chapter of this doctoral thesis, also the class of polymers interesting for the applications sought in the field of electric and magnetic response turn out to be essentially carbon-based materials. Indeed, by limiting this brief overview to the most common industrial polymer, studied also in my doctoral project, a common compound is the epoxy resin. Its advantages over other polymers are the easy process needed for its synthesis, its ability to mix with elementary C-based building blocks (e.g. CNTs) or nanocomposites and its stability over a rather wide range of temperature. All these properties translating into low production cost and easy industrialization. Depending on the targeted application, different characteristics are needed. Hence, various type of polymer can be used or, as in the case of the epoxy resin, different functional groups can be attached to the main body of the hydrocarbon backbone or to its terminal groups, thus allowing also to modulate the length of the polymeric chain and

its chemical nature (reactive or inert).
The polymer mostly utilized to date is the poly(methyl methacrylate), briefly referred to as PMMA [32], consisting in a chain of monomers of C atoms with single and double bonds plus two O atoms which generally form hydrogen bonds with surrounding hydrophilic moieties or are used as sites to functionalize the polymer. PMMA is a transparent thermoplastic with low impact on the intrinsic properties of the molecules or nano-objects that it can hot and, as such, well fit in a wealth of applications from flexible electronics (ionic gels) to electromagnetic shielding. The ease to mix with the hosted molecular or nano-meter elementary blocks is a fundamental condition because the microwave absorption property of the nanocomposite polymer/molecular (or macromolecular) inclusion strongly depend on the nanostructures created inside such a nanocomposite and on the atomic-level interactions between polymer and hosted (nano)system. For instance, clusters of filler nanocomposite give rise to polarization phenomena which have a non-negligible impact on the absorption characteristic [22]. Thus, the mixing ability and the nature of the guest-hots interplay between polymer and hosted molecular systems is a key factor in the realization of an efficient polymer/filler system. In the current technology, there are three main approaches for introducing a specific molecular building block into a polymer matrix: (i) The first is a mechanical mixing, polymers are initially in a molten phase and inside this liquid-like state the desired molecular or nano-sized objects are inserted before proceeding to solidification of the polymeric matrix. (ii) The second one is the in situ formation of the filler, the polymer matrix is already formed, whereas the hosted molecules or macromolecular objects are syntesized directly inside the matrix. (iii) In the third method, the molecular or macromolecular object is initially dispersed into a monomer matrix composed by the precursors of the polymer, then the polymerization is operated by a suitable trigger resulting in a matrix incorporating the hosted molecular components.

1.3.2.1 Carbon nanotube

Since the carbon nanotube is the major system used and studied in the present Ph. D. project, I provide here some additional detail useful to support the discussison of the results presented in the next chapters. As mentioned above and illustrated in Fig.1.5, a CNTs which can be seen as a rolled graphene whose curvature radius can vary, although fine control of this parameter is still a challenge. It has become an important C-based system since its long cylindric shape confers to a CNT a unique quasi-1D structure [26]. According to the rolling process and curvature radius, different chiralities can be realized and the chirality is the quantity that is currently used to classify CNTs. The chirality of a CNT is expressed by two indices n and m and indicated as (n, m). With this classification scheme, we can identify three distinct cases: (1) if $m = 0$ the CNT border assumes a *zigzag* structure type; if $m = n$ the same border takes an *armchair* configuration; finally, in all other cases a *chiral* CNT is realized. The majority of CNTs are characterized by semiconductor properties with the remarkable exception of the armchair CNT, which possesses a metallic behavior. As expected, those differences imply different dielectric characteristics. The chirality can be somehow controlled using TEM characterization [33], although synthesis with a specific desired chirality is still elusive. Despite their intrinsic properties, either semiconductor or metallic, CNTs are generally non-magnetic nano-objects, thus their microwave absorption originates from dielectric relaxation, polarization and ohmic loss [34].

A point worthy of note and that makes CNTs interesting in term of cost efficiency, is that composite systems that use CNTs require a really low CNT *vol*% to get the desired dielectric properties. Such a low amount is mainly due to their aspect ratio which is defined by l/a, being l the length and a the diameter of the CNT. Basically, their nearly

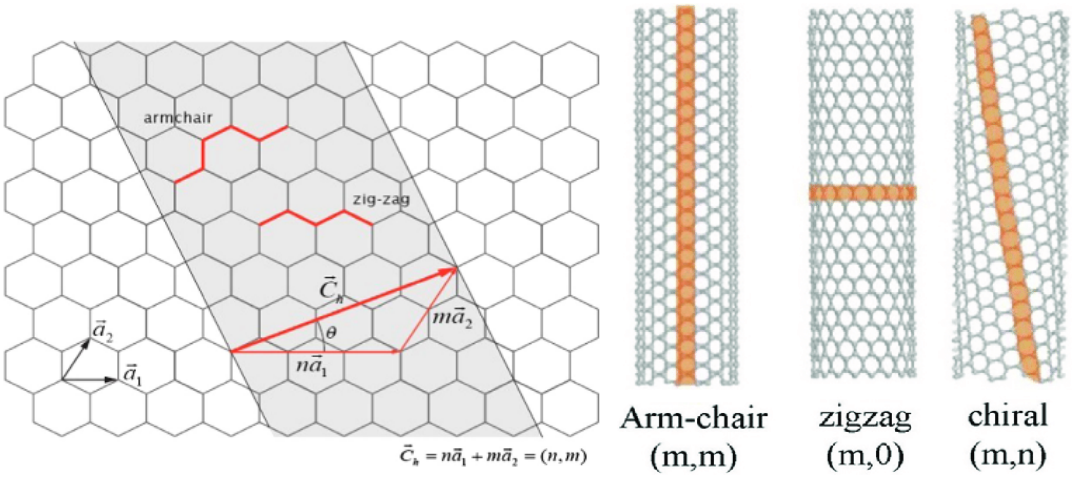

Figure 1.7. Schematic summary of the chirality of CNTs staring from the flat graphene sheet before the rolling process. The chirality of the CNT results from the initial rolling angle of the sheet. Figure taken from [4].

one-dimensional character is the feature that allows to reduce to a minimum the amount of CNTs needed for the realization of a device. The typical range of aspect ratio of CNTs used nowadays is in the range between 100 and 1000. Thus, the percolation threshold can be reached at 0.1-1 *vol*% [35] and it has been already shown that very good dielectric properties are reached at only 0.35 *vol*% [36].

CNT coated with ferromagnetic nanoparticles

To tune and optimize the intrinsic characteristics of CNTs, namely to make them able to absorb EMWs such as radar or microwave interferences, a better matching between dielectric loss and magnetic loss is needed. This can be achieved by combining CNTs with some other atomic or molecular object suited to increase the electromagnetic response properties that a bare CNT cannot provide. Specifically, to enhance the matching between the magnetic and the dielectric response, researcher had the idea to create systems composed of CNTs interacting with metallic/ferromagnetic elements, clusters or nanoparticles. To this aim, three different approaches were tested, whose success depends on the targets and scope of the resulting composed hetero-system.

The first is the substitution of a C atoms of the CNT network with metallic ones [37], a bit complicated to realize since atomic replacement in the rather stable CNT is energetically demanding.

The second is to fill the inner cavity of the CNT cylinder with metallic atoms or small clusters of size compatible with the CNT diameter[38]. In this case, it has been reported that filling CNTs with Fe nano-particles (NPs) improve the complex permittivity and complex permeability [39, 40] and these characteristics can be controlled by the chemical nature and concentration of the filling NPs. This observation was also made for different ferro- or ferrimagnetic molecules, such as spinel, where the complex permittivity and permeability of the CNT/spinel system outperform those of spinel and pure CNTs [41].

The third possible way pioneered consists in decorating or coating CNTs with metallic NPs [5, 42], exploiting the surface plasmon absorption (SPA). In this case the performance of CNTs coated with metallic NPs have been observed to undergo a remarkable enhancement and the decoration process results less demanding than atomic substitution[43, 44] thus becoming more promising and versatile than the former two cases. Indeed, dielectric and magnetic properties improve remarkably upon metallic ferromagnetic coating and, additionally, this can lead to new optical, electronic or magnetic properties according to the chemical nature of these heteroatoms [45, 46]. In the microwave domain, Sui and

coworkers have shown that Co atoms deposited on CNTs allow to modulate the frequency response of composite polymer/CNT systems resulting in a shift of the absorption peak [47]. Another example concerns the hydrogen functionalization of CNTs that induces changes in the THz range of the power absorption spectrum measured by time-domain spectroscopy [48].

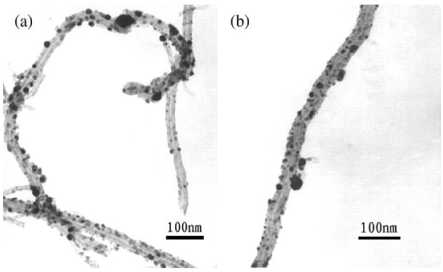

Figure 1.8. TEM images of MWNTs decorated with cobalt nanoparticles as reported by Z. Dong *et al in Materials Letters* **62**, *4059-4061 (2009). [5]*

1.3.2.2 Graphene based systems

Graphene

Graphene is a well-known 2D structure composed by carbon atoms in a hexagonal arrangement realized by chemical bonds having sp^2 hybridization. As mentioned above, the electronic orbitals orthogonal to the graphene plane confer to graphene a high charge carrier mobility μ (namely $\mu > 10^4$ cm^2/Vs) and a high electron/hole concentration n which can reach values of $n = 10^{13}$ cm^{-2} [49]. The peculiar electronic band structure of graphene gives rise to a quasiparticle called the massless Dirac fermion, which can be described in terms of the relativistic generalized Dirac's equation, and has several potential applications ranging from the design of new materials and to applications of existing material (e. g. graphene) in next-generation electronics. The characteristics briefly summarized here make graphene an ideal component for innovative nanocomposite with electronic characteristics that can be either designed *ad hoc* or tuned to comply with specific requirements such as the EMI problems targeted in this work. I wish to add also that graphene possess a relatively high thermal conductivity, thus becoming appealing also for heat transport applications.
A drawback, however, is the fact that graphene presents huge problems when incorporation into a polymeric matrix is attempted. On one hand, the stable structure and strong atomic-scale interactions make difficult to use sheets or large graphene flakes as a filler for a polymer, despite the three different incorporation methods mentioned in this chapter. On the other hand, graphene has a strong hydrophobic character that makes complicated its handling in solutions, including polymer precursors in the liquid state.
An interesting route to modify the intrinsic properties of graphene has been shown to be oxidation, consisting in replacing some C sites with O atoms either on the pristine honeycomb structure or upon creation of vacancies. Given the importance of this so-called grphene oxide system in the context of my doctoral work, I dedicate the following paragraph to this specific form of graphene.

Graphene oxide and its reduced form

The insertion of oxygen into the two-dimensional graphene carbon network is a forefront research line rich of possibilities not yet fully exploited (or understood). As mentioned at the end of the above paragraph, graphene oxide (GO hereafter) is a graphene monolayer in which O atoms substituting C sites can change locally the electronic structure of the

system and/or can become centers for binding functional groups. The original scope was to find a workaround to the hydrophobic character of pristine graphene, since O or carefully selected functional group can promote the formation of hydrogen bonds in polar solvents and increase the graphene solubility in water [50]. GO is produced by treating graphite with strong oxidants, followed by an exfoliation process. Functional groups are chemical moieties carrying oxygen atoms such as, for instance, carboxylic acid, epoxy and phenol hydroxyl [51]. Both substitutional O atoms and this type of functional groups function break the sp^2 hybridization of the graphene network and introduce sp^3 on with the net effect of the arising of out-of-plane chemical bonds. As a consequence, on these sites the orthogonal π-states disappear and GO is no longer a 2D conductor, but becomes an insulator.

The GO carrying functional groups, contrary to the pristine graphene, can be incorporated inside a polymeric matrix by virtue of its newly acquired hydrophilic properties ensured by the presence of O sites. Upon incorporation, GO can be reduced to obtain reduced Graphene oxide (rGO), in which most of the functional group are removed, leaving behind just O atoms. This allows (at least partially) to recover an sp^2-like planar structure. However, as a result of the removal, the new lattice contains defects, mainly vacancies or multi-vacancies, because of the removal of carbon atoms and, as a consequence of oxidation, O atoms replace some carbon sites [52]. This new material possesses characteristics similar to graphene, but its conductivity properties can vary over a wide range of values depending on the reduction treatment used (i. e. amount of vacancies and O atoms in the network), ranging from 10 to 10^3 S/cm [53], to be compared with the nominal value of 10^4 S/cm in pure graphene [22].

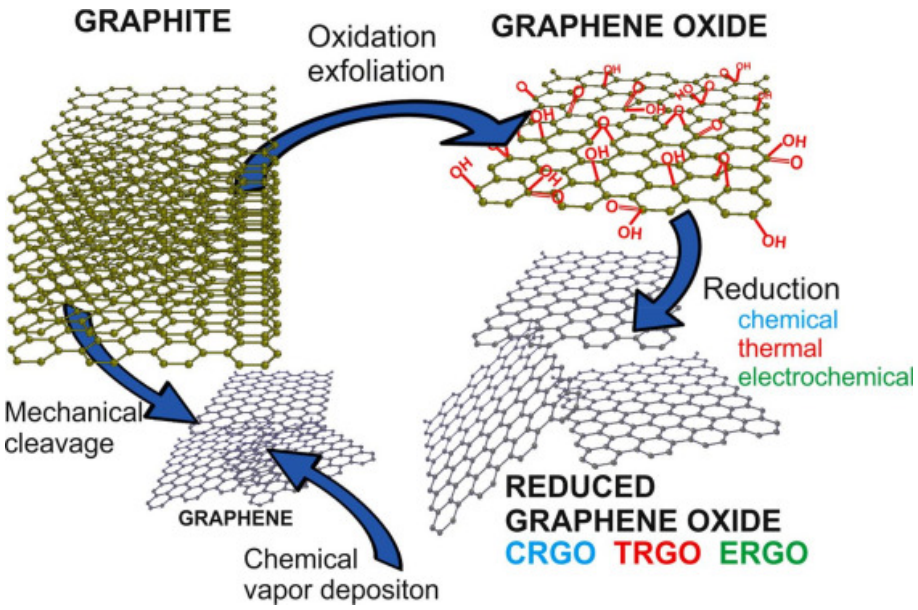

Figure 1.9. Graphical summary of the different phases leading to the production of reduced graphene oxide (rGO). Depending on the reduction process, rGO can be obtained, the chemically reduced GO (CRGO), the thermally reduced GO (TRGO), and the electrochemically reduced GO (ERDO). The physical properties of rGO depend of the reduction process. Image taken from [6]

1.4 A brief survey of the computational methods used for C-based systems modeling

While the next chapter will be dedicated to the methods used in my own doctoral project, I provide here a short overview in molecular and atomic-level modeling approaches used

to simulate the systems presented in the former paragraphs and targeted in the present work. Without any claim to completeness, this small section has to be regarded as an overview on what is available nowadays in the field of computational approaches oriented to the class of materials in which I am interested.

1.4.1 Empirical methods

To determine the mechanical, structural and dynamical properties of a large number of atoms, traditionally classical molecular dynamic has been developed. This approach, based on an iterative solution of the Newton's equations of motions for all the particles constituting a system, is based on a simplified description of the interactions occurring among the atoms. This simplified description consists in an analytic form of a potential function from which gradients, hence forces acting on the atoms, can be computed. Being the electronic degrees of freedom excluded and thanks to the analytic interatomic potential easy to handle, large systems, nowadays up to millions of atoms can be simulated over a time scale of a few thousands of ns on the most performing high-performance computing platforms and well tuned codes.

The base simplification is that the detailed electronic structure is not needed at this level of approximation and atoms interact solely via a function that depends on the instantaneous atomic position, not their velocities. In this respect, this becomes a *static*, or better electrostatic, approximation, legitimate by the fact that the speed of atoms, far from any possible relativistic range, play a negligible role. The whole system evolution is given by a numerical integration of the Newtonian classical equations of motion, as mentioned above. The specific form of these classical potentials rely mostly on empirical assumptions and *a posteriori* benchmark on experimental results. They contain, in an unavoidable way, parameters that need to be adjusted from experiments or higher-level theoretical results as provided by *ab initio* calculations. Another drawback is the fact that once assessed for a given system these classical potentials cannot be generalized to a different system, since changes in the atomic arrangement (structure) and/or chemical components of a condensed phase imply a profound change in the electronic structure, hence on the nature of the interactions among the atoms, thus calling for a reformulation often far from trivial.

1.4.2 Monte Carlo methods

Monte Carlo (MC) methods represent a wide class of algorithms based on educated random sampling of the phase space allowing to compute physical properties and behavior of a given system. Their use is widespread in a variety of different fields from nuclear physics to condensed matter. Contrary to molecular dynamics, where the phase space is explored iteratively along a time-oriented trajectory generated by equations of motion, MC methods rely on a stochastic exploration of the same phase space without involving dynamics but a sort of point-by-point probe of the configurational space of total energy surface spanned by the system under study. Randomly generated numbers, carefully weighted on specific *ad hoc* functions depending on the physics/chemistry of the system, are used to calculate physical parameters (energy, structure, etc.) within the Central limit theorem.

A textbook application of the MC approach is the exploration of a given potential $V(x, y, z)$, either empirical or ab initio, in which the coordinates x, y and z are sampled at different numerical values and the (potential) energy computed accordingly. An improvement to this blind random sampling is represented by the use of a Markovian chain algorithm in which the related master equation allows for a driven and *educated* guess of the random values to be sampled.

An interesting version of MC modeling in materials science is the one known as Kinetic MC. This method allows to compute the evolution in time of a system. The basic principle is the definition of an *appearance frequency*, namely the frequency during the sampling at which a give event occurs, and this provides also an estimate of the simulation time needed to get this specific event. A typical application of the Kinetic MC is this study of defect mobility in solid-state systems.

1.4.3 Quantum mechanics based method

This class of methods will be extensively discussed in the next paragraph, since they have been my preferred approach all along my Ph. D. work, due to the fact that the explicit inclusion of the electronic structure information and its evolution is essential to rationalize the dielectric response and to characterize the behavior of a system in terms of absorption and dipole dynamics required for all cases in which EMI problems are involved. For completeness with respect to the sections above, I limit the discussion to the basic features. Quantum mechanics allows to describe in a consistent way the electronic structure of materials. This resumes to solving the Schrödinger equation for a multi-electron system, a task very demanding and for which several methods have been proposed over the years. The only prerequisite is the knowledge of the atomic species composing the system and their positions. In this respect, we are still in an electrostatic approximation and all methods of this type fall in the class of the so called *ab initio* or first principles methods.

The system's electronic structure and geometry are given by minimizing numerically the total energy functional dependent on the electron wavefunctions $\psi_i(\mathbf{x})$ $(i = 1, ..., N)$ and atomic coordinates $\mathbf{R}_I$ $(I = 1, ..., M)$ for a system composed by N electrons and M nuclei. I wish to underscore that the nuclear degrees of freedom are still treated as classical variables, contrary to the electrons. Approximation have been proposed to overcome the problem of solving the many-body Schrödinger equation, trying (but not always succeeding) in avoiding big loss in information. A successful example is the Born-Oppenheimer (BO) approximation in which the nuclear problem is disentangled by assuming that nuclei are heavier than electrons and, as such, much slower so that only their instantaneous positions as a sort of external parameters are needed to solve the electronic structure problem. The solution proposed by Walter Kohn, nowadays known as density functional theory (DFT), consists in abandoning the idea of single wavefunctions for each electronic degree of freedom and assuming only a collective distribution accounting for all the electrons of the system, the electronic density $\rho(\mathbf{r})$. The details of BO and DFT schemes will be two of the subjects discussed in detail in the forthcoming chapter.

Although this is outside the scope of my research work, for the sake of completeness I wish to mention that computational methods in the field of electromagnetic fields and matter interactions include also larger scales and mesoscopic descriptions as in the cases of coarse-graining and finite elements methods, respectively. The price to pay, of course, is a more demanding modeling of the interactions between grains or blocks of the finite elements and the absence of an atomic-level information.

As a complementary information, I wish to remind that the success encountered by BO and DFT methods was boosted by recent development in computing technology. Nowadays accessible high-performance computing (HPC) architectures, constantly evolving along the computer codes in which first principles algorithms are implemented, have made the field of computational science a new frontier to perform advanced simulations that are currently regarded as reliable virtual experiments where materials and their properties can be studies before moving to the actual production stage.

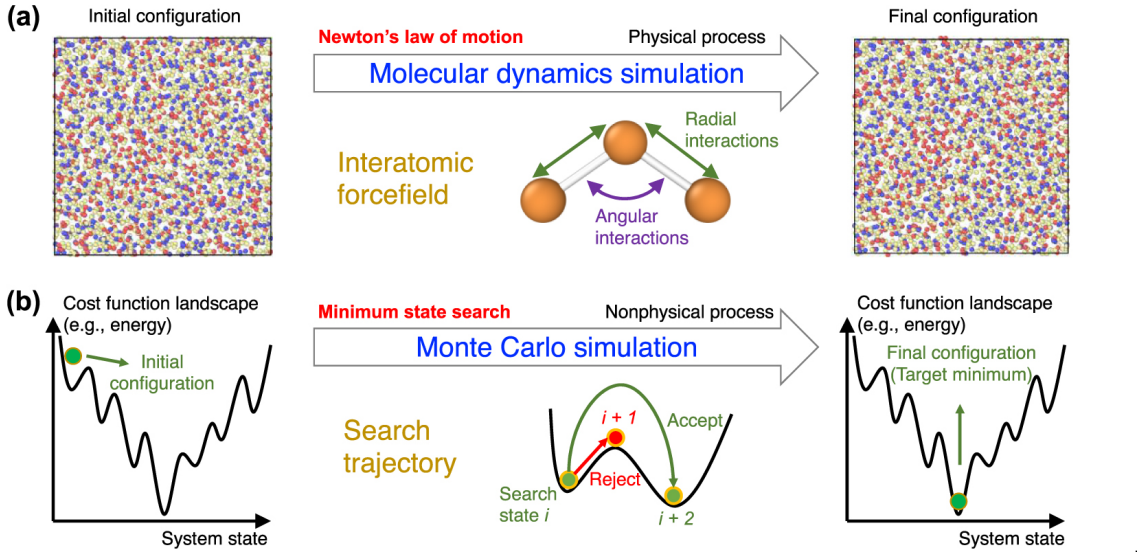

Figure 1.10. Schematic summary of the difference between molecular dynamics and Monte Carlo simulations. The image is taken from [7]

1.5 Final remarks

As summarized in this general introduction, constituting the first chapter of my Ph. D. thesis, materials for electromagnetic absorption is an active and constantly growing research field rich of industrial applications. On the theoretical standpoint, the EMA theory is well assessed at different levels, from classical electrodynamics to semi-classical theory as, for instance, the Drude-Lorentz theory extensively used to describe the light matter interaction (LMI) in terms of dipolar interactions well suited to rationalize absorption and reflection processes. Still useful are phenomenological models, such as the Einstein one for LMI, which describes the radiation at thermal equilibrium and is grounded on thermodynamical arguments. Although a bit outdated, it allows to predict light emission phenomena, despite the fact that more recent advances at the quantum level represent a more accurate and precise approach to LMI.

On the experimental side, forefront innovative techniques have been able to unravel at unprecedented levels of accuracy the LMI of carbon and non-carbon based materials and, even more important, to synthesize and produce all the new forms of carbon-based systems presented in this chapter.

The synergy and complementary roles of theoretical modeling and advanced experimental techniques provide a comprehensive, although not exhaustive, overview of the LMI general problem. To date, researchers have been able to reach a good understanding of the processes that occur in microwaves range, such as relaxation phenomena, ohmic loss, etc., as well as phenomena occurring at an atomic scale level such as the diffusion and dispersion law of an electron in the graphene electronic band. Nonetheless, a lot of work is still needed in more complex carbon-based systems, especially the most recent ones that could be discovered and assembled only after recent breakthrough in terms of synthesis and characterization.

A point that is difficult to afford and for which a general solution is still elusive is the link between macroscopic properties and fundamental mechanisms at a molecular and atomic scale. Despite impressive HPC advances and increased codes performances, the present computing power still does not allow for an ab-initio treatment of large systems, namely more than 1000 atoms, on a time scale beyond a few hundreds of ps. This bottleneck is one of the limits that I explored in my doctoral project, trying my best to push my

simulations as far as possible within the reach of the available HPC platforms. Specifically, I used intensively the linux supercluster of the HPC Center of the University of Strasbourg, specifically CAIUS (Cluster de cAlcul Intensif à l'Universitséé de Strasbourg, https://hpc.pages.unistra.fr/) and the Tier-1 level facilities provided by GENCI (Grand équipement national de calcul intensif, https://www.genci.fr/) and in particular Joliot-Curie supercompupter (AMD Rome partition) of the TGCC centre in Grenoble. Taking into account the continuously growing computer power and improving technologies, along with better performing codes and algorithms, I paid special attention at pushing the limits of first principles dynamical simulations to compute on-the-fly dipole moments and major quantities used in a post-processing stage to extract absorption spectra and dielectric response to be compared with the experimental outcome. Whenever stumbling blocks appeared, particularly in the simulation time, whose reciprocal value is an indicator of the minimal frequency reachable, I sought for alternative methods (e. g. dynamical matrix and perturbation theory) with the results that will be detailed in the next chapters. Generally, despite still existing shortcomings, this type of modeling represents a new frontier in the use of computational methods to complement or replace explorative experiments, with consequent cost reduction, before moving to the real production stage of materials and devices.

My research work targeted specific and relatively well assessed systems, to reduce the amount of uncertainties that an unexplored field implies, both in terms of materials and methods. This was done in synergy with industrial partners as Dassault Aviation and experimental colleagues working in the same domain and within the same MOLIERE LabCom initiative with the support of the Agence de l'Innovation de Défense (AID).

For this reason, carbon based materials have been identify as the best candidate systems for the scope of this thesis, with special emphasis on CNTs and graphene (rGO), being the most promising materials for applications in electronic devices, EM shielding, reinforce for construction materials, and several other possibilities disclosed in the recent years. Moreover, carbon is a widely diffused element on Earth and, as such, it has a low production cost and a mitigate environmental impact. After a summary of the computational methods used in my work, presented in Chapter 2, I shall present my results on CNT coated with Cobalt nano-particles in Chapter 3. This specific system is one of the most appealing possibilities illustrated in this introduction and deserves special attention in terms of modification of the dielectric response upon decoration with Co on the pristine nanotube. Since a simultaneous atomic and electronic description of a large system such as a CNT coated with Co is needed to accurately model the electronic interactions between the two moieties, the first principles molecular dynamics (FPMD) approach has been my privileged computational tool in this case. This has been also a good occasion to check on a realistic model to which extent these methods can be pushed to reach (or not) the desired frequency range.

Again in synergy with experimental coworkers and following their guidelines, we have seen that carbon based nano-composite can be created using 3D printing techniques. This has disclosed a new scenario consisting in response of CNTs interacting among them and inserted into a polymeric matrix. This has driven the research efforts presented in Chapter 4. In this case, due to huge system size, I resorted to dynamical matrix and perturbation schemes to work out the frequency range associated to interacting nanotubes and the effect of polymers, as the PMMA introduced in this chapter, on the spectrum of these composite objects.

Analogously, recent experiments focused on rGO systems were te major motivation of my simulations on reduced graphene oxide models discussed and detailed in Chapter 5. Also in this case, on the basis of the experience provided by the former two chapters in terms of better suited computational approaches, I focused my calculations on the spectral

response, being this the leading general motivation of the present research.

Chapter 2

Computational Methods

Summary

This chapter is intended as a highlight of the computational methods and algorithms used in this thesis. The purpose is to present in a brief, yet complete way, the atomic-scale modeling techniques, based on first-principles approaches, that allowed to obtain the results presented in the following chapters. Starting from classical molecular dynamics, I shall review its extension to quantum-mechanical based treatment of the electronic interaction, within the density functional theory framework, to extract physical observables from temporal averages, within the ergodic principle, providing the macroscopic quantities useful to compare with experiments and to provide guidelines to the realization of materials for the applications targeted in my project.

2.1 Introduction

One of the major objectives of my doctoral project is the understanding of microscopic phenomena that escape experimental investigations and that have a microscopic origin resulting in a macroscopic response of the materials. This challenging issue calls for adequate atomic and molecular scale simulations rooted in quantum mechanic and suited to provide the measurable quantities sought.
Given the nowadays state-of-the-art, the best tool available in computational physic and chemistry, able to account for fundamental interactions at a quantum mechanical level and to allow for a time-evolving modeling of the ensemble of atoms simulated is the ab-initio molecular dynamic (AIMD). This is a computationally affordable way to cope with the non-trivial problem of many-body interactions for a system composed of nuclei and electrons. For these reasons, in this chapter I present the methods I used during my thesis work. To this aim, I first highlight the physic behind these methods in order to put them in their correct context and also to probe their strengths and their limitations for the applications I am interested in. In the first part, I give a brief review of the quantum mechanical treatment in the case of a multi-electron system. The electronic structure problem will be approached in the framework of the density functional theory (DFT). Then I shall focus on how DFT is used as a *driver* to perform AIMD simulations. Formally correct, DFT still resorts to approximations that crucially determine its applicability and reliability in providing quantitative results. This will be explicitly discussed in an attempt at understanding limitations and shortcomings that AIMD as a whole and DFT in particular introduce in an AIMD-based modeling project.
A brief overview of the molecular dynamic methods and algorithms will be introduced. Without any claim of completeness, since a lot of literature and excellent books are available, I describe how forces are computed and implemented in order to be able to dynamically explore a potential energy surface (PES). In the specific case of AIMD, two numerical integration methods of the underlying equations of motion (EOMs) are presented, the Born-Oppenheimer Molecular Dynamics (BOMD) and the Car-Parrinello Molecular Dynamics (CPMD), both of them falling the AIMD classification scheme in the related literature. Since the majority of the simulations presented here are done in the canonical ensemble (NVT) at finite temperature T, an overview of the temperature control methods is provided, with special attention to implementation of a thermostat for which I gave my contribution in the course of my doctoral studies.
Summarizing this short overview, while it is true that AIMD provide useful atomic-level information on the system, their post-processing elaboration and translation into experimentally measurable parameters requires a careful handling and accurate treatment. For this reason, in the last part of this chapter I provide some description of methods suitable to determine electromagnetic properties and related measurable quantities of the system starting from the atomistic information extracted from my simulations.

2.2 Density Functional Theory

The density functional theory (DFT) [54], is a re-formulation of quantum mechanics for a may-body system originally proposed by W. Kohn and L. J. Sham in 1965. This scheme allows to determine the electronic ground state of a multi-electrons system and the ground state of electron wave function is reformulated in terms of the global electronic density. The consolidated success of this method was awarded by the Nobel prize in chemistry to Walter Kohn in 1998 [55], jointly with John Pople, and is still the most used approach in a wealth of fields from quantum chemistry and physics to materials science and biochemistry. This success is mostly due to the affordable computational cost that characterizes DFT

with respect to other quantum chemical methods (especially wave-function based) that imply a heavy computational burden, translating into severe limits of affordable systems size and, in the case of dynamics, maximum simulation time.

2.2.1 Electronic structure

In the framework of non-relativistic quantum mechanics, a system evolution can be fully described by the time-depending Schrödinger equation:

$$i\hbar\frac{\partial}{\partial t}\Phi(\mathbf{r},\mathbf{R},t) = \hat{H}\Phi(\mathbf{r},\mathbf{R},t) \tag{2.1}$$

Where $\mathbf{r}$, $\mathbf{R}$ is the notation for the vectors representing, respectively, the argument of the electronic wavefunctions and the atomic positions. Φ is the many-body the quantum state of the system. This function contains all the system information and is depending on time, and positions of the two ensemble of degrees of freedom ($\mathbf{r}$,$\mathbf{R}$). These two vectors can be written explicitly as $\mathbf{R} = \{\mathbf{R}_i\}_{i=1,\dots,N_{at}}$ and $\mathbf{r} = \{\mathbf{r}_i\}_{i=1,\dots,N_{el}}$, where N_{at} is the total number of nuclei and N_{el} the total number of electrons composing the system. Whenever the quantum state does not depend on time, we have the typical *static* Schrödinger equation:

$$E_{tot}\Phi(\mathbf{r},\mathbf{R}) = \hat{H}\Phi(\mathbf{r},\mathbf{R}) \tag{2.2}$$

The resolution of this eigenvalues equation is, at least in principle, essential to get a full description of the spectrum and energy characterizing the many-body system. However, in practice, it represents a non-trivial problem often impossible to solve due to the complexity of the systems. In many cases, including the condensed matter framework of this thesis project, the many-body Hamiltonian can be divided into three contributions:

$$\hat{H} = \hat{T} + \hat{V} + \hat{V}_{ext} \tag{2.3}$$

1. In this formulation, $\hat{T}$ represents the kinetic energy operator of the system, which can be decomposed into $\hat{T} = \hat{T}_N + \hat{T}_e$, namely the kinetic energy of nuclei and the corresponding one for the electron, both written here as quantum operators acting on the nuclear and electronic wavefunctions, respectively:

$$\hat{T}_N = -\sum_{a=1}^{N_{at}} \frac{\hbar^2}{2M_a}\nabla^2_{\mathbf{R}_a} \tag{2.4}$$

   and

$$\hat{T}_e = -\sum_{i=1}^{N_{el}} \frac{\hbar^2}{2m}\nabla^2_{\mathbf{r}_i} \tag{2.5}$$

   Here, M_a is the mass of the a-th nucleus and m is the electron mass.

2. $\hat{V}$ is the interacting potential energy operator of the system. In an ensemble of N_{at} atoms and N_{el} electrons, there are three different types of interactions, among electrons ee, among nuclei NN and among electrons and nuclei Ne. By assuming that both ensembles interact only in an electrostatic way (as opposed to an electrodynamical treatment, typically restricted to relativistic cases), the Coulomb interaction assumes the form of a linear combination, $\hat{V} = \hat{V}_{NN} + \hat{V}_{ee} + \hat{V}_{Ne}$. These three terms have the explicit analytic forms:

   - $\hat{V}_{NN}(\mathbf{R})$ the interaction between nuclear variables

$$\hat{V}_{NN}(\mathbf{R}) = e^2\sum_{a<b}^{N_{at}} \frac{Z_a Z_b}{|\mathbf{R}_b - \mathbf{R}_a|^2} \tag{2.6}$$

where Z_a and Z_b are the atomic numbers of the atoms localized at the positions $\mathbf{R}_a$ and $\mathbf{R}_b$, e is the electronic charge and the sum is done on half of the nuclear subset $a < b$ to avoid double counting.

- $\hat{V}_{ee}(\mathbf{r})$ the interaction between electrons

$$\hat{V}_{ee}(\mathbf{r}) = e^2 \sum_{i<j}^{N_{el}} \frac{1}{|\mathbf{r}_j - \mathbf{r}_i|^2} \tag{2.7}$$

- $\hat{V}_{eN}(\mathbf{r}, \mathbf{R})$ the interaction between electrons and nucleus

$$\hat{V}_{eN}(\mathbf{r}, \mathbf{R}) = -e^2 \sum_{i,a}^{N_{el}} \frac{Z_a}{|\mathbf{r}_i - \mathbf{R}_a|^2} \tag{2.8}$$

3. $\hat{V}_{ext}$ represent all the external potentials, that can come from different sources, from an applied external temperature or pressure, to an external electric field, depending on the type of calculation targeted.

We remark that, at this point, an over-simplification has already been introduced: the nuclear and electronic degrees of freedom interact only in pairs, as a consequence of the Coulomb expressions used above. This is not always a good approximation. On the contrary, it is a source of concern since many-body systems involve many-body interactions (hence beyond the two-body terms) and, if the variables are quantum objects, beside these *correlation* interactions, also *exchange* ones have to be properly accounted for. This will be discussed later in this chapter, but I anticipate here that these interactions represent a crucial contribution to the total energy of the system, for which developments and improvements are still work in progress even nowadays. Despite the simplification of two-body interactions, the resolution of this Hamiltonian would give us an insightful set of eigenvalues and eigenfunctions allowing to characterize a given system. The main issue is that a system of N particles ($N = N_{at}$ atoms $+N_{el}$ electrons) has $3N$ degrees of freedom, thus, for large systems, even within the simplified interaction introduced, the calculation time would be prohibitively expensive and in practice unfeasible, leaving aside any attempt at computing a time evolution. For these reasons, this is not a route that can be pursued for the systems on which this doctoral work (and not only) is focused.

2.2.2 Brief Review of the Density Functional Theory

To simplify the hard task of handling simultaneously nuclear and electronic degrees of freedom, the two ensembles can be considered as two separate subsets composed of heavy (nuclei) and light (electronic) particles whose motion occurs on different time scales: This is called the Born-Oppenheimer approximation, where the difference in mass ($M >> m$) and in speed ($v_N >> v_e$) between nuclei and electrons allows us to decouple their wave functions. This will be recalled later as the adiabatic approximation used to propagate in time the two ensembles of variables. To the scope of the present paragraph, this approximation allows to write:

$$\Phi(\mathbf{r}, \mathbf{R}) = \zeta(\mathbf{R})\Psi(\mathbf{r}) \tag{2.9}$$

where $\zeta(\mathbf{R})$ are nuclear wavefunctions and $\Psi(\mathbf{r})$ the electronic ones. Thus, by assuming that nuclei are acting as a static ensemble of coordinates on the fast time scale of the electronic motion, we can focus only on the electronic subsystem. Hence, the Hamiltonian of this subsystem becomes:

$$\hat{H} = \hat{T}_e + \hat{V}_e + \hat{V}_{ext}^e \tag{2.10}$$

As in the previous section, $\hat{T}_e$ and $\hat{V}_e$ are the electrons kinetic energy and the electron-electron Coulomb interaction. The interaction potential between electrons and nuclear variables, instead, is treated as an external contribution with respect to the electronic subsystem. As a word of warning, this potential in not *external* to the whole system, which is still constituted by its electrons and its nuclei, but just external to the electrons subsystem. We can add it to what has been called external in the former paragraph, thus obtaining the expression $\hat{V}^e_{ext} = \hat{V}_{eN} + \hat{V}_{ext}$, $\hat{V}_{ext}$. Let's define T_e, V_e and V^e_{ext} the eigenvalues of $\hat{T}_e$, $\hat{V}_e$ and $\hat{V}^e_{ext}$ respectively.

Since V^e_{ext} is a potential that depends on the nuclear positions, determined either via experiments (X-ray or neutron diffraction) or via theoretical calculations, its actual form and numerical value can vary according to the system studied. Nonetheless, for a given V^e_{ext}, the other two terms, T_e and V_e, are fully determined by the nature an topology of the system and are called "universal" operators. The remaining problem is then the solution of the electronic interaction part. Shortly after the rise of quantum mechanics and the Schrödinger equation for a multi-electron system, Llewellyn Thomas and Enrico Fermi proposed a model [56] to study N-body systems in a semi-classical way. In this scheme, we are no longer forced to use the many-body electronic wavefunction $\Psi(\mathbf{r})$, but a global description of the system in terms of its electronic density $n(\mathbf{r})$,

$$n(\mathbf{r}) = \langle \Psi(\mathbf{r}_1, \mathbf{r}_2, ..., \mathbf{r}_{N_e}) | \Psi(\mathbf{r}_1, \mathbf{r}_2, ..., \mathbf{r}_{N_e}) \rangle \tag{2.11}$$

The electron system is reinterpreted as an electron gas, more or less homogeneous or slowly varying, and the system is reduced from an unknown wavefunction to a scalar quantity (or two scalar quantities if the spin is accounted for) depending on a 3-dimensional vector $\mathbf{r}$. A problem in the Thomas-Fermi method is that it does not take into account the exchange energy of the system. In this context, a major improvement is the variational principle proposed by P. Hohemberg and W. Kohn [57] to describe the ground state of a system of interacting electrons in which their density $n(\mathbf{r})$ is the variable function. According to this formulation, for any system of interacting particles in an external potential, this potential is determined uniquely, except for a constant, by the ground-state density $n_0(\mathbf{r})$. This allows to reformulate $v_{ext}(\mathbf{r})$ as:

$$V^e_{ext}(\mathbf{r}) = \int d^3r n(\mathbf{r}) v_{ext}(\mathbf{r}) \tag{2.12}$$

and such a potential is a unique functional of $n(\mathbf{r})$, as well as $V^e_{ext}[n(\mathbf{r})]$. Thus, since $V^e_{ext}[n(\mathbf{r})]$ is the unique "non-universal" potential of the Hamiltonian, there is a direct correspondence between $n(\mathbf{r})$ and $\psi(\mathbf{r})$,

$$\psi(\mathbf{r}) = \psi[n(\mathbf{r})] \tag{2.13}$$

which is also a unique functional of $n(\mathbf{r})$. As anticipated above, this reduces the problem of a complicated many-body wavefunction to the search of a proper ground state distribution of the electrons. The ground-state of the corresponding Hamiltonian becomes, then, a functional of the ground state density $\psi_0(\mathbf{r}) = \psi[n_0(\mathbf{r})]$. This is basically the first theorem of Hohenberg-Kohn. The second theorem of Hohenberg-Kohn demonstrates that a universal functional for the energy $E[n(\mathbf{r})]$ in terms of the density $n(\mathbf{r})$ can be defined (in principle) exactly and it is valid for any external potential $v_{ext}(\mathbf{r})$. For any given $v_{ext}(\mathbf{r})$, the exact ground state of the system is the global minimum value of this functional, and the density $n(\mathbf{r})$ that minimizes the functional $E[n(\mathbf{r})]$ is the exact ground state density $n_0(\mathbf{r})$. In a formal mathematical language, if $E[n(\mathbf{r})]$ is the functional describing the whole system, it can be written as a sum of the universal potential (i. e. all the electronic interactions) $F_{HK}[n(\mathbf{r})]$ and the external contribution as:

$$E[n(\mathbf{r})] = F_{HK}[n(\mathbf{r})] + \int d^3r n(\mathbf{r}) v_{ext}(\mathbf{r}) \tag{2.14}$$

For any trial density $n'(\mathbf{r})$ different from the ground state one, The total energy calculated is never lower that the exact ground state one E_0, namely:

$$E[n_0(\mathbf{r})] \leq E[n(\mathbf{r})] \tag{2.15}$$

If $V_{ext}[n(\mathbf{r})]$ can be known precisely from the atomistic information of the system studied (i. e. crystallographic coordinates and related ionic partial charges), this is not the case of $F_{HK}[n(\mathbf{r})]$. The problem is then the exact determination of this universal potential.

A method to address this issue and determine the universal function was proposed by D. R. Hartree and V. A. Fock, nowadays known as the Hartree-Fock approach, a self-consistent field method whose solution assumes that the wavefunctions of a system of N electrons can be written in terms of Slater determinants of the form:

$$\Psi_a = \frac{1}{\sqrt{N!}} \begin{vmatrix} \phi_1(x_1) & \phi_2(x_1) & \phi_3(x_1) & \dots & \phi_N(x_1) \\ \phi_1(x_2) & \phi_2(x_2) & \phi_3(x_2) & \dots & \phi_N(x_2) \\ & & \dots\dots\dots\dots\dots & & \\ \phi_1(x_N) & \phi_2(x_N) & \phi_3(x_N) & \dots & \phi_N(x_N) \end{vmatrix} \tag{2.16}$$

Such a Slater determinant is a multi-electron wavefunction that satisfies the Pauli exclusion principle, where $\phi_i(x_j)_{i,j=1,\dots,N}$ are electrons orbitals and each index can include also the spin (up or down) in the so-called spin-unrestricted approach. This method leads to an electronic energy of the types $E_{HF}[n] = E_H[n] + E_X[n]$, where the first functional is the Hartree energy, $E_H[n]$, written explicitly as a Coulomb interaction:

$$E_H[n(\mathbf{r})] = e^2 \int\int d^3r d^3r' \frac{n(\mathbf{r})n(\mathbf{r}')}{|\mathbf{r} - \mathbf{r},|} \tag{2.17}$$

Thus, the E_H Coulomb electrostatic energy of the system depends on the density $n(\mathbf{r})$, or better on the the charge densities at positions $\mathbf{r}$ and $\mathbf{r}'$. Conversely, E_X is the exchange energy which come from the fermionic character of the electron and has no classical analog. For the exchange part of the interaction, the wave functions must be anti-symmetric upon exchange of two electrons of the system, thus producing a spacial separation between electrons that have the same spin, according to the Pauli exclusion principle, sometimes called Fermi hole. In the framework of this formulation, the energy given by the Hartree-Fock method does not provide the exact solution of the Schrödinger equation. The difference between $E_{HF}[n]$ and the real universal potential is the missing (in Hartree-Fock) term accounting for the correlation energy and originating from all the many-body interactions neglected in this formulation. It can be recovered by a number of considerations and often *ad hoc* assumptions. On a first instance, in a way analogous to the Fermi hole described above, the restriction in the space of two electrons with opposite spin, also called Coulomb hole, prevents two electrons from occupying the same space. Secondly, the kinetic energy is modified because of the many-body interaction. Indeed, we can write the kinetic energy as $T[n] = T_S[n] + T_C[n]$, and T_C can be included into the correlation energy E_C. Finally the exchange-correlation energy can be re-defined as a global functional of the electronic density:

$$E_{XC}[n(\mathbf{r})] = E_X[n(\mathbf{r})] + E_C[n(\mathbf{r})] \tag{2.18}$$

in which the two parts of the interaction, exchange X and correlation C are simply linearly added. For the sake of completeness, we warn the reader that formulations of the exchange-correlation functional in which a linear combination is not used exist, as for instance, a family of XC functionals proposed by the group of N. Handy. Since this is neither an

aspect, nor a formulation of interest for the present thesis work, I drop any discussion and invite the readership interested in this issue to look at the related literature. Now, the equation to minimize becomes:

$$E_0[n(\mathbf{r})] = T_S[n(\mathbf{r})] + E_H[n(\mathbf{r})] + E_{XC}[n(\mathbf{r})] + E_{ext}[n(\mathbf{r})] \tag{2.19}$$

Following the variational Hartree method, Kohn and Sham wrote the so-called Kohn-Sham (KS) equation [58], which is an auxiliary equation, resembling the Schrödinger equation,in which the system of N interacting electrons is mapped into a one of N non-interacting electrons evolving in a potential produced by all other electrons, but the density $n(\mathbf{r})$ produced by this system is the same as the interacting one. Practically, we have to solve a single particle Schrödinger-like equation:

$$[-\frac{\hbar^2}{2m}\nabla_i^2 + v_s(\mathbf{r})]\phi_i(\mathbf{r}) = \epsilon_i\phi_i(\mathbf{r}) \tag{2.20}$$

in which ϕ_i is the i-th KS orbital, and ϵ_i the corresponding KS eigenvalue. $v_s(\mathbf{r}) = v_H(\mathbf{r}) + v_{ext}(\mathbf{r}) + v_{XC}(\mathbf{r})$ is the KS effective potential obtained via the variational method, where v_H, v_{ext}, and v_{XC} are given formally by the functional derivatives:

$$v_H(\mathbf{r}) = \frac{\delta E_H[n(\mathbf{r})]}{\delta n(\mathbf{r})} = \int \frac{n(\mathbf{r}')}{|\mathbf{r}-\mathbf{r},|}d\mathbf{r}', v_{ext}(\mathbf{r}) = \frac{\delta V_{ext}[n(\mathbf{r})]}{\delta n(\mathbf{r})} \tag{2.21}$$

The stumbling block still present in this formulation is the fact that v_{XC} is unknown, it does not have an explicit expression as the Hartree term and needs to be approximated. This will be discussed in the next sub-section. The new KS density given by:

$$n_s(\mathbf{r}) = \sum_i^{occ} d_i \langle\phi_i|\phi_i\rangle \tag{2.22}$$

This is a summation over all occupied states, and d_i is the degeneracy of the i-th occupied stats. As a word of warning, we recall that $|\phi_i\rangle$ are not atomic or molecular orbitals, but just the solutions of the KS equation and, in this respect, they are arbitrary provided that the sum of their scalar products gives the exact ground state electron density. Those equations have to be solved self-consistently, which leads to an iterative algorithm as shown in figure 2.1. In this algorithm, one has to choose an initial trial density. Then, by using this density, we construct $v_H(\mathbf{r})$ and $v_{ext}(\mathbf{r})$ from eq. 2.22 and v_{XC}. The (numerical) solution of eq. 2.20 gives us a new set of KS wave functions and corresponding eigen energies, ϕ_i and ϵ_i. Finally a new density can be computed from eq. 2.22. The total energy of the system becomes then:

$$E_{KS} = \sum_i \epsilon_i - \frac{e^2}{2}\int\int d^3r d^3r' \frac{n(\mathbf{r})n(\mathbf{r}')}{|\mathbf{r}-\mathbf{r},|} - \int d^3r n(\mathbf{r})v_{XC}(\mathbf{r}) + E_{XC}[n(\mathbf{r})] \tag{2.23}$$

This procedure is reiterated until the convergence is reached, within a given numerical threshold. Finally, we get $E_{KS}(\mathbf{r}) = E_0(\mathbf{r})$ and the corresponding $n_s(\mathbf{r}) = n_0(\mathbf{r})$, the energy and the wavefunctions of the ground-state.

2.2.3 Local and semi-local approximation of E_{XC}

In the DFT formulation summarized in the former paragraph and formally exact, all the terms have an exact analytical expression with the exception of E_{XC}. This many-body part accounting for exchange X and correlation C interaction is very hard to compute and, still nowadays, we have to resort to approximations and auxiliary assumptions rooted in

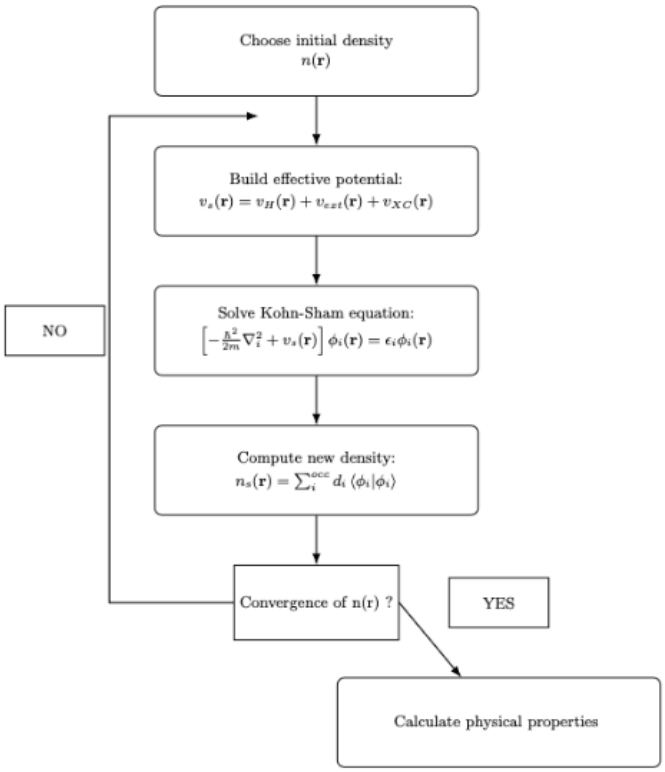

Figure 2.1. Visual representation of the iterative algorithm proposed by Kohn and Sham in order to find the proper electronic density

fundamental physics, but to some extent not always easy to justify. Only *a posteriori* assessment test can support or disprove the validity of the approximated expression adopted. The first approximation of E_{XC} was already proposed made by Kohn and Sham [58] in their original DFT formulation: under the assumption of a homogeneous electron gas slowly varying and minimal density fluctuations, the local-density approximation (LDA) was formulated. The success of the LDA approximation is due to its low computational cost and his relatively good accuracy, at least to some extend. Currently, its limitations and sometimes questionable performance make LDA obsolete. Nonetheless, I give here a brief overview of LDA since it is still the fundamental (and initial) step that allowed any subsequent improvement. In this approximation, the exchange-correlation energy per electron at the point $\mathbf{r}$, $\epsilon_{XC}(\mathbf{r})$, is considered equivalent to the energy of a homogeneous electrons gas of density $n(\mathbf{r})$ at the point $\mathbf{r}$:

$$E_{XC}[n(\mathbf{r})] = \int \epsilon_{XC}(\mathbf{r})n(\mathbf{r})d^3\mathbf{r} \tag{2.24}$$

and we can define:

$$\epsilon_{XC}(\mathbf{r}) = \epsilon_{XC}^{hom}[n(\mathbf{r})] \tag{2.25}$$

Hence, the E_{XC} energy becomes a purely local functional depending on the electronic density at a given coordinate $\mathbf{r}$. The exchange and correlation energies are usually split into two separate contributions, the exchange can be written exactly [59]:

$$\epsilon_{XC}^{hom}[n(\mathbf{r})] = -\frac{3}{4}\left(\frac{3}{\pi}\right)^{\frac{1}{3}} n(\mathbf{r})^{\frac{1}{3}} \tag{2.26}$$

and the correlation contribution is obtained by auxiliary Quantum Monte Carlo calculations [60]. This approximation, always based on the assumption of homogeneous electron

gas, disregards any correction due to impurities in the system. LDA calculations can generally give at least a semi-quantitative estimation of structural properties [61], with errors in the bond length up to $1-2\%$ and about $1^\circ - 2^\circ$ in bond angles in the best performing cases. Sometimes, the precision can be improved by separating the spin contributions and distinguishing the spin-up and spin-down electron densities as two distinct scalar quantities. This is what is called spin-unrestricted approximation or local spin density approximation (LSDA), particularly useful for magnetic properties. Nonetheless, the success of LDA and LSDA in terms of structural properties has been shown to be due mainly to errors compensations: the exchange energy is underestimated while the correlation energy is overestimated.

A first improvement toward the LDA approximation consists in the inclusion of some short-range inhomogeneity into the homogeneous electrons distribution assumption, to account for characteristics of materials departing from a homogeneous electrons gas. This translates into a modification of the E_{XC} term, which becomes dependent not only on the local electronic density, but also on its gradient. This class of XC functional is termed Generalized Gradient Approximation (GGA), and beside the density $n(\mathbf{r})$, the gradient of the density, $\nabla(n(\mathbf{r}))$, is also used as a variational variable. Thus, the XC general formula becomes:

$$E_{XC}^{GGA}[n(\mathbf{r}), \nabla(n(\mathbf{r}))] = \int \epsilon_{XC}^{GGA}[n(\mathbf{r}), \nabla n(\mathbf{r})] n(\mathbf{r}) d^3\mathbf{r} \tag{2.27}$$

As it is well known, there is not a unique way to write a GGA version of the exchange-correlation functional. The GGA correction is also referred to as semi-local, being the gradient the first order variation of the density, thus accounting only for short range non-localities. Moreover, it is often not exactly the gradient but its modulus $|\nabla(n(\mathbf{r}))|$ that it is actually considered in the most common GGA expressions. GGAs represent a general improvement with respect to pure LDA, but they are more demanding in terms of computational effort. Popular GGA functionals include the Perdew-Burke-Ernzerhof (PBE) [62] and the Becke-Lee-Yang-Parr (BLYP) [63, 64] ones. For the scope of this thesis and in view of the performances we could assess, the BLYP formulation is the one adopted in the present work. In this scheme, the exchange functional is the one proposed by Becke (B), while the correlation part is the generalization of the Colle-Salvetti formula derived by Lee, Yang and Parr (LYP functional).

2.2.4 Beyond local and semi-local approximations of E_{XC}

Hybrid functionals

As discussed above, theoretically the formulation of DFT is exact, but when used in computational physics and chemistry, some approximations are needed to express the unknown E_{XC} parts. Improvements and attempts are still an ongoing work, efforts focusing on going beyond the simplification discussed in the former paragraph.

In the case of the exchange part, an exact expression is the one discussed in the case of the Hartree-Fock approximation. A successful idea from which the nowadays hybrid functionals benefit, is the use of a certain percentage of the exact exchange expressed as in Hartree-Fock to complement (at least in some way) local and semi-local descriptions of the XC interaction. Since the exact exchange implies the calculation of cross-products of all the wavefucntions of a given system, the computational workload increases significantly for these hybrid functionals compared to the usual LDA/GGA methods. Two of the most common hybrid functionals are the B3LYP and PBE0 [65], the latter subsequently generalized by the group of Scuseria and known as HSE06. in the case of B3LYP, Becke proposed a reformulation [66] of his own XC functional by parameterizing three contributions. One of these contributions is the LYP correlation energy, while for the exchange

the formula of Becke and the exact exchange are used. The B3LYP expression becomes then:

$$E_{XC} = E_{XC}^{LSDA} + a_0(E_X^{exact} - E_X^{LSDA}) + a_X \Delta E_X^{B88} + a_C \Delta E_C^{LYP} \tag{2.28}$$

where a_0, a_X, and a_C are semiempirical coefficients to be determined by an appropriate fit to experimental data, E_X^{exact} is the exact exchange energy (i. e. the computationally most expensive part of the algorithm), ΔE_X^{B88} is Becke's 1988 gradient correction (to the LSDA) for the exchange energy, and ΔE_C^{LYP} is the mentioned LYP gradient correction for the correlation contribution. This method was originally tested with a Perdew-Wang gradient correction for the correlation, instead of the LYP one, but then abandoned in view of some shortcomings.

Van der Waals correction

While the inclusion of a given percentage of exact exchange helps in improving significantly the exchange interaction, the correlation part still suffers from the limitations that a GGA implies. Namely, long-range correlations are still missing. Nonetheless, these are dominating in non-bonding interactions, particularly in the stacking of layered materials or nucleic acids. To compute these subtle and important contributions, that are neither chemical nor hydrogen bonds, long-range van der Waals (vdW) interactions must be included. This can be done using damped dispersion models, where the damping serves to avoid double counting at short distance, where the density gradients in GGAs are already active to account for these short-range correlations. Common models proposed over the years include the Elstner *et al.* [67] or the Mooij *et al.* [68] models, which share the same implementation. More recent advances have been obtained by the semi-empirical vdW corrections proposed by Stefan Grimme [69].

In this thesis the Grimme model is used. According to this formulation, the vdW energy contribution is written as a dispersive energy between atoms separated by a distance (R_{ij}) in a system of N_{at} atoms:

$$E_{dis}(R) = -\alpha \sum_{i,j}^{N} {}_{at} \frac{C_{ij}}{R_{ij}^6} f_{dmp}(R_{ij}) \tag{2.29}$$

In this formula, their numerical values of the C_{ij} coefficients are taken from [69], while $f_{dmp}(R_{ij})$ is a damping function that is equal to one at long distance and zero beyond a cutoff distance ($R > R_{cutoff}$) again tabulated by S. Grimme and introduced to avoid the double counting mentioned above. The paramter α in front of the formula is a scaling factor depending on the functional used for the DFT scheme and for the majority of the GGA functionals currently used, Grimme has provided accurate numerical data. This vdW dispersion energy is linearly added to the DFT total energy functional and this combination is referred to as DFT-D. In this thesis, the DFT-D2 version is used, where the additional label 2, refers to the first amendment done by Grimme and his group.

The use of semi-local exchange–correlation functionals augmented with an explicit dispersion correction has become a standard strategy for first-principles molecular dynamics simulations of extended carbon-based materials. In this work, the BLYP functional combined with Grimme's D2 [70, 71] dispersion correction is employed, as it offers a well-established compromise between computational efficiency and physical accuracy. According to the calculations we performed on different systems, the BLYP functional provides a more accurate description of localized chemical bonding compared to other functionals, such as PBE, which are constructed to recover the asymptotic limit of the homogeneous electron gas [72]. While the BLYP functional accurately captures covalent C–C bonding and the local electronic structure, it lacks long-range van der Waals interactions, which are essential for a realistic description of low-dimensional and flexible carbon systems. The D2 dispersion correction effectively restores these missing interactions at negligible computational

cost by introducing pairwise atom–atom contributions, thereby improving the accuracy of interatomic forces and equilibrium distances [72, 73].

2.2.5 Pseudopotentials and wavefunctions

Solving the Kohn-Sham problem by computing all the electronic wavefunctions of the atoms composing a system is still a huge computational task also within the DFT framework. The number of states is indeed huge and most of them do not actually contribute to any chemical bonding, but remain as inert core states not participating to the physics/chemistry of the whole system and representing a short-scale tough problem. In order to overcome the workload represented by the huge amount of orbitals of the entire system, we can resort to pseudopotentials which mimic the exact behavior of an all-electron calculation at least beyond a certain threshold distance, but that do not contain the core electrons which are then not treated explicitly and not expanded on the basis set used to represent valence electrons. During a DFT calculation, the number of KS

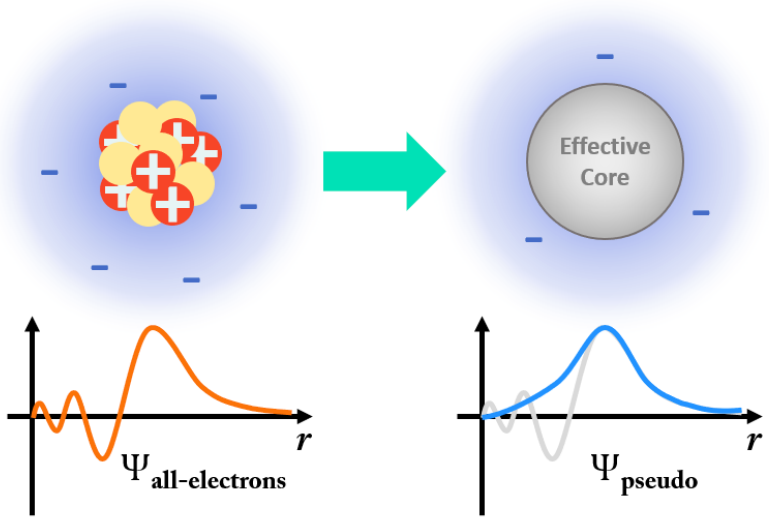

Figure 2.2. Comparison between an all-electron description of an atomic wavefunction (left panel) and the corresponding one in the case of the use of a pseudopotential. Beyond the cutoff radius, both potentials and wavefunctions are identical.

equations that we need to solve is equal to the number N_e of electrons in the system. For large and complex systems, N_e can become not affordable unless pseudopotentials (PP) [74, 75] are used or, alternatively, frozen-core methods as in the projector augmented-wave (PAW) scheme, which is however beyond the scope of this paragraph and not used in this doctoral work. The construction of a PP starts from the atomic radial Schrödinger or Dirac equation for the specific chemical element considered. Then a fitting procedure is used to construct the PP and the associated nodeless pseudo-wavefunction as the one illustrated in the figure. Thus, in the PP created from the real all-electron potential, the core electrons are eliminated. Yet, outside the cutoff region, the PP and the real all-electron potential are identical. The type of PPs used in this thesis are the norm-conserving ones constructed according to the scheme proposed by Troullier and Martins [76] for carbon and oxygen. For hydrogen an analytical von Barth-Car PP [77] has been use and in the case of d for Hydrogen. For the heavy Co atom, we resorted to a Goedecker-Teter-Hutter pseudopotential [78] which includes some semi-core states for a more precise description of the electronic structure.

Summarizing, the Hartree and the exchange correlation potential are computed only for the valence electrons, whereas the electron-nucleus interaction is described by a PP.

Concerning the mentioned basis set, by limiting my discussion to the one used in all my doctoral project, I wish to recall that Kohn-Sham orbitals are expansed on a plane waves (PW) basis set, particularly useful since not depending on nuclear coordinates (hence not requiring tedious calculations of Pulay's forces) and well suited for periodic systems. By resorting to the Bloch's theorem [79], we can express an electronic wavefunction as a set of PWs (Fourier series of Bloch wavefunctions) as:

$$\psi_i(\mathbf{r}) = \sum_G c_{i,\mathbf{k}+\mathbf{G}} exp[i(\mathbf{k}+\mathbf{G}).\mathbf{r}] \tag{2.30}$$

Where $\mathbf{G}$ is the reciprocal lattice vector, and $\mathbf{k}$ is the wave vector in reciprocal space. Considering that the coefficients $c_{i,(\mathbf{k}+\mathbf{G})}$ corresponding to PW to small kinetic energy $E_{PW} = \frac{\hbar^2}{2m}|\mathbf{k}+\mathbf{G})|^2$ are dominating with respect tp those with large E_{PW}, we can limit the sum to some computationally affordable value. Thus, the theoretically infinite PW basis set (spanning a Hilbert space) can be truncated for energies larger than a given cutoff energy $E_{PW} > E_{cutoff}$. E_{cutoff}. This cutoff has clearly to be large enough to accurately represent wavefunctions and total energy, thus compromises have to be found depending on the size of the system and the available high-performance computing architectures. Of course, a large E_{cutoff} translates into more expensive calculation, thus special attention must be paid in selecting its value without compromising the quality of the results.

2.3 First Principle Molecular Dynamic

The arising of computational sciences and the continuously growing computer capability of HPC platforms boosted simulations and modeling in modern research, making computer modeling a sort of virtual environment able to complement experiments or to perform virtually experiments that would be too expensive for practical laboratory realization. Yet, we have to keep in mind all the assumptions and simplifications introduced in our theoretical framework in comparing to experiments and experimental conditions at which laborartory tests are done. In the approaches used here, complex mathematical equations are used to determine plenty of microscopic properties from which macroscopic physical quantities of a system have to be extracted for a proper comparison and to verify the predictive power of models and algorithms used.

A clear bottleneck in the simulation of high complexity systems at an atomic level is the inherent computational cost which is limited on one hand by the fundamental physics (e. .g. quantum mechanics and related short quantum time scales) and, on the other hand, by the computational equipment available and the current technological limits in computing power. A typical stumbling block is the affordable simulation time of a complex atomic system evolving dynamically. Depending on the level of the theory (classical or quantum-mechanics based dynamics) and the HPC capability, nanosecond (classical) or picosecond (quantum-mechanics) time scales can be reached. In the context of this doctoral project, I can anticipate here that, for instance, the maximum frequency ω that can be *seen* by a dynamical computer simulation is $\omega = 2\pi/\text{max. simulationtime}$, with the consequent limits that nano- or pico-second time scales imply. However, atomistic methods provide access to a wealth of microscopic structural and dynamic properties, spatial and temporal response of atoms can be tracked, and ensemble or time averages, within the ergodic principle, can be used to compute measurable quantities.

2.3.1 Molecular dynamics

One of the most successful atomistic modeling used in condensed matter is the molecular dynamics (MD) [80, 81], whose development started in the early 1950s, immediately after

the Second World War. The MD is a numerical technique for solving Newton's equations of motion of an ensemble of particles and that reproduces the time-dependent behavior of many-body systems on a given time scale in the sense specified above. This method enables the calculation of both equilibrium static properties (structure, topology) and dynamic properties (transport, phase change, etc.) from time-averaged trajectories at the equilibrium, thus establishing a bridge between statistical mechanics and thermodynamics. Historically speaking, the first example of MD documented is the one of Alder and Wainwright (1957) [82] aimed at exploring phase transitions in hard-sphere systems. And this started a whole new field still under improvement and development nowadays.

Modern MD simulations, empowered by high-performance computing, can access longer time scales and larger system sizes. These simulations are now routinely used in materials science, chemistry, biophysics, and nanotechnology to probe atomic mechanisms of many macroscopic properties that can be expressed in terms of one or more microscopic variables. MD has also earned the status of "virtual experiment" able to offer real-time insights into molecular processes otherwise inaccessible to direct experimental observation.

In MD the type of the interaction potential acting among the particles plays a crucial role in determining accuracy and affordable time of the simulation. Depending on the type of potential used, MD can be classified into two main categories: Classical Molecular Dynamics (CMD), which uses empirical or semi-empirical potentials either analytical or numerical (as in the case of Machine-Learning derived potentials), and Ab Initio Molecular Dynamics (AIMD), or First-Principle Molecular Dynamics (FPMD), where the potential is computed from the fundamental quantum mechanics, namely in its DFT formulation discussed in this chapter. Empirical/semi-empirical potentials contain adjustable parameters that have to be fitted to experiments and/or quantum mechanical auxiliary calculations to be able to catch the targeted physical properties of the material, but they do not account for the electronic degrees of freedom and related quantum effects, although they may well reproduce structural properties and allow dynamical simulations on a longer time scale with respect to AIMD. Conversely, AIMD has the advantage of being robust and independent of the system under study, not relying on adjustable parameteres, thus being more general in terms of applicability. Its *driver* is the DFT formulation of the many-body quantum mechanics and allows to include explicitly the electronic structure in the time evolution of the system. Two main methods are used to integrate numerically the underlying equations of motion, the Born-Oppenheimer (BOMD) and Car-Parrinello (CPMD) ones. The choice depends on the level of accuracy, execution speed and type of system (insulator, semiconductor, metal, etc.) targeted. Any choice, nonetheless, passes across the calculation of the forces acting on each atom via the potential U, namely:

$$F_i(\mathbf{R}) = -\frac{\partial U(\mathbf{R})}{\partial R_i} \tag{2.31}$$

for a system with N particles whose positions are identified by the vectors $\mathbf{R}$ ($i = x, y, z$). Thus, the motion of a particle is described by the Newton's equation of motion (EOM):

$$\frac{d\mathbf{p}_i}{dt} = F_i(\mathbf{R}) \tag{2.32}$$

where the force F_i, computed as above, acts on the i-th particle. The practical solution of Newton's equations for the whole ensemble of particles is an iterative procedure making use of appropriate numerical integrators. Hence, provided an initial configuration, forces are calculated, the EOM of the corresponding system are integrated over a discretize amount of time (called time step in MD codes), and the atoms positions and speeds are updated to a subsequent position and velocity, resulting in a sequence of configurations (trajectory) evolving in time. For the numerical integration, the most common methods are the Euler

algorithm and the Verlet one [83], which is based on an expansion in time in terms of a Taylor series, both backward and forward in time by virtue of the time reversibility of the microscopic equations of motion. We get then:

$$\mathbf{R}_i(t+\delta t) = \mathbf{R}_i(t) + v_i(t)\delta t + \frac{1}{2}\frac{(\delta t)^2}{M_i}F_i(\mathbf{R}) + \frac{1}{6}\frac{\delta^3\mathbf{R}_i(t)}{\delta t^3}\delta t^3 + o(\delta t^4) \tag{2.33}$$

and

$$\mathbf{R}_i(t-\delta t) = \mathbf{R}_i(t) - v_i(t)\delta t + \frac{1}{2}\frac{(\delta t)^2}{M_i}F_i(\mathbf{R}) - \frac{1}{6}\frac{\delta^3\mathbf{R}_i(t)}{\delta t^3}\delta t^3 + o(\delta t^4) \tag{2.34}$$

Thus, by adding these equations, we obtain the Verlet algorithm used to update the positions:

$$\mathbf{R}_i(t+\delta t) = 2\mathbf{R}_i(t) + \mathbf{R}_i(t-\delta t) + \frac{(\delta t)^2}{M_i}F_i(\mathbf{R}) + o(\delta t^4) \tag{2.35}$$

The Verlet algorithm is more stable than the Euler algorithm over the interesting time scales of either classical or first-principle MD, because the next position ($t+\delta t$) depend on the actual position (t) and the previous one ($t-\delta t$) and the propagating error of this algorithm is of the order $\mathcal{O}(\delta t^4)$, whereas the Euler method it correct up to $\mathcal{O}(\delta t^2)$. The precision and stability of this class of algorithms strongly depends on the choice of the integration time step δt. A short δt implies a higher precision and a better stability, but the computational cost (simulation time needed to cover a given maximum physical time) become consequently higher. On the contrary, a long δt allows to cover more rapidly longer simulation times, but accuracy and stability can become questionable. All-in-all, the right choice it is always a matter of compromise.

In order to reduce the computational workload, some workarounds are available in MD. In a system with a clearly identified symmetry or to study intensive properties (i. e. properties not depending on the system size), suitable boundary conditions can be applied used. Thus, an infinite system can be mimicked by a finite one bordered by its periodically repeated images; generally a simulation virtual cell is created containing all the atoms explicitly included to represent the studied system, and when a particle exits from one side of the simulation cell, it re-enters from the opposite side. A constraint here, is that in AIMD the wave functions of the system must have the length of the box as maximum possible dispersion or, preferably, should decrease (numerically) to zero at the border of the simulation cell if the latter is large enough and the system is confined in the inner region of the cell, far from its borders. This last condition applies to clusters or one-dimensional-like objects as the ones that will be discussed and detailed in the next chapters.

2.3.2 Born-Oppenheimer molecular dynamic

The BOMD is based on the BO approximation, already introduced in this chapter, in which the motion of ions (nuclei) and electrons can be decoupled. As mentioned, this approximation is justified by the difference of mass and speed between the two ensembles of degrees of freedom. From the total energy of the system, written as in the DFT framework outlined in the first part of this chapter, gradients can be computed, providing the forces acting on the nuclei, to be used to solve the Newtonian equations of motion. The nuclear positions are then updated classically, as in the Verlet algorithm introduced above, while the electronic structure, treated quantum-mechanically has to be recomputed at each time step. Practically, according to the ions positions, the electronic structure is optimized by solving the time-independent stationary Schrödinger equation, or more precisely the Kohn-Sham equations for the electronic orbitals, and then the ions is propagating using classical

EOM in which the force field is generated by the other ions and the electronic structure. The iterative procedure is thus summarized by following set of coupled equations: ,

$$\begin{cases} M_I \ddot{R}_I &= -\nabla E_{KS} \\ H_e \Psi_i &= E_{KS} \Psi_i \end{cases} \tag{2.36}$$

Here, M_I is the mass of nucleus I at position $\mathbf{R}_I$, ψ_i is KS single particle orbital of each electron in the system describing the DFT ground state and H_e is the corresponding effective KS one particle Hamiltonian. Optimizing the electronic structure at each step ensures that the electronic structure trajectory strictly follows the ground state, namely the minimum of the BO potential energy surface (PES). This is however the shortcoming of the BOMD approach: in principle the electronic structure has to be fully converged at each dynamical step and such an operation can become excessively time consuming if a tight convergence criterion is used. Conversely, is the convergence is not optimal, errors accumulate at each time step and the conservation of the constants of motion along the trajectory can be lost for more or less long simulation times. Again, also in this cases comprormises have to be found between stability/accuracy and affordable computational workload.

2.3.3 Car-Parrinello molecular dynamics

Introduced by R. Car and M. Parrinello in 1985 [84], the Car-Parrinello Molecular Dynamics (CPMD) provides an alternative way to generate a dynamical trajectory within first-principle based methods. At variance with the BOMD, the CPMD approach avoids solving iteratively the KS equations at each movement of the ions. Instead, the electronic wavefunctions are computed only at the beginning of the dynamics, at the first time step, by solving the KS equations in the usual way. Then, the KS orbitals obtained are used as additional dynamical variables and included in the extended Lagrangean (or Hamiltonian). They have then their own EOM (Euler-Lagrange EOM) and evolve with a fictitious dynamics alongside the ionic positions. This treatment of the electronic orbitals as dynam-

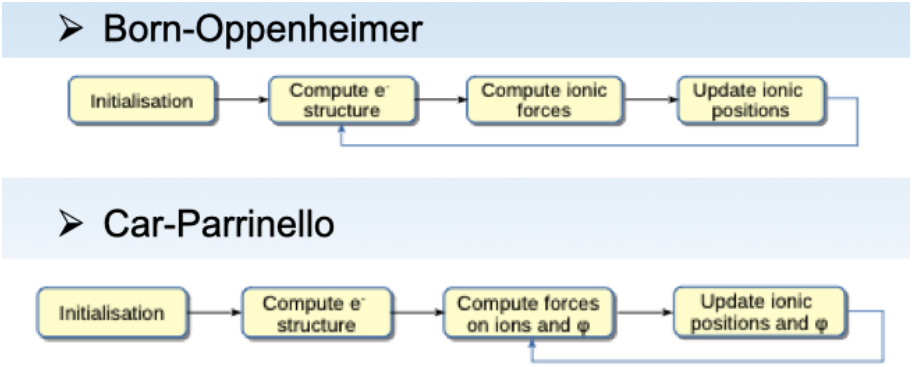

Figure 2.3. Difference of implementation between the BOMD and the CPMD methods.

ical variable is mathematically formalized through an extended Lagrangian that unifies classical ion dynamics and quantum electronic structure propagation. Moreover, within this method, all external additional variables such as thermostats (more detail in section ..), barostats, reaction coordinates, etc. can be added extending further the Lagrangean and allowing to write consistently Euler-Lagrange EOMs for each new dynamical variable α_q introduced. Such a Lagrangean is:

$$\begin{aligned} \mathcal{L}^{CP} = \textstyle\sum_i \mu \int \dot{\psi}_i^*(\mathbf{x}) \cdot \dot{\psi}_i(\mathbf{x}) d^3x + \frac{1}{2} \sum_I M_I \dot{R}_I^2 + \frac{1}{2} \sum_q \mu_q \dot{\alpha}_q^2 \\ - E^{DFT}[\psi_i, \mathbf{R}_I, \alpha_q] + \textstyle\sum_{ij} \Lambda_{ij} \big(\int \psi_i^*(\mathbf{x}) \psi_j(\mathbf{x}) d^3x - \delta_{ij} \big) \end{aligned} \tag{2.37}$$

Thus, in the extended Lagrangean, beside the classical dynamical variables of any MD, atomic position R_I and masses M_I, we have a fictitious mass for the electronic orbitals μ which controls the adiabaticity of the system all along the dynamics and acts as the parameter regulating the proximity of the electronic structure to the ground state as demonstrated by the theorem of Bornemann and Schütte [85]. Summarizing, the first term in the Lagrangean is the fictitious kinetic energy of the electronic degrees of freedom, the second is the usual kinetic energy of the classical nuclei, the third one the kinetic term of any supplementary dynamic variable, followed by the DFT total energy functional. The last term is the new ingredient needed to keep track that wavefuntions are quantum objects and is a constraint to ensure the orthogonality and the proper normalization of the orbitals. Form this Lagrangian, in the usual Euler-Lagrange way, we get the following coupled EOMs:

$$\begin{cases} M_I \ddot{R}_I &= -\nabla E_{KS} \\ \mu \ddot{\psi}_i(\mathbf{r}) &= -\frac{\delta E_{KS}}{\delta \psi_i^*(\mathbf{r})} + \sum_j \Lambda_{ij} \psi_j(\mathbf{r}) \\ \mu_q \ddot{\alpha}_q &= -\frac{\delta E_{KS}}{\delta \alpha_q} \end{cases} \tag{2.38}$$

This pseudo-classical propagation of the KS orbitals as additional electronic degrees of freedom in the EOM is what allows to avoid the resolution of the KS DFT equations at each time step along the trajectory generated by the CPMD dynamics. The price to pay, beside the need of a sufficiently small time step, is that the orbitals do not stick exactly to the minimum of the BO PES and the resulting trajectory is not exactly a BOMD one, but oscillates around it dynamically and coincides with the BOMD only on average. Adiabaticity is a key requirement in CPMD to ensure a proper separation between electronic and nuclear degrees of freedom. For the adiabatic approximation to remain valid, the electronic transition frequencies must be significantly higher than system's maximum phonon (ionic) frequencies. A central factor in maintaining this condition is a careful selection of the fictitious mass parameter μ that, as mentioned above an demonstrated by the Bornemann-Schütte theorem, regulates the degree of adiabaticity of a CPMD dynamics. As usual in numerical simulations, also in this case a good compromise has to be found: μ should be small enough to minimize deviations from the BO PES, yet large enough to allow for the use of efficient time steps to make affordable simulations over meaningful time scales. A criterion proposed by Pastore and coworkers is that in the CPMD formalism the electron transition frequency is given by [86]:

$$\omega_{ij} = \sqrt{\frac{\epsilon_i - \epsilon_j}{\mu}} \tag{2.39}$$

where ϵ_i is $i-th$ eigenvalue of the $i-th$ unoccupied state and ϵ_j, the $j-th$ eigenvalue of the $j-th$ occupied KS orbital. We obtain the minimum transition frequency ω_{min} when $(\epsilon_i - \epsilon_j)$ is the smaller possible, but not zero. This implies that an energy gap E_{gap} must exist between the HOMO (highest occupied molecular orbital) and the LUMO (lowest unoccupied molecular orbital) bands. A maximum frequency ω_{max} can also be identified according to the maximum possible energetic value $(\epsilon_i - \epsilon_j)$ which has to be compatible with the maximum plane wave energy E_{cut}, defined in the previous section, and that fixes our upper limit. We can then have a rough estimation of the maximum time step that can be chosen:

$$\delta t_{max} \propto \sqrt{\frac{\mu}{E_{cut}}} \tag{2.40}$$

showing that, again, μ is a key parameter in CPMD and must be carefully determined based on the specific system being studied. Adiabaticity has to be kept all along the trajectory and this translates into an accurate choice of μ, useful to minimize as possible the computation workload and to grand numerical conservation of the constants of motion at least on the time scale of the simulation.

2.3.4 Thermodynamic Ensembles

In any MD, either classical of DFT-based, the number of particles inside a given simulation box does not vary (I disregard here any Grand Canonical ensemble, since no simulation presented in this work has been done with a variable number of particles). Given this restriction, the natural ensemble in which an MD trajectory evolves is the Microcanonical Ensemble (NVE). The acronym NVE means that the number of particles (N), the volume of the simulation cell (V) and the energy of the system (E) are the constants of motion during the dynamics. The NVE ensemble corresponds to a system where all the configurations Ω_E having an energy equal to E have the same probability to occur. This is expressed as a uniform probability

$$p_E = \frac{1}{\Omega_E} \tag{2.41}$$

Another equally important thermodynamic ensemble in which a system can evolve along an MD is the Canonical Ensemble NVT, where the constants of motion are the Temperature(T) instead of the energy of the microcanonical ensemble, the volume (V) and the number of particles (N). The NVT system is in thermal equilibrium with a heat bath at constant temperature. The temperature of a system is defined as in statistical mechanics:

$$T = \frac{1}{3k_B}\langle\sum_I m_I \mathbf{v}_I^2\rangle \tag{2.42}$$

Where k_B is the Boltzmann constant and m_I and $\mathbf{v}_I$ the mass and velocity of the $I-th$ particle. The concept of "constant temperature" is questionable in a system, especially of finite size, in which the particles' speed fluctuates continuously. This has made the control of the temperature of a system a big challenge in MD simulations, until the brilliant idea originally proposed by S. Nosé. Indeed, this has become one of the most popular methods to cope with these fluctuation and to keep the system, on average, to a given target temperature. The method is universally known as the Nosé-Hoover thermostat. The idea behind this thermostat is to use a dynamical variable that can rescale the speed of the atoms but in such a way that the canonical Boltzmann distribution is preserved. The formalism is the one proposed by Nosé in 1984[87] with a thermostat fully compatible with statistical mechanics; this model was later refined by W. G. Hoover [88]. As mentioned, this method introduces a fictitious degree of freedom ζ coupled to the system's dynamics, simulating frictional forces that allow for acceleration or deceleration of the atomic motion (velocity of the atoms) to reproduce fluctuating velocity distribution around a given temperature T. Such an additional variable evolves according to extended Lagrangean or Hamiltonian of the MD, enabling correct sampling of the canonical ensemble.

Within my collaboration in the ADynMat consortium, I contributed to this temperature control method in the course of my Ph. D. studies, finalized in a publication in 2024[89],. In this work, we have demonstrated that Nosé's initial formulation already encompasses all the elements that characterize the Nosé-Hoover approach. The expression for the degree of freedom that represents the action of the thermostat naturally emerges when Nosé's equations are written in terms of "real time" evolution. I reacll that Nosé's equations were initially expressed in terms of a "virtual time". By introducing this new degree of freedom, the EOMs become:

$$M_I\ddot{R}_I = -\nabla E_{KS} - M_I\dot{\zeta}\dot{R} \tag{2.43}$$

Here we clearly see that ζ directly affects the atomic velocities and behaves as a friction term. This new dynamical variable is thus coupled to the EOMs of the system (equations 2.38) and controls directly the kinetic energy of the atoms by balancing it with the energy

of the thermostat. The EOM representing the evolution of the thermostat variable ζ is:

$$Q\ddot{\zeta} = \sum_I M_I \dot{R}_I - (3N+1)k_B T \tag{2.44}$$

where $3Nk_BT$ is the energy associated with the thermostat, Q is a mass-like parameter that controls the coupling and the thermostat frequency, whose role is not too different from the electronic fictitious mass discussed in the case of the CPMD EOMs.

2.4 Electromagnetic properties calculations

Electromagnetic properties are usually expressed as measurable quantities depending on the frequency. For any FPMD simulation, and in general, for any time series of physical variables generated by dynamics, we need to move from the time domain to the frequency domain, hence in the reciprocal space of of time. This translates into an appropriate Fourier transform that allows for this operation. While the time-to-frequency Fourier transform requires long time to compute low frequency (hence it is referred to as *intensive* method), distance/impulsion Fourier transform needs large system sizes for accurate estimations (hence is is classified as *extensive* method).

2.4.1 Electromagnetic absorption

As explained in chapter 1, from the Poynting theorem, we can obtain a relation between the electromagnetic absorption of a medium and both the complex dielectric permittivity and the complex magnetic permeability. In material science, and particularly in the simulation framework in which this research work is conducted, such relation becomes particularly useful to extract physical observables from the time evolution of microscopic quantities. Specifically, what we have available *on the fly* during an AIMD simulation are atomic positions and velocities, electronic density, spin density and dipole moments at each instant of the dynamical simulation. Coming directly to the quantities interesting for the scope of my work, a crucial one is the complex refraction index:

$$\tilde{n} = \sqrt{\frac{\epsilon\mu}{\epsilon_0\mu_0}} \tag{2.45}$$

where ϵ is the complex dielectric permittivity and μ the complex magnetic permeability. Since only the product of the two is involved, these two quantities (ϵ, μ) can be treated separately and for a non-magnetic system the expression can be simplified as $\tilde{n}^2 = \frac{\epsilon}{\epsilon_0}$. Analogously, in a fully magnetic system we have $\tilde{n}^2 = \frac{\mu}{\mu_0}$. The related absorption coefficient can be expressed in terms of the dielectric susceptibility χ_ϵ:

$$\alpha_\epsilon(\omega) = \frac{\omega}{cn(\omega)\epsilon_0}\Im[\epsilon(\omega)] = \frac{\omega}{cn(\omega)}\Im[\chi_\epsilon(\omega)] \tag{2.46}$$

in which $\chi = 1 - \epsilon_r$, with the relative dielectric permittivity given by $\epsilon_r = \frac{\epsilon}{\epsilon_0}$, and $n(\omega)$ is the real part of the refractive index. Similarly, if we consider a magnetic medium, an identical relation can be found between $\alpha_M(\omega)$ and $\chi_M(\omega)$, the magnetic absorption coefficient and the magnetic susceptibility, respectively. Connections between dynamically obtained quantities and macroscopic observable rely, as usual, on statistical physics, and specifically, for the cases of interest in the context of this thesis, the linear response theory (LRT). The LRT describes the behavior of a system in the context of the fluctuation the fluctuation–dissipation theorem, originally proposed by H. Callen and T. Welton in 1951 [90] to describe the relation between the dissipative part of an admittance function and the correlation spectra of the corresponding physical quantities. Since the complex part

of the magnetic and dielectric susceptibility represent the dissipative part of the susceptibility, R. Kubo [91] proposed a versatile formula able to accurately describe magnetic and dielectric susceptibility within this framework and grounded into quantum mechanics. The fluctuation–dissipation theorem can then be reformulated in terms of the following formula:

$$\Im[\chi_\epsilon(\omega)] = \frac{\tanh(\beta\hbar\omega/2)}{\hbar}\int_{-\infty}^{+\infty} dt e^{-i\omega t}\langle \mathbf{P}(0)\mathbf{P}(t)\rangle \tag{2.47}$$

where $\beta = 1/k_B T$, T being the temperature of the system, k_B the Boltzmann's constant, $\hbar$ the Planck's constant, and c the speed of light. In the case of the dielectric function, the time evolving quantity to be considered is the dipole moment $\mathbf{P}(t)$ of the system. Analogously, for a magnetic system, the corresponding frequency dependent quantity becomes the magnetic susceptibility $\chi_M(\omega)$, computed from the time evolving spin magnetization $\mathbf{M}(t)$. Finally, the formula used to extract the infrared (IR) absorption spectrum per unit volume within the LRT becomes [92] becomes the Fourier transform of the dipole-dipole autocorrelation function:

$$\alpha_\epsilon(\omega) = \frac{4\pi\omega\tanh(\beta\hbar\omega/2)}{3V\hbar cn(\omega)}\int_{-\infty}^{+\infty} dt e^{-i\omega t}\langle \mathbf{P}(0)\mathbf{P}(t)\rangle \tag{2.48}$$

accounting for the dielectric absorption and

$$\alpha_M(\omega) = \frac{4\pi\omega\tanh(\beta\hbar\omega/2)}{3V\hbar cn(\omega)}\int_{-\infty}^{+\infty} dt e^{-i\omega t}\langle \mathbf{M}(0)\mathbf{M}(t)\rangle \tag{2.49}$$

for the magnetic absorption. The factor $4\pi/3$ that appears in the equation 2.48, comes from the Lorentz local field approximation. The macroscopic dipolar moment is related with local dipole moment by the relationship $\mathbf{P}_{macro} = \frac{1}{3\epsilon_0}\mathbf{P}_{local}$, in CGS units $(4\pi\epsilon_0)^{-1} = 1$, thus we get $\mathbf{P}_{macro} = \frac{4\pi}{3}\mathbf{P}_{local}$. Finally, from equation 2.45, we can see that the total absorption spectrum is the product of the dielectric absorption and the magnetic absorption $\alpha(\omega) = \alpha_\epsilon(\omega)\alpha_M(\omega)$. From the absorption spectra, one can easily extract the imaginary part of the complex dielectric function by exploiting equation 2.46. The real part, instead, can be calculated using the Kramers-Kronig relation, if $\tilde{\epsilon}(\omega) = \epsilon_1(\omega) + i\epsilon_2(\omega)$, thus, from $\epsilon_2(\omega)$ computed via the fluctuation-dissipation theorem, $\epsilon_1(\omega)$ becomes:

$$\epsilon_1(\omega) = 1 + \frac{2}{\pi}P\int_0^\infty \frac{\omega'.\epsilon_2(\omega)}{\omega'^2 + \omega^2}d\omega' \tag{2.50}$$

where P is the Cauchy principal value of the integral.

2.4.2 The Maximum entropy method

In the practical handling of numerical data that imply a conversion from the time domain to the frequency domain, as mentioned in the previous section, the Fourier transform (FT) is the most popular algorithm. Its success is due to its versatility, the wide range of applications and the possibility of fast and efficient implementation in computer codes, including parallelism and distributed algorithms. Yet, this method is not free from shortcomings. In particular, FT is sensitive to noisy or truncated data, it does not account for instrumental distortions and has difficulties in handling high frequencies resulting from sampling problems such as, for instance, not optimal time steps in our MD or FPMD numerical integration of the EOMs. Method able to reduce noise in a data set or to account for instrumental distortion have been proposed to overcome this stumbling block. Among the algorithms available to this aim, one that has proved its utility in a variety of fields is the maximum entropy method (MEM) [93]. It is a tool that, for given N points in a time-domain data set x_i $(i = 1, \ldots, N)$, can filter out the noise and produce a corresponding spectra $\mathbf{y}$ that is consistent with x_i and that can generate a frequency spectra $\mathbf{p}$

without losing information or missing important physical features of the response. A rich literature is available on the MEM. For this reason, I limit here the discussion to the main points essential to get the gist of how it works. To determine if a "mock data" ensemble $\mathbf{y}$ is consistent with x_i, we resort to the χ^2 in which a parameter σ_i is associated to each numerical data.:

$$\chi^2 = \sum_{i=0}^{N} |y_i - x_i|^2/\sigma_i^2 \tag{2.51}$$

σ_i being the statistical uncertainty in x_i. When $\chi^2 = 2N$, the "mock data" y is considered consistent with x_i. Then, the frequency spectra $\mathbf{p}$ is calculated using a simple linear operation $\mathbf{p}$=$\mathbf{R}\mathbf{x}$ where $\mathbf{R}$ is a matrix, which is usually a FT [94] but can be enhanced by including convolution to describe specific phenomena if needed. Finally, the spectra with the minimum information is selected among all the consistent spectra that can be computed [95].

Since this method also rely on FT, some claim that this method is purely cosmetic. Without entering in this dispute, I wish to bring to the attention some consideration proposed by J. A. Jones and P. J. Hore [96], who demonstrated that under certain conditions: (i) $N_f = N_{t_i}$ (as many complex point in the time domain as there are in the frequency domain); (ii) the noise level is the same for all the spectra; (iii) R contains only a FT, hence a frequency spectrum; (iv) there is no truncation in the free induction decay. Without arguing if MEM is purely cosmetic, I remark that in general those conditions are not all satisfied at the same time. Thus, generally the MEM enhances interesting (for the scopes of my work) peaks and the resolution remains acceptable even for incomplete and noisy data [97].

2.4.3 Wannier functions and centers

Understanding of the energy band, chemical bonds, and precise (local) electronic structure around the atoms of interest is generally a hard task in DFT calculations, This is due, on one hand, to the fact that the theory considers as actual variable only the global distribution of electrons, i. .e. the electronic density function, on the other hand on te fact that KS wavefunctions are just an auxiliary basis set whose only scope is to give the exact ground state density of all their square moduli are summed up. Given this scenario, DFT is in principle unable to provide explicit contributions of each electron composing the system, although often KS orbitals are used as roughly representative of molecular orbitals. Attempts have been done in the past to partition the charge density in contributions centered around specific atoms or bonds. Yet, the majority of them rely on arbitrary assumptions *ad hoc* and cannot be generalized to any system. An unbiased way to recover electronic information in the neighborhood of single atomic sites is the one proposed by Marzari and Vanderbilt [98] allowing to get localized wavefunctions via a unitary transformation of the KS orbitals, obtaining the so-called Maximally Localized Wannier Functions (MLWF). Wannier functions (WF) w_{nR}, which are in practice what chemists call Boys-Foster orbitals, depend on an index n ranging from 1 to the maximum number of wavefunctons (electrons) of the system and $\mathbf{R}$ is the Bravais Lattice vector. The unitary transformation of the Bloch/KS wavefunction that allows to compute the WFs is:

$$w_{nR}(\mathbf{r}) = \frac{V}{(2\pi)^3} \int_{BZ} dk \psi_{n\mathbf{k}}(\mathbf{r}) e^{-i\mathbf{k}.\mathbf{R}} \tag{2.52}$$

where the integration runs over the first Brillouin zone. Among all the possible equivalent unitary transformations, Marzari and Vanderbilt proposed to select te one that minimizes the spread. To this aim, they introduced a unitary rotation matrix $U^{\mathbf{k}}_{mn}$ defined as:

$$\psi_{n\mathbf{k}}(\mathbf{r}) = \sum_m U^{\mathbf{k}}_{mn} \psi_{m\mathbf{k}}(\mathbf{r}) \tag{2.53}$$

The problem is then reduced to find the right $U^{\mathbf{k}}_{mn}$ that gives to the most localized ω_{nR}. To this aim, they make use of the spread operator Ω defined as:

$$\Omega = \sum_n [\langle w_{n0} | \mathbf{r}^2 | w_{n0} \rangle - \langle w_{n0} | \mathbf{r} | w_{n0} \rangle^2] \tag{2.54}$$

This formulation of the localization functional allows a natural decomposition into two functionals:

$$\Omega = \Omega_I + \tilde{\Omega} \tag{2.55}$$

Where,

$$\Omega_I = \sum_n [\langle w_{n0} | \mathbf{r}^2 | w_{n0} \rangle - \sum_{m\mathbf{R}} \langle w_{m\mathbf{R}} | \mathbf{r} | w_{n0} \rangle^2] \tag{2.56}$$

and

$$\tilde{\Omega} = \sum_n \sum_{m\mathbf{R} \neq n0} \langle w_{m\mathbf{R}} | \mathbf{r} | w_{n0} \rangle^2 . \tag{2.57}$$

It can be demonstrated that Ω_I is invariant under any unitary translation, while this it is not the case of $\tilde{\Omega}$. Thus, the problem is reduced to find the minimum of $\tilde{\Omega}$.

In a simulation cell with a lateral size L_x, a Wannier function center (WFC) can be defined as the center of the distribution of its corresponding WF. This is explicitly given by [99]:

$$x_{nk} = -\frac{L_x}{2\pi} \Im [ln \langle w_{nk} | e^{-\frac{i2\pi x}{L_x}} | w_{nk} \rangle] \tag{2.58}$$

with analogous expression for the y and z components. The WFC, along with the spread of the WF, are a useful tool to reduce the complex information contained in a wavefunction as the WF to just four numbers, the coordinates of the WFC and the associated spread. I did extensive use of this tool to analyze the details of the electronic structure of the systems targeted in the doctoral project and these will be recalled and detailed in the next chapters whenever needed to support the discussion.

2.4.4 The Lattice dynamics method

Infrared (IR) and Raman spectrum result from vibrational modes of the system. Nonetheless, I wish to bring to the attention that a vibrational spectrum does not always correspond to an IR or a Raman one. This is a detail that sometimes is not pointed out in the literature, as I could verify in the course of my work, but that deserves attention. To have an IR or a Raman response, a displacement of both the nuclei and the electrons is required, but it must occur with a displacement of the center of charge of the positive (nuclei) part and the negative (electrons) part to give rise to a non-zero dipole that, in turn, contributes to the IR/Raman signal. For instance, a biatomic molecule (H_2, O_2, etc.) have a well defined stretching mode, hence a vibrational peak, but due to the symmetry of the molecule, no positive/negative center of charge displacement occurs, thus these molecules are IR silent. To make the scenario more complicated, but those two spectroscopic methods have inactive modes, despite being both vibrational techniques to probe a system. Namely, an IR spectrum shows modes that are not visible in Raman spectroscopy, and the reciprocal is true. Conversely, some modes are visible in both method, and, finally, some are inactive in both. Thus, both IR and Raman spectroscopy provide incomplete information and present difficulties in mode assignment to structural phenomena.

Methods based on lattice dynamics [100] have been proposed over the years to determine all the vibrational modes of a given system, often resorting to the hypothesis of local harmonicity. To giev a brief overview of the basis of these approaches, we can start by

writing the potential energy $V(\mathbf{r})$ in a Taylor series with respect to a small displacement of the particles at the position $\mathbf{r}$. This Taylor expansion gives:

$$V = V_0 + \frac{\partial V}{\partial \mathbf{r}}\mathbf{r} + \frac{1}{2!}\frac{\partial^2 V}{\partial \mathbf{r}^2}\mathbf{r}^2 + ... \tag{2.59}$$

At equilibrium, meaning at the minimum of this parabolic-like function, the forces are all zero, so the second term (same as eq. 2.31) vanishes. Third and higher-order terms are generally neglected, and we drop the first constant term which is irrelevant and does not contain any physics interesting in this context. Thus, we construct the V_{ij} matrix form the second derivative of the potential:

$$V_{ij} = \frac{\partial^2 V}{\partial \mathbf{r}_i \partial \mathbf{r}_j} \tag{2.60}$$

which is called the force constant matrix. The potential energy is then reduced to a matrix whose elements are the ones written above:

$$V = \frac{1}{2}\sum_{i,j} \mathbf{r}_i V_{ij} \mathbf{r}_j \tag{2.61}$$

This expression indicates that $V_{ij}\mathbf{r}_j$ is the force acting on the atom i if the atom j is displaced by $\mathbf{r}_j$. Within the AIMD framework used in my work, those forces are calculated using the finite differences method, and for each displacement the electronic structure is consistently recomputed, thus remaining in an *ab initio* scheme. Hence, the algorithm considers a system of N ions at sites i and j and the index of the three cartesian coordinates $\alpha = x, y, z$ is the one for the degrees of freedom of those ions. When we displace one ion j of the system by a distance $\pm r_\alpha$ in the α direction, total energy and forces are recomputed for every ion i of the system. While forces are computed analytically, as in any DFT implementation, the derivative of the force is computed numerically by finite difference as:

$$-\frac{\partial^2 V}{\partial \mathbf{r}_i \partial \mathbf{r}_j} = \frac{\partial F_{ij}}{\partial \mathbf{r}_j} \approx \frac{F_{ij}^{+} - F_{ij}^{-}}{2r_\alpha} \tag{2.62}$$

where $F^{\pm}$ is the force corresponding to a displacement of $\pm r_\alpha$. Consequently, the EOM for a particular atom i becomes:

$$m_i \frac{d^2 r_i}{d^2 t} = -\sum_j V_{ij}\mathbf{r}_j \tag{2.63}$$

where m_i is the mass of the i-th atom. The solution of this equation has the form:

$$r_i^{\pm} = \frac{1}{\sqrt{N m_i}}\mathbf{e}_i exp[i(\mathbf{q}\mathbf{r}_i - \omega_i t)] \tag{2.64}$$

where $\mathbf{q}$ is the wavevector and $\mathbf{e}_i$ is the polarization vector of the $i-$th ion. If eq. 2.64 is inserted into eq. 2.63 we get the eigenvalues equation:

$$\omega_{i,\alpha}^2 \mathbf{e}_i = D_{i,j}\mathbf{e}_i \tag{2.65}$$

being $D_{i,j}$ is the dynamical matrix, which is a Fourier transform of V_{ij}, and $\omega_{i,\alpha}$ are all the vibrational modes (normal modes) of the system. $D_{i,j}$ is a $3N \times 3N$ matrix, thus it has $3N$ vibrational modes or, more precisely, $3N - 6$ modes, since three translations and three rotations of the whole system (spurious modes) are part of of the computed spectrum and are generally identified by imaginary modes. This method can predict Raman and IR spectrum within the hypothesis that atomic displacements correspond

to dipolar displacements, since all vibrational modes are accounted for. The incomplete information of the IR and Raman spectroscopy comes from the impossibility to describe the atoms or group of atoms responsible of a specific vibrational mode. Here, however, since the eigenvectors of the dynamical matrix are the polarization vectors of the system for each normal mode (eigenvalue) computed, each vibrational mode is clearly linked to specific atom/atoms displacement, thus making easy to identify the atoms or the ensemble of atoms responsible for a given vibrational mode.

Chapter 3

Structural, electronic and dielectric properties of carbon nanotubes interacting with Co nanoclusters

Summary
The fluctuation dissipation method has been used as the reference approach to extract from my dynamical simulations the IR and MW spectra. In this chapter, first principles dynamical simulations, and specifically the CPMD method, have been used and tested to probe their capability in providing the desired information and to understand their limitations. The use of these simulation methods in this direction and in this field of applications represent a novelty (and a challenge) of this thesis project. The specific system on which these methods have been applied represents a new frontier in tuning the electromagnetic response of carbon-based materials, particularly carbon nanotubes (CNTs). Namely, the response of CNTs can be changes or modulated by the addition of metallic clusters or nanoparticles at their external surface. This has the advantage of being realizable without particular difficulty, as opposed to CNTs encapsulating heteroatoms or molecules. In the application of interest to my project, I tested the case of Cobalt aggregates decorating the external surface of a CNT. Thus, in the following paragraphs, I provide a microscopic picture of the interaction at finite temperature between a CNT and a variable number of Co aggregates mimicking the plausible experimental coverage. The dynamical simulations allow to observe structural deformations and conformational evolution of the composite systems. This, in turn, affects the electronic structure evolution and the related dielectric response. A rationalization of the microscopic phenomena involved is done by resorting to the maximally localized Wannier functions (MLFWs) and centers (WFCs) introduced in the methodological chapter. For direct comparison with experiments, the IR spectrum and the complex dielectric function are computed for each system considered. Finally, a discussion on those results in the perspective of possible achievement and limits of the approach will be done. The work presented in this chapter and all the results reported have been finalized in a publication appeared in Carbon Trends (HAL Id: hal-04742694, DOI: 10.1016/j.cartre.2024.100410) in 2024.

3.1 Motivations, systems studied and methods

Since their discovery more than twenty years ago[26], CNTs in direct interaction with metallic atoms and nanoparticles have attracted a considerable interest and a still expanding range of applications mainly targeted toward next-generation electronic devices and systems[44]. Their acknowledged efficiency in terms of electronic and thermal transport, the relatively low production cost, and the controllable, to a certain extent, environmental impact are counterbalanced by the still existing technological difficulty in growing a specific nanotube in situ and in controlling its chirality[33]. On the other hand, the physical properties of a bare CNT can be tuned by adding heteroatoms or clusters at the extenral surface of a CNT and in particular metallic adducts[42]. The synergy of CNT and metal clusters decorating their surface can lead to new optical, electronic or magnetic properties depending to the chemical nature of these additional external objects[46]. In the microwave domain, Sui and coworkers [47] have shown that Co atoms deposited on CNTs allow to modulate the frequency response of composite polymer/CNT systems, resulting in a shift of the absorption peak.

Yet, despite intensive experimental activity, especially in the last ten years, a detailed atomic-level knowledge of the mechanisms regulating the interaction of heteroatoms and clusters with CNTs is still lacking. This is indeed a major stumbling bock, because this fundamental knowledge is instrumental to design and tune the resulting macroscopic properties, and in particular the dielectric response of these composite materials. Starting from this rich background, in this work I made intensive use of the simulations tools and methods reported in my second chapter to investigate the behavior at finite temperature of single-walled CNTs (SWCNT) decorated with a variable number of Co clusters mimicking the experimental coverage. Such a cooperation of Co aggregates and SWCNTs determines the sought macroscopic properties of these promising systems. The choice of coated CNTs, as opposed to CNTs encapsulating metallic atoms or clusters, as mentioned in the introduction of my thesis, is due to the fact that the production of these composite systems is less demanding than a growth of CNT around Co clusters or nanoclusters and the amount of metallic atoms coating the CNT can be better controlled, with clear advantages in term of feasibility, production costs and overall weight of the obtained material. All these features make this class of systems particularly appealing for electronic and aeronautics applications, where too heavy materials risk to damage devices, and weight cut or limitations are required to boost flight efficiency of aircrafts.

3.2 Models realized and methods

3.2.1 model details

As a reference system, we considered a carbon nanotube of chirality (10,10) as a prototype of armchair system possessing known conductivity properties, being stable over a rather wide range of temperature and currently used for chemisorption experiments [101–103].

The simulated segment of this (10,10) CNT contains 240 C atoms, has a diameter of 13.50

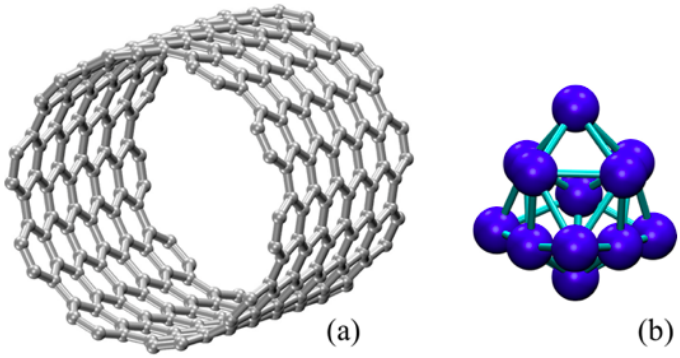

Figure 3.1. Simulated systems of (a) the (10,10) carbon nanotube and (b) the Co nanocluster composed of 12 atoms equilibrated as described in the text. The color code here and in the following figures is gray for C and blue for Co.

Å and a length of 14.77 Å. This system is simulated inside an orthorombic cell $a \times b \times c = 34.40 \times 34.40 \times 14.77$ Å^3 for an isolated CNT on which periodic boundary conditions are applied. With this choice, the CNT is periodically repeated along the c axis whereas along the other two axes the large empty space ensures a good separation from repeated images and a space sufficient to accommodate the Co clusters detailed in the ongoing discussion. Concerning the Co nanoclusters, due to the poor literature available on structural data of these nanoobjects, we constructed a minimal nanoparticle composed of 12 Co atoms compatible with published data [104]. Small cobalt clusters are useful model systems for investigating size-dependent magnetic properties of transition metals. Although the available literature specifically addressing Co_{12} clusters is relatively limited, clusters in this size range have been identified as exhibiting well-defined local magnetic moments and finite-size effects, making these atomic agglomerations important reference systems for nanoscale magnetism [105]. In this context, Co_{12} represents a physically meaningful cluster size able to capture essential magnetic features while remaining computationally tractable. Plus, in a recent study, an aromatic benzene ring [106] has been shown to be suitable to stabilize the Co structure. Since the same hexagonal motif is what we have on a CNT, this has been used as a guideline to select Co nanoclusters to interact with the external surface of our CNTs. The simulation cell for this nanopaticle was a $18.0 \times 18.0 \times 18.0$ Å^3 cubic box and the cluster was considered as an isolated system.

From those two reference systems, upon thermal equilibration, two composite systems have been created. These two systems are composed of the the (10,10) CNT on which, in the external surface, three and four Co nanoclusters were added. These numbers are not randomly chosen, but correspond to a coverage of $\sim$ 15 % and $\sim$ 20 %, respectively, consistently with the experimental indications. In the first case, for the total coverage of three Co nanoclusters, the aggregates were placed at different positions on the external surface of the CNT, carefully avoiding any possible direct interaction among them. This was essential to investigate the way these nanoclusters interact with the CNT and to allow enough separation among the Co aggregates to allow them to equilibrate independently on the CNT substrate. One nanoparticle was initially placed at the center of the aromatic cycle of the hexagonal motif of the nanotube, a second one was positioned on top of a C-C bond, and the third one on a C atom at the vertex of one of the hexagons of the CNT. This covers all the possibilities suggested in the literature as potentially stable sites for approaching atoms or molecules. Then, to investigate the effect of coverage on this

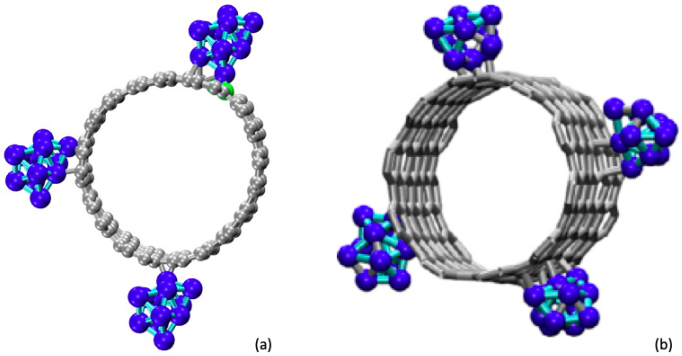

Figure 3.2. Simulated systems of (a) the (10,10) carbon nanotube decorated with three Co nanoclusters and (b) the (10,10) carbon nanotube decorated with four Co nanoclusters.

same system, a second system was prepared in a similar way, but a fourth Co nanocluster was added, again at a distance sufficiently large to avoid any bias or forced interaction with the three Co nanoclusters already present. These systems are simulated in box $a \times b \times c = 42.33 \times 42.33 \times 14.77$ Å^3, with periodicity along the c axis is still mimicking an infinite system, while the two other dimensions are large enough to ensures the isolation of the system from its periodically repeated replicas.

3.2.2 Methods

As explained section 2.3, among the two possible implementations of a first principles molecular dynamics, BOMD and CPMD, we selected the CPMD approach, since conservation of constants of motions is easier than BOMD, which requires a high degree of convergence of the recomputed electronic structure at each step to achieve an acceptable numerical conservation of the total energy and an accurate calculation of the forces. In fact, errors in the estimation of the proper ground state in a BOMD approach accumulate along the trajectory and can become a serious problem for long lasting simulations as the one required in my project. The mathematical formalism of the CPMD algorithm, instead, grant such a conservation because of its construction. Thus, all the simulations conducted here have been done within the CPMD [84] framework, being DFT [58] the *driver* of this specific dynamical propagation of electronic and ionic degrees of freedom.

Simulation Protocol

In order to have some check point, to survey the behavior of a simulated system and to verify if the simulation was correct from a phyiscal-chemical standpoint, we set up and benchmarked a precise simulation protocol summarized as follows. First, the system is created according to the guidelines given above, resulting in a set of atomic positions based on standard bond lengths and angles provided in the literature and available databases. Then the wavefunctions and electronic density are computed by numerical optimization as in any standard DFT scheme, described in section 2.2. Specifically, we considered an electronic structure as *converged* when the total energy reaches an accuracy of 10^{-6} a. u. (Hartree) and gradients on the electronic degrees of freedom are lower than 10^{-5} a. u. At this point a full relaxation of the structure is done by using a damped dynamics approach in order to find the ground state of the system. To this aim, a friction force is applied to atoms velocities and the system is annealed up to a temperature around 0.1 K. This step helps the system to find a local minimum of the potential energy surface (PES) before moving to the dynamic stage. The following step consists in a dynamics in the NVE microcanonical ensemble to check for the stability of the system and to explore locally the PES for possible equivalent configurations with energies comparable to the

minimum found. Since, the evolution of the system in the NVE ensemble is characterized

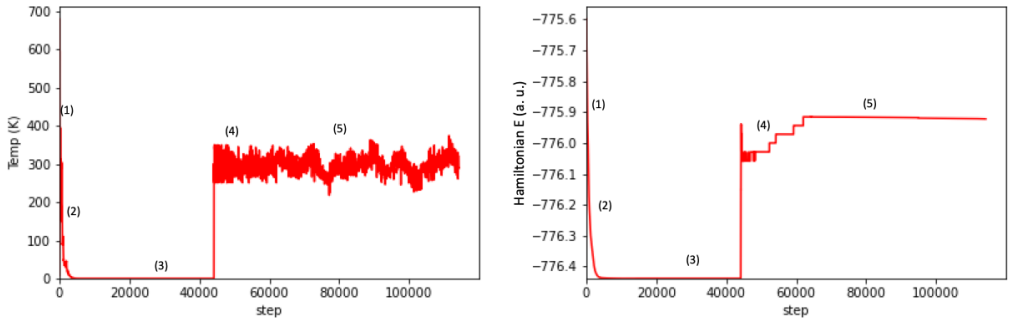

Figure 3.3. key parameters to follow the evolution of a simulated system, at the left it is the temperature of the system and at the right it is the Hamiltonian energy of the system. The five phases are clearly exposed here. (1) the system wavefunctions are initialized, (2) the wavefunction are annealed, then (3) the minimum energy is probed in a NVE dynamic, after (4) a rescaling, (5) the NVT dynamic is started using a Nosé-Hoover thermostat.

by a constant energy, thus, if a lower energy configuration is reached, the kinetic energy increases, balancing the lowering of the DFT potential energy, and this energy difference can even distribute among the nuclear and electronic degrees of freedom in a CPMD scheme, thus allowing for a surveillance *on the fly* of the detailed behavior of the system. Once the stability is assessed in the NVE ensemble, we started the heating phase to bring the system in an NVT ensemble. This is achieved in two stages: (i) initially a simple velocity rescaling algorithm is used to bring the system to a finite temperature (room temperature in the cases studied), then (ii) when the systems starts keeping the target temperature imposed, visible as a gradual disappearing of the rescaling jumps in the temperature and the total energy, we switch to a Nosé-Hoover thermostat chain for a proper evolution in the canonical NVT ensemble. In this last stage, statistics is accumulated and physical values extracted.

Parameters and preparation

In all my simulations a fictitious electron mass of 380 a. u. and an integration step of 4 a. u. (0.097 fs) ensured good numerical control of the constants of motion. This is illustrated in Fig. 3.4, where a clear separation between the (fictitious) electronic and (real) ionic kinetic energies indicate that the two sets of degrees of freedom do not exchange energy and that the adiabaticity is preserved. For the exchange and correlation interaction, we selected the Becke exchange and the Lee–Yang–Parr correlation functionals (BLYP), a choice that has already been benchmarked and used for simulating stand-alone CNTs and CNTs interacting with atoms and molecules [107]. The BLYP functional was complemented by the inclusion of van der Waals interactions according to the maximally localized Wannier functions [108] implementation [109, 110]. The core-valence interaction was described by a norm-conserving numerical pseudopotential of the Troullier–Martins type for C and a semi-core one of the Goedecker–Teter–Hutter type for Co. Electronic wavefunctions are expanded on a PW basis set with a cutoff of 100 Ry (1360.57 eV) and all calculations have been done in a spin-unrestricted approach, with the sampling of the Brillouin zone of the reciprocal space limited to the Γ point. Such a relatively large cutoff value is needed for an accurate description of the semi-core states included in the Cp pseudopotential and resulted essential for a good description of the overall electronic structure. Indeed, according to our experience, for a small cutoff value of the PW basis, beside a poor description of the semicore states, a good control of the adiabaticity is compromised for long-lasting dynamical simulations. Moreover, serious convergence problems arise in the calculation of the MLWF and, hence, in the estimation

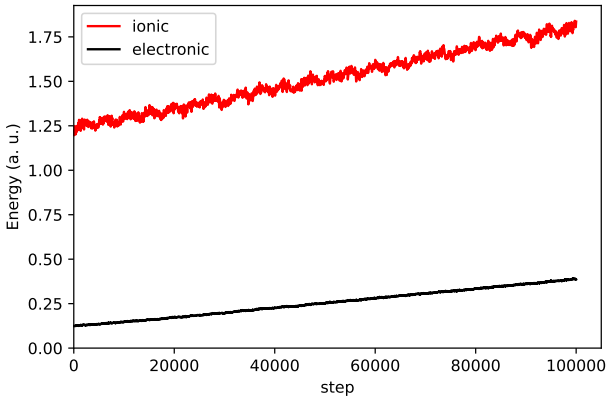

Figure 3.4. Kinetic energies of the ionic subsystem (red curve) and the fictitious electronic subsystem (black curve) for the CNT at 300 K and comprising 240 C atoms, showing a clear energetic separation of the two subsystems

of the vdW interaction. Gradient corrections (GC) are also affected by the choice of the cut-off, so special care must be paid in this (and not only) type of simulations. Concerning this aspect, in all my calculations I verified that a GC-cutoff value of 10^{-6} a. u. is a wise choice to avoid numerical noise and having a stable simulation. Simulations were performed with the CPMD package. For convenience, we speak about IR-spectrum even if the lower-frequency part (10 - 300 cm^{-1}, representing about 10 % of the whole spectrum) corresponds to the THz range.

As far as the preparation of the Co cluster is concerned, I started with an optimization of the isolated Co aggregate at the DFT level used for all systems and the NVE equilibration phase lasted for about 15 ps. This was followed by a canonical NVT dynamics at 300 K lasting for 45 ps where data were extracted for post-processing. The equilibrated structure, shown in Fig. 3.1 (b), assumes a conformation compatible with the hexagonal closed-packed bulk Co [111] with bond lengths (2.25-2.29 Å) and angles ($\sim 60°$) of the triangular facets typical of this type of symmetry. As mentioned above, a spin-unrestricted description was adopted to check for possible spin-related issues (magnetic moment) of the Co nanocluster, evidencing an overall symmetric distribution of spin-up and spin-down distributions conferring a zero total spin to this type of Co nanocluster.

3.3 Results and discussion

For these systems the performed canonical NVT simulations lasted for 50 ps and the last 30 ps, where the system is well equilibrated, were used to accumulate statistics, observe structural deformations, characterize the electronic structure, and extract the IR absorption spectra to get the physical information that can be observed macroscopically.

3.3.1 Structure and chemical bonding properties

One of the interesting aspects disclosed by the use of molecular dynamics is that it grants access to atomic-level information otherwise not accessible to experimental probes, thus allowing for the search of the microscopic origin of the behavior of a system ultimately resulting in a global response detectable at a macroscopic level. By looking at the atomistic mechanisms occurring during the canonical NVT dynamics on CNT/Co systems, we noticed two main features. The first one is that the Co clusters form chemical bonds with C atoms at the surface of the CNT, hence being chemisorbed, with bond lengths of 2.00–2.15

Å. The structural influence of this chemisorption can be observed through the interatomic distances in the neighborhood of the Co-C bonds, resulting in slight elongations and distortion of the local carbon network structure as quantified in Fig. 3.5. Concerning the Co nanoclusters, the mean interatomic distance of an isolated Co nanocluster calculated during the preparation phase is 2.282 ± 0.008 Å, while the mean interatomic distance of a nanocluster in interaction with a CNT increases to 2.308 ± 0.011 Åas shown Fig. 3.5 (a). From the CNT standpoint, a direct structural effect is also observed in the sense

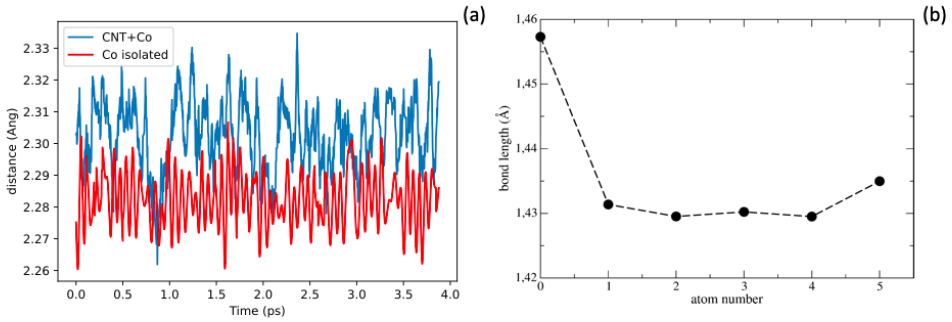

Figure 3.5. (a) Co-Co Bond length inside the Co nanocluster averaged over a 4 ps simulation time, in red when the Co nanocluster is simulated as a stand-alone system, in blue for the Co that decorates the CNT (b) C-C Bond length of the nanotube at increasing distances from the C site "0" where a C-Co chemical bond has been formed. The bond distortion propagates up to the fourth neighbor before assuming, from the fifth neighbor, typical values of a regular CNT. The black circles indicate the atom neighbor at increasing distances whereas the dashed line is only a guide to the eye.

reported in panel (b) of Fig. 3.5. Namely, in the vicinity of the C–Co chemical bond, the first C–C distance turns out to be longer, whereas the next ones up to the fourth neighbor shrink. This has then the effect of slowing down locally all the vibrational modes of the C atoms directly bound to these metallic nanoclusters. And, as a consequence, the IR and dielectric response shift toward lower frequencies, although it is difficult to quantify this shift at this stage. This will be better discussed later in the ongoing chapter. The effect of this chemisorption on the CNT/Co system can be quantified using the formula :

$$E_d = E(CNT + nCo^{12}) - E(CNT) - nE(Co^{12}) \tag{3.1}$$

where $E(CNT + nCo^{12})$ is the energy of the structure consisting of a CNT which has chemisorbed n nanoclusters of Co, $E(CNT)$ is the energy of the pristine CNT, and $E(Co^{12})$ is the energy of a single Co nanocluster. From this simple formula, for instance, we can estimate the energy difference for the system carrying four Co nanoculters, resulting to be $E_d = -22.04 \pm 0.02$ u.a., indicating that a chemisorption has been realized and this energy difference corresponds to the C–Co binding, but it accounts also for the variation of the C–C bonds in the vicinity of the C–Co chemical bond(s), plus the changes in the Co-Co bonds inside the nanoclusters.

A second effect is that at finite temperature (300 K in our case) these Co clusters are mobile and diffuse along the CNT by breaking and reforming these chemical bonds rather quickly with an average speed of 0.82 ± 0.09 Å/ps corresponding to a diffusion coefficient of $5.8 \pm 0.2 \times 10^{-4}$ cm^2/s as illustrated in panel (a) of Fig. 3.6 for the CNT decorated with three Co nanoclusters.

This displacement is accompanied by fluctuations of the shape of the Co nanoclusters which do not undergo any Co–Co bond cleavage, thus keeping their size. By looking at the

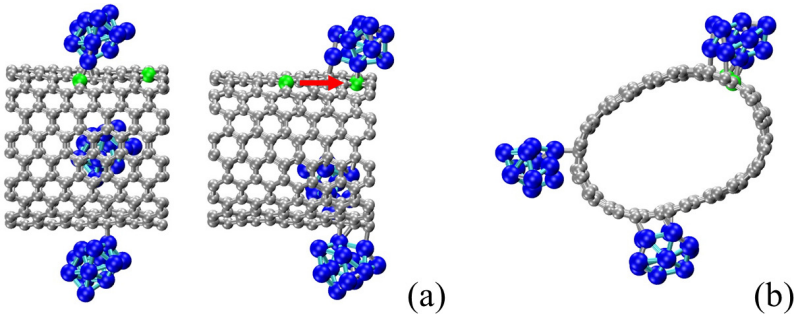

Figure 3.6. Evolution of the (10,10) CNT decorated with three Co nanoclusters. (a) displacement of the Co nanoclusters during the NVT dynamics. The C atoms highlighted in green show the initial position of one of the three clusters (left) where a C–Co chemical bond exists and (right) displaced position assumed by this same Co nanocluster after 8.7 ps along the direction indicated by the arrow, where a new C–Co chemical bond has been created with the C site shown in green. Panel (b) shows a representative snapshot of the radial distortions occurring to the CNT as a consequence of the presence of Co nanoclusters bound to the external surface and diffusing on it. Apart from the C atoms evidenced in green, the same color code of former figures is used.

cross section of the CNT shown in Fig. 3.6 (b), we remark that the heavy Co clusters induce large deformations on a relatively long time scale (about 4-5 ps) of the nanotube during the dynamics. A general conclusion that can be drawn is that above a certain coverage,

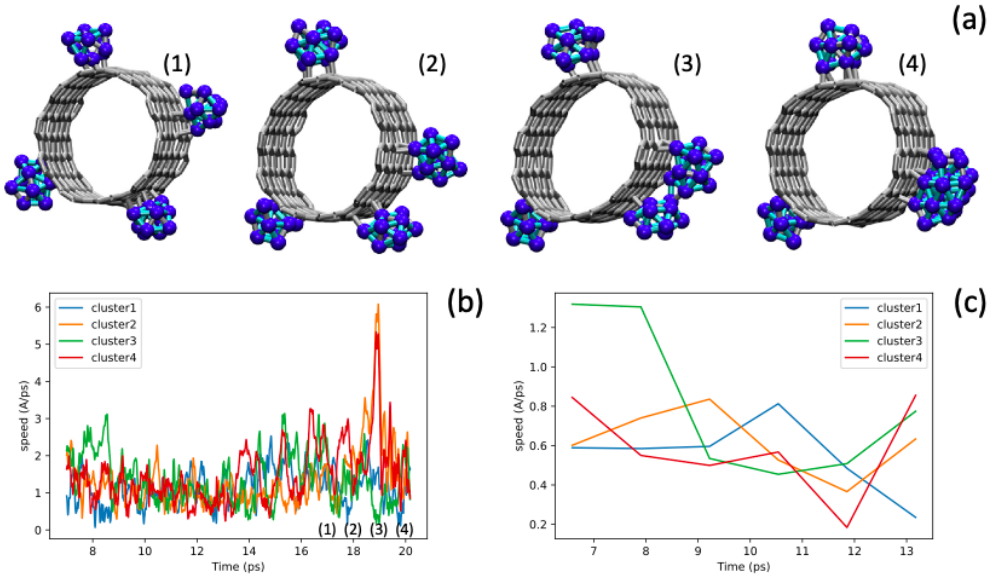

Figure 3.7. (a) Panels from letf to right show the dynamical evolution of the four Co nanoclusters on the (10,10) CNT during our canonical NVT simulation resulting in the formation of larger Co cluster which remains stable on the time scale of our FPMD. The color code is the same used in former figures. (b) instantaneous velocity of the four Co clusters, showing that the formation of the larger cluster does not result from an entirely random process but seems to be well structured and a consequence of the increased coverage. (c) Velocity averaged over a picosecond for each cluster before the formation the larger cluster.

corresponding to the case of four Co aggregates in the case studied here, the inherent diffusion of these Co nanoclusters due to the finite temperature, gives rise to a coalescence of the isolated Co clusters moving on the external surface of the CNT. This induces the formation of larger aggregates or nanoparticles that can be difficult to control and that, once formed, remain rather stable on the composite system, as illustrated in Fig. 3.7. In about 20 ps, during our NVT dynamics, this clusterization process occurred for two of

the four Co nanoclusters which meet each other. Looking a at the nanoclusters speed reported in Fig. 3.7 (b), the Co aggregates follow a random diffusion process characterized by high speed during this random movement. Nonetheless, by looking at the average movement over a picosecond reported in Fig. 3.7 (c), the average velocity is 0.64 ± 0.1Å/ps, which is a consistent and common feature among the three Co clusters. The increased coverage simply gives more opportunities to small clusters to meet over the ps time scale of the simulation, thus increasing the probability of coalescence. The clusterisation process proceeds with a sudden change of speed of the clusters labeled as 2 and 4 in Fig. 3.7 (c). A practical consequence of the newly formed Co nanoparticle having a size double with respect to the original twelve-atom nanocluster is a slower diffusion of this more massive object on the surface of the CNT. Yet, this alone is insufficient to hinder completely the diffusion process, which is still an active dynamical feature irrespective of the size of the Co aggregate.

While structural and dynamical features due to the presence of the Co nanocluster on the CNT can be easily characterized and quantified in my simulations, the interpretation of the appearance of structural deformations observed in the CNT in interaction with Co clusters are more difficult and the consequence on the dielectric (or magnetic) response escapes quantification and rationalization at this purely mechanical analysis. The next question is, then, how can we explain thus structural deformations? To answer this question, a deeper analysis accounting for the underlying electronic structure is required. This is the target of the next paragraph.

3.3.2 Electronic structure and spin density properties

The electronic structure of a system studied within the DFT framework can be easily described in terms of the Kohn-Sham electronic density and related orbitals, intended as the eigenfunctions of the KS Hamiltonian. Yet, on one hand, these is no guarantee that these orbitals represent actual molecular orbitals; generally they do, but just to a certain extent an there is no guarantee that they are good representations of actual molecular orbitals. Due to the nature not necessarily localized of the KS wavefunctions, some characteristics and behaviors might result hard to catch in a simple KS description. Moreover, it always somehow arbitrary to partition the electronic density in a way to extract meaningful local information. Thus, to get a better bond descriptor, I shall use the MLWF introduced in section 2.4.2, where the unitary transformation into localized Wannier function, Wannier functions centers (WFCs) and their spread allow to recover a sort molecular-orbital picture of the local electronic structure. This method provides a practical way to follow the

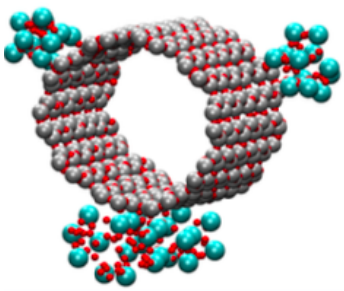

Figure 3.8. Simulation of a CNT with a coverage of four Co nanoclusters. From the MLWF calculation, the WFCs (highlighted as small red spheres) of valence electrons can be visualized and monitored as classical-like objects evolving with the atoms during the dynamics.

electrons in the structure with a minimal information consisting on the WFCs cartesian coordinates, accompanied by their spread, which in a sense resemble a sort of classic picture

of electrons (as opposed to an extended and complex object as would be a wavefunction), as shown Fig. 3.8. It has been already shown [112] that the use of MLWF and WFCs allows for a direct inspection of chemical bonding and provide a useful bod descriptor to understand the nature of a chemical bond, to compute local dipole moments and to extract both local and global dielectric properties, especially in low symmetry cases. In my work, I make extensive use of this mathematical tool to characterize the Co-decorated CNTs and to provide a detailed microscopic picture of this composite system.

In order to explain the structural deformations discussed in the previous section, along with the effects of the chemisorption affecting C–C chemical bonds around the Co–C area, I attempted to focus on different segments of the whole system in an attempt at unraveling the important features. Thus, I identified three distinct areas from the distances distribution reported in Fig. 3.5: the first one in the direct vicinity of the chemisorbed Co atoms where the bound length turns out to be increased, the second area starts from the second chemical bond and extends up to the fourth, where a shrink of the C–C bonds occurs, and, finally, the region far from the Co–C chemical bond is the one that remains unperturbed by the presence of the interacting Co nanocluster. To this aim, a comparison with the bare CNT has been done, to get a clearer picture of the regular dynamical shrink and elongation of the C–C chemical bonds not depending on the presence of Co–C bonds. In my first analysis, I inspected the relative positions of the WFCs (i. e. the chemical bonds) with respect to the bonded C atoms in these three distinct areas. The longitudinal and radial distributions are reported Fig. 3.9. These two specific directions along which my analysis has been done have been selected according to the symmetry of te CNT. Moreover, it is worthy to note that in this calculation only well localized and low delocalized electrons (minimal Wannier spread) are taken into account, whereas highly delocalized valence electrons extending over larger areas are supposed to be only marginally involved into tight bonds.

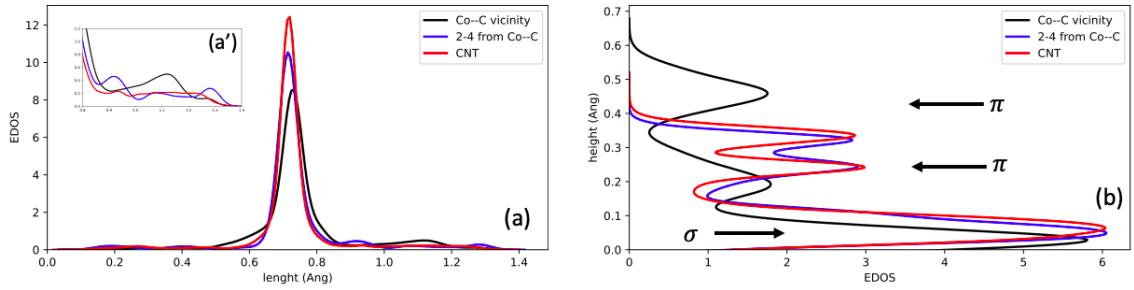

Figure 3.9. Distribution of the WFCs, accounted with their spread, resulting in a local electronic density of state (EDOS), Panel (a) shows the longitudinal distribution in the sense given in te text, namely along the external surface of the CNT where valence electrons are distributed on the chemical bonds of the nanotube carbon network, (a') is a zoom on the right side of the central peak, added for clarity. Panel (b) shows the distribution of the perpendicular part of the valence electrons contributing to this local DOS; we can easily identify the localized band (σ-bonds) and the delocalized π-band. The electronic density distribution highlighted in red shows the contribution of the unperturbed C–C bonds, analogous to the pristine "bare" CNT, and refers to C atoms from the Co–C chemical bonds. The blue line refers to the bonds which underwent the contraction reported in Fig. 3.5 and discussed in the text. Finally, in black I show the situation relevant to the chemical bonds in the close vicinity of the Co–C bond.

The analysis of the valence electrons distribution presented here shows that most of the electrons are localized at the center of the bonds, as expected for covalent C–C structures, with major differences arising in the cae of Co–C bonds. The small shift arising in the peak positions is due to the different bound length identifies and discussed in this paragraph. Beside the characteristic of the σ bond, which does not contain specific information

useful to rationalize structural deformations, namely sp^2 and sp^3 σ bonds types, the more interesting part is given by a delocalization affecting π states as shown in Fig. 3.9(b), compared to the bare CNT, and the area in which bonds present a shrink: the distribution is characterized by a higher spread in the longitudinal part and in the radial part, amounting to 0.5 Å and 0.25 Å. While there is no clear numerical evidence of an electron deficiency (2.56 ± 0.01 electrons per C–C bound) between the carbon atoms close to the bound Co and the non perturbed C–C bonds, we can remark, nonetheless, that a wider π-band is less effective than a tightly localized one. In this respect, in the intermediate region, the radial π-band is tighter than the the one of bare CNT, and this is also confirmed by the larger spread observed on the longitudinal part. This provided an electronic structure insight into the geometrical trend observed and reported in Fig. 3.5. In Fig. 3.9(a'), a longitudinal feature of the π-band corroborates the general scenario depicted; the distribution shows a deviation of π-electrons from the C atom directly linked to the Co: this is a signature of the chemisorption, namely some electrons involved in the Co-C bond realize a nearly sp^3 structure with a C atom extruding form the cylindric geometry of the CNT, although no bond cleavage, neither on the CNT not on the Co cluster occur.

An important physical quantity for the evaluation of the electromagnetic properties of the system is the dipolar moment. The C atoms of the CNT forming chemical bonds with Co that induce deformation up to the fourth neighbor, result in a displacement of both atoms and underlying electronic structure, giving rise to dipole moments that evolve in time, thus contributing to the dielectric response of the system. In this respect, the MLWF method represents a useful tool to compute local dipole moments and an analysis around the C atom directly bonded to the Co is what I did to characterize locally the composite system, obtaining the result summarized in Fig. 3.12. The analysis presented is focused on C atoms

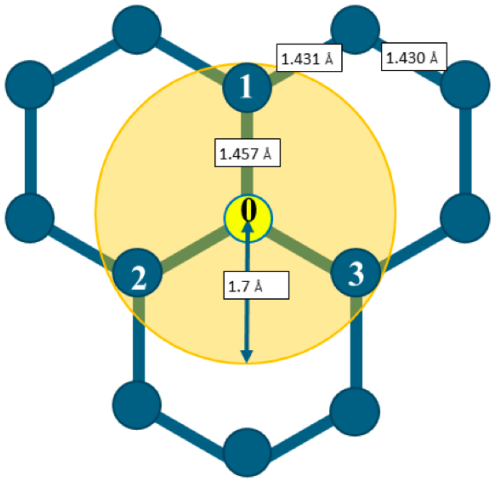

Figure 3.10. Detail of the local atomic arrangement and main bond distances in the neighborhood of the C atom directly bound to a Co atom of one of the decorating clusters. This chemically bonded atom, highlighted in yellow and labeled as "0", along with its nearest neighbors (labeled from 1 to 3) is the local pattern used to compute the local bond lengths and local dipole moment of the analysis shown in Figs. 3.5 and 3.11. The main average distances are indicated, and the yellow shaded circle of radius 1.7 Å indicates the atoms that have been taken into account for the calculation of the local dipole moment of Fig. 3.11.

directly involved in the C–Co bond and a comparison is done for an analogous C site on a pristine CNT not perturbed by Co atoms. We can see that the local dipole moment $|\mathbf{p}|$ distribution (Fig. 3.11), although broad due to the dynamical fluctuations during the simulation, is centered at 0.0 D for both the longitudinal and radial values of the local $|\mathbf{p}|$, whereas pronounced peaks between 3.5 and 12.3 D arise in the longitudinal distribution,

extending up to 15.7 D in the radial component. At the same time, for the bare CNT, a broad distribution is observed for the radial and the longitudinal part. The effects of the

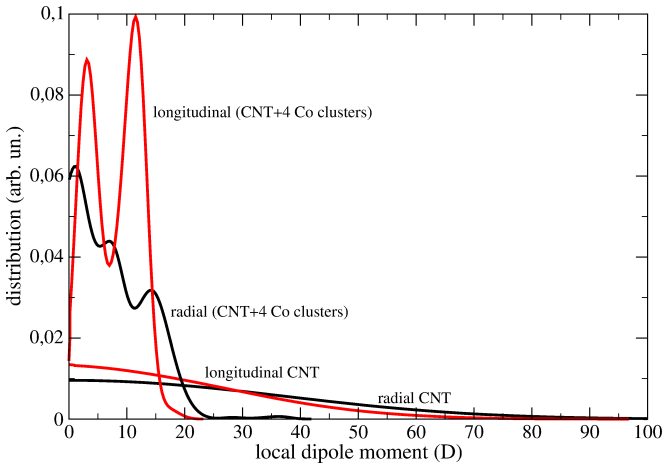

Figure 3.11. Radial (black lines) and longitudinal (red lines) local dipole moment distributions in a bare (10,10) CNT at 300 K and analogous distribution for the CNT decorated with four Co nanoclusters. The average value for a bare CNT is 0 D with a large broadening due to the dynamical deformations of the CNT. These deformations are less pronounced when a massive Co cluster is chemically bound to the CNT, but the local dipole moment is considerably enhanced as evidenced by the peaks at 3.5 and 12.3 D for the longitudinal component and 1.7, 7.3 and 15.7 D for the radial component.

chemisorption, in line with the geometrical and electronic analyses presented above, are evident also in the dipole moment distribution. Since some electrons are attracted by the Co nanoclusters, the local dipolar moment experiences a sort of constraint that, in turn, makes its distribution lower in comparison with the unconstrained one.

As discussed section 2.4.1, if the dielectric properties can be described in terms of dipolar moment and its time variations, the magnetic properties depend, instead, on the magnetic moment and its behavior as a function of time. To inspect also this aspect, we monitored the evolution of the spin density of the system along the dynamics, with special attention on the phases of the clusterization process. The final distribution is shown in Fig. 3.12 and the message we can extract is that the overall spin neutrality is kept all along the process, thus not giving rise to any undesired (or uncontrolled) magnetic moment. More precisely, locally the spin density $\rho_s(\mathbf{x}) = \rho_\uparrow(\mathbf{x}) - \rho_\downarrow(\mathbf{x})$ can undergo instant fluctuations, with spin-up and spin-down components localized on different regions, but the total spin $S = \int \rho_s(\mathbf{x}) d^3x$ is always zero. In view of the results obtained from the spin density analysis, we can safely conclude that $\rho_s(\mathbf{x})$ is not involved into the structural (and electronic) deformations discussed in section 3.3.1. Instead, the chemisorption resulting in the creation of Co–C bonds induces modifications in the electronic structure that have direct consequences on the macroscopic dielectric response. This will be the focus of the following paragraph.

3.3.3 Dielectric properties

In order to compute macroscopically observable properties of the system, we made use of the calculation *on the fly* of the total dipole moment of the system during the NVT dynamics. To this aim, after the initial equilibration of about 5 ps, the dynamical run

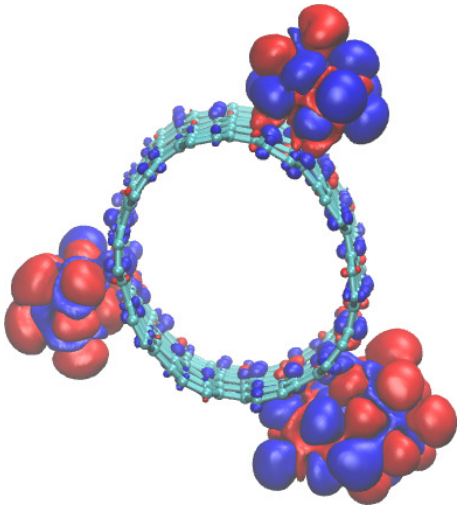

Figure 3.12. Spin density distribution of the CNT system carrying four Co nanoclusters after the clusterization process discussed in the text and shown in the former figure. The total spin of the whole system is equal to zero as well as the partial spin of each single Co nanocluster decorating the CNT. The isosurfaces are shown at a value of $\pm 1.00 \times 10^{-3}$ 1/Å^3 with the spin-up in red and the spin-down in blue.

was continued for 40 ps and, during this time, the total dipole moment $\mathbf{M}(t)$ was accumulated to extract the infra-red (IR) absorption spectrum with the method explained section 2.4.1; specifically, a Fourier transform of the dipole–dipole autocorrelation function $\langle \mathbf{M}(t+t')\mathbf{M}(t') \rangle$,

$$\alpha(\omega) = \frac{4\pi\omega \cdot \tanh(\beta\hbar\omega/2)}{3\hbar c V \cdot n(\omega)} \int_0^\infty e^{-i\omega t} \langle \mathbf{M}(t+t')\mathbf{M}(t') \rangle dt \tag{3.2}$$

where $\beta = 1/k_\mathrm{B}T$, being T the temperature at which the simulation has been conducted and k_B the Boltzmann's constant, V the volume of the simulation cell, $\hbar$ the reduced Planck's constant, c the speed of light and $n(\omega)$ the real part of the (complex) refractive index. The maximum entropy method, introduced in Section 2.4.2, was used to achieve a better resolution of the spectrum and to reduce numerical noise. This formula gives the product $\alpha(\omega) \cdot n(\omega)$, directly comparable to the IR spectrum measured experimentally and, as such, does not contain any quantity not directly available from our NVT simulations. The result of this analysis for the pristine (10,10) CNT is shown in panel (a) of Fig. 3.13. We notice that this spectrum agrees rather well with the experimental results reported for CNTs [113, 114]. More precisely, the peak at about 1590 cm^{-1}, attributed to the graphite-like G band and originating from diametral oscillations of the CNT due to the sp^2-hybridized C atoms orbitals [114], and the one around 880-900 cm^{-1} [113] more related to longitudinal oscillations along the nanotube axis are well reproduced by our simulations, although they have been shown to depend on the chirality of the CNT. Contrary to experiments, we do not have a CNT supported onto a solid substrate or embedded in a surrounding environment, thus the intrinsic flexibility of the isolated CNT at finite temperature confers some additional noise to the clean spectra detected experimentally. Yet, within the accuracy of our simulations, the quality of the IR spectrum ensures reliability to our approach.

A macroscopic effect induced by the presence of three Co nanoclusters is the fact that the overall amplitude of the spectrum increases of about a factor of two and becomes more noisy. The main peak of the G band around 1590 cm^{-1} spreads and turns out or be split into a number of roughly equivalent peaks covering the range between 1300 and 2000 cm^{-1}. Analogously, the sharp peak at 880-900 cm^{-1} broadens and becomes a sequence of nearly

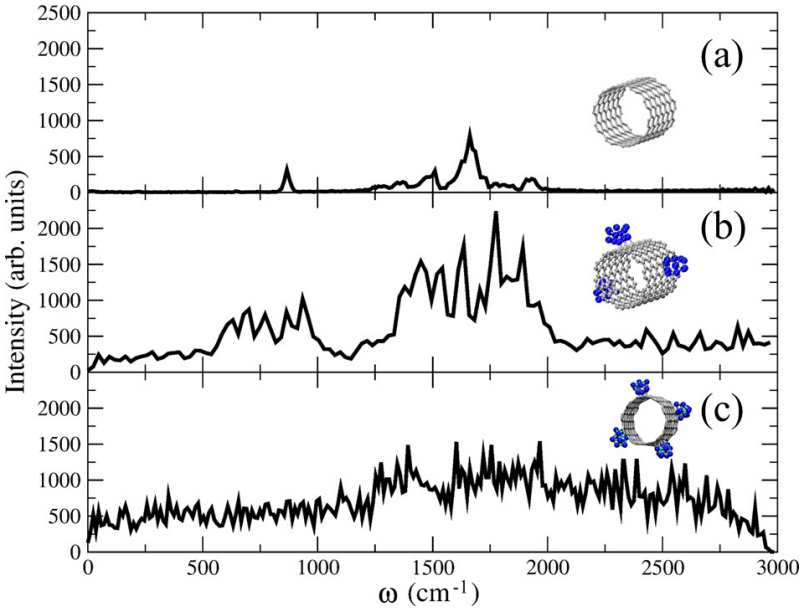

Figure 3.13. Simulated IR absorption spectra for (a) the (10,10) carbon nanotube, (b) the same nanotube decorated with three Co nanoclusters, and (c) decorated with four Co nanoclusters. The inset figures are a graphic reminder of the system to which each spectrum refers and the color code is gray for C and blue for Co.

equivalent peaks ranging from $\sim$ 700 to 900 cm^{-1}. It is worth noting the enhancement of the amplitude of the spectrum in the lower frequency range (THz range), indicating that the system starts having an electromagnetic activity also at $\omega < 300$ cm^{-1}. This effects is further enhanced when four Co nanoclusters are introduced, as seen in panel (c) of Fig. 3.13, resulting in a very noisy IR spectrum.

The increase of the noise on the spectrum and, at the same time, of the global amplitude of the IR signal shown in Fig. 3.6 (c) is the result of the addition of a fourth Co nanocluster to the (10,10) CNT. In the range 1300–2000 cm^{-1} we can barely recognize a set of dispersed peaks reminiscent of the G band of the pristine CNT, whereas the peak at 880–900 cm^{-1} is completely washed out by the dynamically interacting Co nanoclusters. This is accompanied by a more pronounced response in the region below 300 cm^{-1} (THz range).

Although we do not have neither sufficient statistics nor resolution to argue quantitatively about the very low frequency range, as shown Fig. 3.14, a peak in the range 20-50 cm^{-1} (THz range) seems to be a systematic feature in the three spectra of increasing amplitude depending on the number of Co nanoclusters. This feature will be reflected in the dielectric response discussed later. Despite being still far from the microwave regime, this trend offers a hint into the effect of adding the Co metallic clusters on the CNT: low frequencies becomes active as a consequence of the (heavy) constraint induced by the presence of Co aggregates and paves the route to a tuning in the desired regime. Yet, some warning have to be brought to the attention: overloading a CNT with Co nanoclusters has, on one hand, the effect of making the resulting composite heavier, not a desirable effect in aeronautics applications, and, on the other hand, due to the effective cost of Co, the production on an industrial scale can become unaffordable.

An analogous dynamical NVT simulation within the same spin-unrestricted approach was done for an isolated Co nanocluster. As mentioned in the methodological section, the total spin of twelve-atom cluster is equal to zero, indicating a non-magnetic state of our Co nanocluster. The IR absorption spectrum of this isolated Co nanocluster, shown in Fig. 3.15, was computed in the same way using the dipole accumulated along the last 45 ps

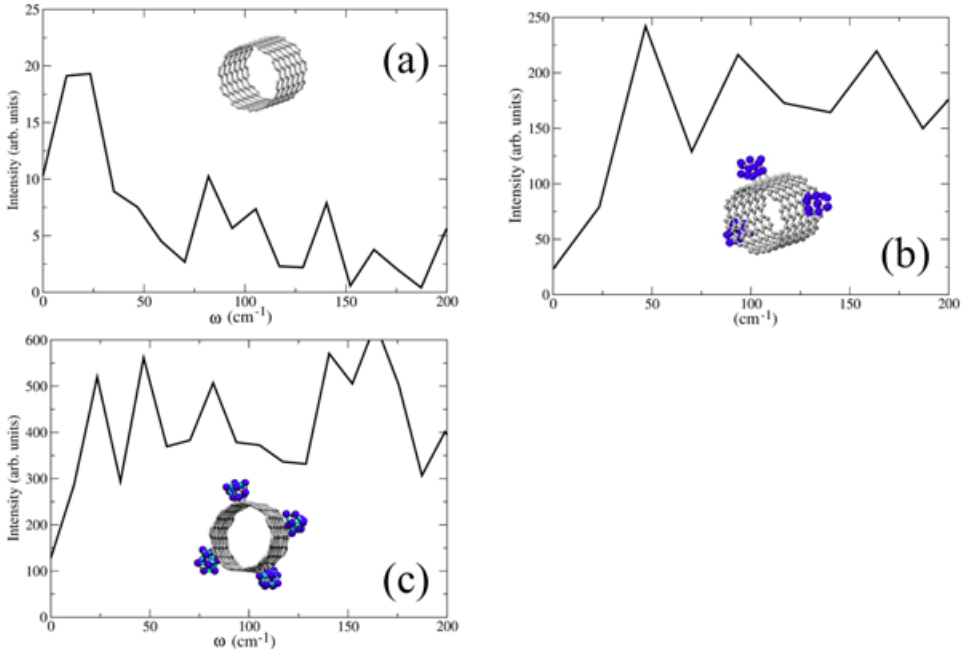

Figure 3.14. Details of the adsorption spectra in the low frequency range for the three systems discussed in the main text and sketched in the inset of each panel. Panel (a) is the bare (10,10) carbon nanotube (CNT), panel (b) the same CNT decorated with three Co nanoclusters and panel (c) the CNT carrying four Co nanoclusters. As indicated in the main text, the color code for the atoms is gray for C and blue for Co.

dynamics mentioned in the former paragraph. Although the comparison with experiments is difficult because of the fact that we have here a single isolated Co nanocluster, whereas in experiments nanoclusters of different sizes on a solid support are realized, the spectrum we obtain is still compatible with the experimental outcome [115] although very noisy due to the free motion of the twelve-atom Co cluster. Moreover, as it can be seen from Fig. 3.15, the intensity is roughly two orders of magnitude smaller than the spectrum of the bare CNT, consistent with the general idea of a weak dielectric response. The enhancement and

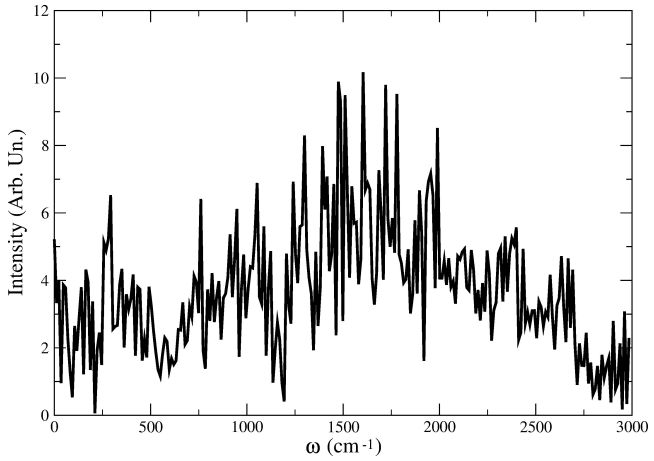

Figure 3.15. Simulated IR absorption spectra of the twelve-atoms Co nanocluster. The noisy signal is due to the large thermal motion of the isolated nanocluster

remarkable change in the IR spectrum upon addition of Co clusters can be rationalized in terms of local modifications of the structure and related dipole moment on the CNT. In the previous sections, I have shown that the presence of Co nanoclusters induces local deformations and modification in the underlying electronic structure of the C–C bonds of the CNT, thus modifying the rigidity of those C–C connections constituting the scaffold of a nanotube. The dynamical formation and cleavage of Co–C chemical bonds caused by the Co nanoclusters diffusion process is responsible for new additional modifications and relaxations, resulting in the large structural deformation observed and discussed above. Since relaxation processes are known to be responsible for the dielectric response, we could establish a direct link between structural and electronic modification and their effect on the absorption spectra. The Co clustering was an unexpected side product, nonetheless it gives us information on the behavior of the system when a certain coverage percentage is reached: since this newly formed Co nanocluster is bigger, its diffusion coefficient is lower that the small Co nanoclusters, but induces larger deformations in the CNT structure, thus contributing to a shift toward lower frequencies also of the G band with effects evident in the IR spectrum of Fig. 3.13.

For a more direct comparison with macroscopic physical quantities, which are of practical interest for the realization of these composite materials, we computed the complex dielectric function $\varepsilon(\omega) = \varepsilon_1(\omega) + i\varepsilon(\omega)$. The imaginary part is directly given by Eq. 3.2,

$$\varepsilon_2(\omega) = \frac{2c \cdot \alpha(\omega) \cdot n(\omega)}{\omega} \tag{3.3}$$

which holds for a non-magnetic medium. This is indeed the case here, since we can neglect any dynamical permeability induced by the Co clusters, due to their low amount and in view of the reported analysis of the spin density. Moreover, even if present, such a dynamically induced permeability is generally very low and restricted to a frequency domain below 10 GHz in the absence of applied magnetic fields and totally absent in the THz and IR range. The real part $\varepsilon_1(\omega)$ can be computed from the imaginary one via the Kramers-Kronig dispersion formula

$$\varepsilon_1(\omega) = 1 + \frac{2}{\pi} P \int_0^\infty \frac{\omega' \cdot \varepsilon_2(\omega')}{\omega'^2 - \omega^2} d\omega' \tag{3.4}$$

with obvious notations and following a well assessed protocol [116]. The results of these calculations for the three systems studied in this work are reported in Fig. 3.16, along with the comparative plot of the dielectric loss tangent defined as $\mathrm{tg}(\Delta) = \varepsilon_2(\omega)/\varepsilon_1(\omega)$.

The modifications over the whole frequency range, along with the amplification toward the low frequency interval below 300 cm^{-1}, reflect the discussion given above for the IR spectrum. The peak located between 20 and 50 cm^{-1} previously evidenced is further enhanced by the factor $1/\omega$ in Eq. 3.3, as shown in Fig. 3.17 . We reiterate that we are at the limit of what we can appreciate within the simulation time scale affordable with fisrt principles dynamical approaches. Nonetheless, this qualitative trend is worthy of mention, being a systematic feature rather than a simple random numerical fluctuation. In particular, the dielectric loss tangent is helpful in evidencing the fact that the response is amplified, along with the low frequency window in which this enhancement is present, as a consequence of the inclusion of Co nanoclusters in the system. This, however, has to be taken with some care because of the diffusivity of Co clusters and nanoclusters occurring already at 300 K and which is likely to be enhanced at higher temperatures. Another point worthy of note is the fact that beside the physical and chemical nature of the atoms decorating the CNT, which have their own absorption and dielectric properties, the fact that these relatively massive objects form chemical bonds with the C atoms of the CNT results in a slowing down of the collective modes of all the C atoms bound to the Co

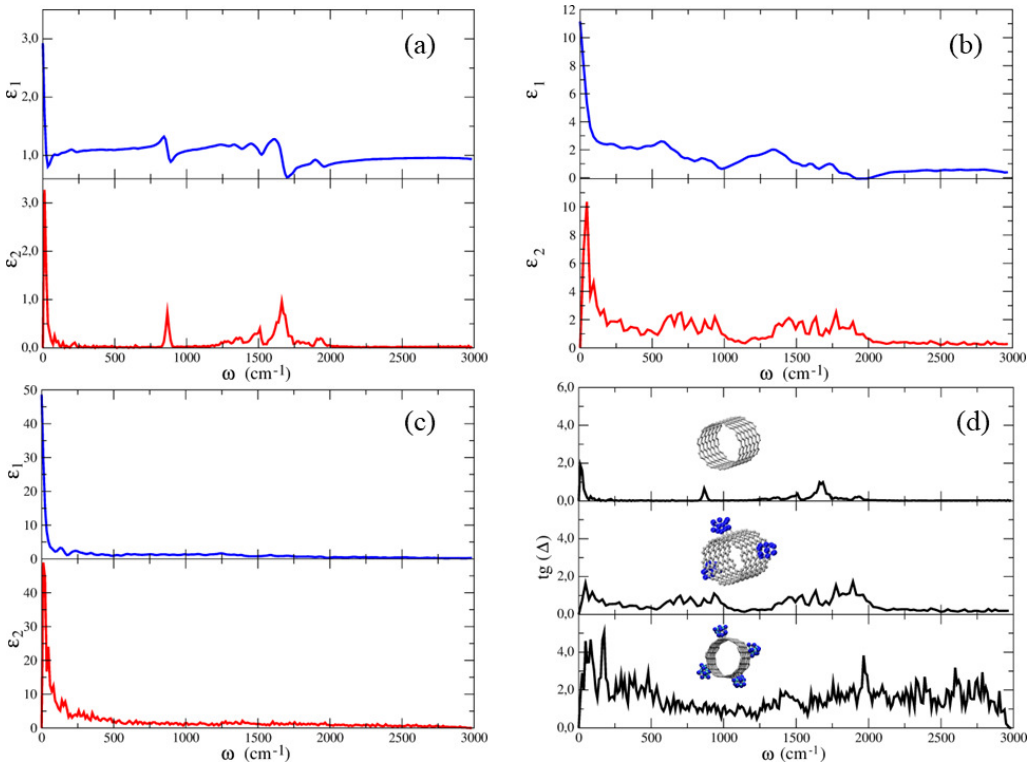

Figure 3.16. Real (blue lines) and imaginary (red) part of the complex dielectric function for the bare (10,10) CNT (a) the same CNT decorated with three (b) and four (c) Co nanoclusters. Panel (d) shows the three dielectric loss tangent curves for these three systems with the same labeling and the inset figures are a reminder of the system to which they refer.

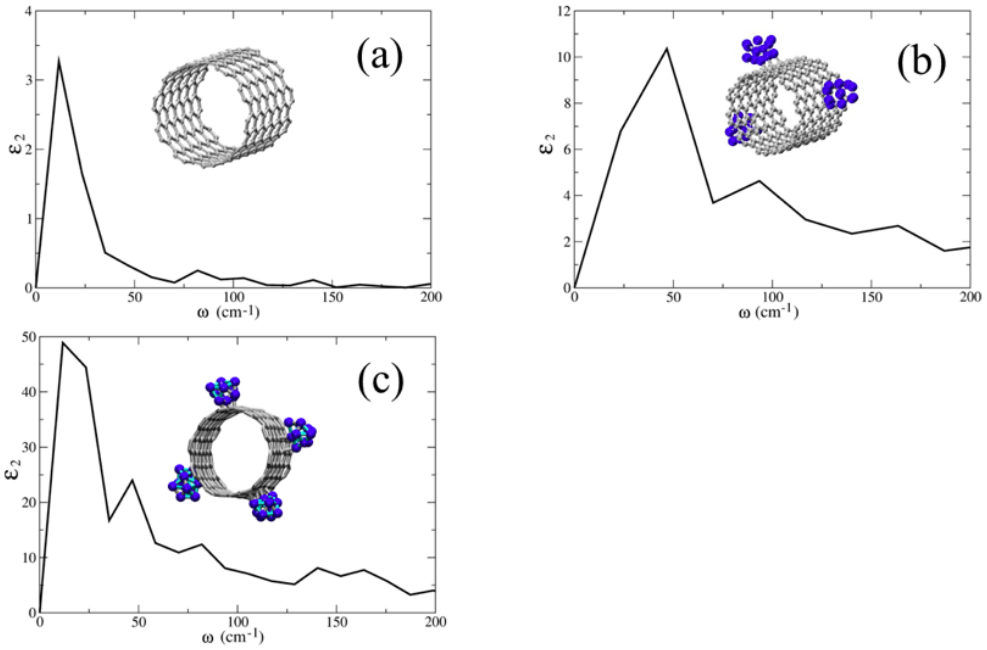

Figure 3.17. Details of the imaginary part of the dielectric function ϵ_2 for the three systems discussed in the main text in the range between 0 and 200 cm-1. Panel (a) refers to the (10,10) CNT, panel (b) to the CNT carrying three Co nanoclusters and panel (c) to the case of four Co nanoclusters. Each inset figure is a reminder of the system to which the plot is refereed.

nanoparticle or nanocluster. These collective modes are indeed the ones responsible for the low frequency part of the IR spectrum and dielectric function, thus indicating that the nature of the electrostatic interaction between CNTs and decorating heteroatoms and the size of the clusters are two major ingredients in the tuning of the response of the composite material in the targeted frequency regime.

3.4 Conclusions and remarks

The present computational analysis aims at unraveling the processes occurring at finite temperature of a system composed of CNTs decorated with small amounts of Co organized in clusters (or nanoparticles). This type of composite materials is being pioneered as possible dielectrics in a wealth of applications including aeronautics and related electronics. To date, experiments remain difficult to interpret and accurate atomistic simulations still lacking. By resorting to FPMD modeling, we could provide a direct insight into the atomic structure and its evolution at finite temperature. The explicit inclusion of the electronic structure and its evolution along rather long-lasting dynamical simulations allowed us to extract the dielectric response of this type of systems, evidencing the dependence of this measurable quantities on both the chemical nature of the system and the amount of Co added to trigger the absorption over a broad frequency range. The deep study of the structural defect and electronic structure due to the dynamical study and the MLWF method allowed had a better understanding of the atomic behaviors that produce those dielectric response. We are aware that the microwave range is hard to reach due to the intrinsic difficulty of quantum-based simulations which are by their own nature bound to the ps time scale (e. g. a 300 ps simulation corresponds to a low-limit frequency of ~ 3 GHz$= 0.1$ cm^{-1}). Nonetheless, this is a first attempt at pushing this type of modeling toward the limits of present high-performance computing architectures and massively parallel codes. The results obtained show that thermal stability problems can affect the microscopic organization of the system which however does not undergo disruption or chemical dissociation separating in an irreversible way the Co and the carbon-based components. Furthermore, our study can provide a guideline for a rational design of compounds suitable to these applications and a hint to stimulate molecular modeling in this rapidly evolving field.

Chapter 4

Structural, chemical and electronic properties of carbon nanotubes interacting with PMMA

Summary

In this chapter, we aim at probing the limitations of our fluctuation–dissipation approach and propose a way to overcome these limits to extract the frequency information interesting for the purposes of my research project. Following the guidelines sketched in the previous chapter, we still focus on CNTs systems within the wide family of carbon-based materials. However, at variance with methods consisting in the addition of metallic nanoclusters and nanoparticles at the external surface of CNTs, our discussions and synergy with the experimental groups oriented our research toward a new horizon. A viable alternative to induce modifications in the spectral response of CNT is to embed nanotubes inside polymer matrices. This has the advantage of constraining the CNTs oscillations without the need for expensive and somehow rare metals. Instead, rather common commercial polymers, for which matrices and substrates for CNTs can be obtained with relatively affordable 3D printing techniques, seem to be able to modulate the electromagnetic response of a composite system consisting of CNTs and hydrocarbon-based polymers in mutual interaction. On a first attempt, due to the lack of precise information at an atomic and molecular level, we still resort to CPMD-based simulations and associated post-processing methodologies. In this regard, I wish to clarify that during the period I worked on this chapter, I had to do a lot of attempts and tests on many different systems. This isn not unexpected when a new route is explored and experimental data are as scarce as the computational ones. It is then not surprising that some *virtual* experiments I conducted resulted in a failure or a negative result. This is not a limitation just of the theory and computational method, but a more general problem that bothered both experiments and modeling. For these reasons, it took me a considerable amount of time to identify the right systems, the right sizes and to eventually proceed to their characterization. Some components of these systems had to be chosen somewhat arbitrarily due to a lack of data and the fact that these same data are not disclosed as part of the industrial secret. This is the case, in particular, of the poly(methyl methacrylate) PMMA polymer, briefly indicated as PMMA in jargon. How these polymer are conceived, synthesized and which capping groups are used to terminate the two ends of the (more or less) long PMMA polymeric chain of the main body were *uncharted territory* during my doctoral thesis. I managed to figure out the main features of the PMMA of interest for our applications from accessible publications (Elsevier, https://www.sciencedirect.com/topics/materials-science/poly-methyl-methacrylate) and from the few data disclosed by vendors (https://sartomer.arkema.com/

and https://polymer-process.com/pmma-polymer/) and only after dynamical equilibration and comparison with experimental structural and spectral data I could reach a confidence level sufficient to pursue my work. In this chapter, I shall then show to which extents dynamical approaches can be applied and which are the intrinsic shortcomings to achieve good microwave spectra. In the second section of this same chapter, I shall focus on the study of vibrational modes of our systems to push the analysis to the lowest possible frequencies and to gain a better understanding of vibrational modes and absorption mechanisms.

4.1 Motivations, system studied and methods

4.1.1 Motivations

While the core of my PhD work lies in the study of specific carbon-based systems and composites for electromagnetic response, the atomic level underlying mechanisms turn out to be of fundamental interest for a complete understanding of the desired properties. In this respect, various physical and chemical phenomena occur, all of them contributing to the overall behavior of the compound obtained, thus they are worthy of investigation for a rational design of devices. Simultaneously, a computational analysis of the advantages and limitations of the present forefront simulation methods has never been conducted on these complex materials, and this is also a task of my research work. Both these aspects represent the driving motivation and a key aspect of my doctoral project. I shall then present the results obtained (and obtainable) with tools and methods employed, along with a critical reflection on their relevance in providing insights or posing stumbling blocks to the desired knowledge in terms of response in the microwave domain.

For the reasons briefly summarized above and in view of the mutual collaboration within the *laboratoire commun* MOLIERE, I had the opportunity to interact directly with Sylvie Martinez, Ph.D. student at the University of Bordeaux (France), whose experimental work involves the use of carbon-based nanocomposites for 3D printing to develop new materials for microwave absorption applications. This has given a new steering to my own research, being the target of both parties the same, as well as the frequency range to be explored. This as actually been my first direct contact with systems consisting of polymer matrices into which various carbon-based compounds are incorporated, from nanotubes,

up to the percolation threshold, to graphene oxide. A direct extension of the systems studied in the former chapter was then CNTs interacting among them, as collective multi-CNTs ensembles and in interaction with polymers of the PMMA type. In this context, I first focused on the atomic-level phenomena regulating the assembly of CNTs and their interaction with PMMA to understand the underlying mechanisms and assess whether polymer-CNT compounds can be optimized inview of their resulting dielectric properties and absorption spectra.

4.1.2 System description

The experimental system indicated above consists of a polymer matrix filled with CNTs up to the percolation threshold. Yet, little is known about the actual role of the polymer and its specific interactions with CNTs. This will then be my first task: characterize all the plausible systems used as building blocks for the composite and unravel the interaction between the CNTs and the PMMA polymer. The scope is to understand the behavior of the consituent blocks as stand-alone components and the nature of the mutual interaction between the external surface of CNTs and a nearby polymeric chain (or chains). The single single-walled CNT, which has been studied in the former chapter, provides a template to start the present analysis. Thus, the subsequent step becomes the interaction between CNTs. Working in the frame of percolation threshold means that this kind of interactions occur very often in the real material. The model system we constructed to represent this situation is composed of two (10,10) CNTs, each one including 240 C atoms. In this model, we started with a distance between the two CNTs equivalent to one single C–C bond length (1.435 Å). The c direction, namely along the axis of the cylindric topology of CNTs, has the same length of the single-walled CNT studied in the former chapter and amounting to 14.77 Å. The simulation cell is orthorhombic and has the dimensions $a \times b \times c = 42.33 \times 42.33 \times 14.77$ Å^3. The large a and b sizes ensure sufficient separation from the periodically repeated images to avoid spurious interactions, whereas the periodicity along c ensures a virtually infinite CNT length.

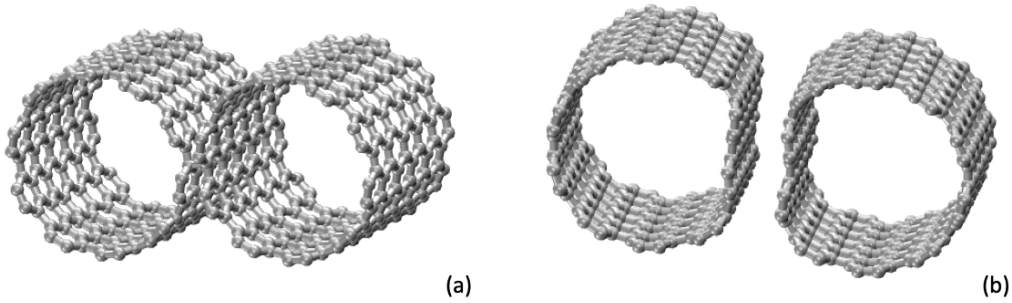

Figure 4.1. (a) Initial configuration of the simulated systems consisting of two (10,10) CNTs of 240 C atoms each in interaction at the mutual distance of one C–C bond length. (b) Resulting Coulomb repulsion observed during the dynamics of the system, where the two CNTs depart from the initial distance and become separated by about 3.9 Å.

During the NVE phase, following the same protocol reported in section 3.2.2, we observed that the initial C–C bond length distance between the CNTs is not kept. On the contrary, the Coulomb repulsion is the dominating interaction resulting in a quick separation of the two CNTs that eventually equilibrate at an average distance of 3.9 Å. Summarizing, as soon as the dynamical simulation starts, the system is in an unstable configuration from which it departs spontaneously. To get a better understanding of this process, we considered also defective CNTs, so unravel whether or not a tighter interaction

among adjacent CNTs can occur. Indeed, industrial CNTs usually carry impurities and defects consisting in vacancies (where C atoms are missing) that could potentially enhance chemical bonding between two CNTs. For this reason, I explored this possibility in my computational investigation. To this aim, a nearly identical system was created with a unique basic difference: in one of the CNTs one C atom i was removed, thus creating a mono-vacancy. The scope was to check if the presence of such a vacancy, hence unsaturated C atoms around it, is sufficient to induce the formation of chemical bonds between the two CNTs, thus binding them. The result of the dynamics has shown, instead, that despite a slight attraction originated from this area, the overall electrostatic repulsion between the two CNTs is still the dominating feature, resulting in a separation of the two CNTs. The main reason is that, despite point-like defects at their surface, CNTs aligned in a parallel arrangement present still a large electrostatic repulsion that prevents the formation of stable chemical bonds. Yet, there is no guarantee that a perfect parallel orientation of the CNTs is the actual experimental situation. In fact, the difficulties in growing *in situ* under controlled conditions parallel sets of identical CNTs makes this situation a wishful thinking rather than a reality. We considered then the case of non-parallel configurations among CNTs. To this aim, we built a system consisting of two (10,10) CNTs in which one of the two, formerly aligned in the system discussed above, is now rotated of 90^o resulting in two CNTs orthogonal to each other. The two CNTs are composed of 320 C atoms, as opposed to the 240 atoms case of the parallel alignment discussed above. This increased size was motivated by the need to apply periodic boundary conditions (PBCs) on both the CNTs while preserving an identical number of atoms on both to avoid any possible biasing due to size mismatch. Hence, the simulation supercell becomes an orthorhombic box of $37.04 \times 19.73 \times 19.73$ Å. Following our assessed protocol, an NVE simulation was followed by an NVT one at room temperature which lasted for 5 ps, showing that this system is dynamically and thermodynamically stable. The selected rotation angle between the two nanotubes represent clearly the extreme case of non-parallel arrangement. We observed that approaching these two CNTs at a distance of a C-C chemical bond length, upon generating a C vacancy to facilitate the creatin of a chemical bond, gives a stable structure at $T = 0$ K, but, at finite temperature, the structural deformations are sufficient to cleave this C-C bond between the two tubes and the two undergo separation. A conclusion that can be drawn is than that the presence of vacancies is insufficient to create stable bonds between CNTs and this is independent on their relative orientation. The possibility to

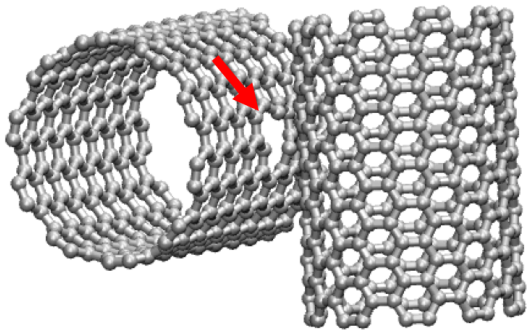

Figure 4.2. Simulated systems consisting of of two (10,10) carbon nanotubes of 320 C atoms each. Their interaction is enhanced by the removal of a C atom to create a vacancy in the contact area, highlighted by the red arrow. As discussed in the text, this is not sufficient to promote the formation of stable chemical bonds between the two CNTs.

have CNTs bound to each other via actual chemical bonds seems ten ruled out. We have, instead, found that two CNTs naturally separate reaching an equilibrium distance of 3.9 Å.

Former works [117] have assessed that two CNTs separated by distances ranging between 3.4 and 6.1 Å can still be regarded as interacting and, in this respect, the value I found is compatible with this conclusion. On the basis of my dynamical simulations results and these published data, I considered two CNT oriented parallel to each other and separated by a distance of 5 Å as still interacting. In fact, they do not separate further all along the dynamical simulation and can thus provide a well assessed template for the present study. Due to the mutual parallel orientation identical to the one used all along this chapter, I could use the 240 C atoms CNTs of length 14.77 Åand an orthorhombic simulation cell of $a \times b \times c = 37.04 \times 37.04 \times 14.77$ Å, with the same boundaries conditions applied earlier. This gives two CNTs virtually infinite along the c axis and an empty space around them sufficiently large to avoid spurious interactions between the two CNTs induced by the periodicity along a and b axes. This is the CNT system for which I studied the interaction with a polymer of the same type used experimentally as a host for nanotubes in the sense mentioned in this chapter and discussed in the first chapter.

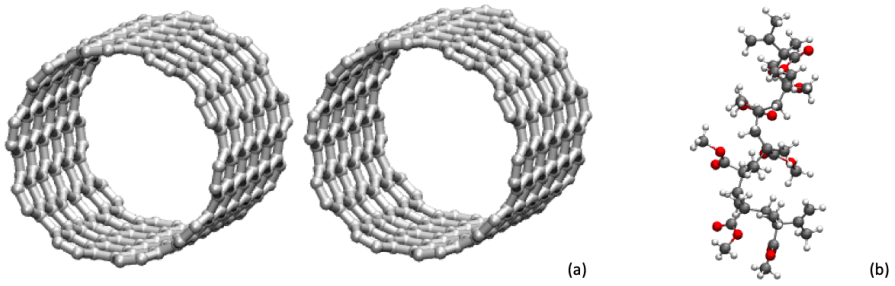

Figure 4.3. Simulated systems consisting of (a) two (10,10) carbon nanotube composed by 240 C atoms each in interaction at a distance of 5 Åand (b) a PMMA polymer composed by seven monomers, and terminated by methyl functional groups.

The structure and chemical composition of the polymer was a considerable stumbling block in my research project. Despite active synergy and frequent exchange with the experimental counterpart, the information needed to construct a polymer was always poor and lacking in all the atomistic details required by the type of simulations used all along my project. From the data provided to us, we could only find out that the resin used for 3D printing by DLP was an industrial blend (IB) provided by the FunToDo company (Netherlands) for which detailed chemical information is not disclosed. The type of polymer was indicated as a PMMA type carrying different acrylic or methacrylic monomers and oligomers. Thus, for our modeling purposes, we considered the best known and mostly used methacrylic based PMMA polymer, typical component in ionic gels and photonic materials in the majority of the reported experiments. The length of a PMMA chain is composed of a variable number of monomer units, depending on the synthesis protocol. In our modeling, to avoid uncontrolled displacements, undesired conformational changes and possible spurious interaction with periodically repeated images, we decided to work with a PMMA polymer whose size is comparable to the simulation cell size and the nanotubes. For this reason, our PMMA chain consists of seven monomers and is terminated by methyl functional groups as shown in panel (b) of Fig. 4.3. We stick to an unfolded configuration and used a $26.46 \times 26.46 \times 26.46$ Å^3 orthorhombic simulation box. The first step was to optimized the PMMA structure prepared in this way at the DFT level, followed by a free dynamics on a ps time scale in the microcanonical NVE ensemble. Once we were confident that the system did not go any anomalous behavior or spontaneous bond cleavage, we started a canonical NVT dynamics at room temperature (300 K) lasting for 7 ps. These two reference systems, the two CNTs and the equilibrated PMMA polymer, we constructed the composite CNT/PMMA systems. The two better

suited to the scope of our simulations are the ones presented in this chapter. We skip the tedious and often disappointing work done to arrive at a reasonable CNTs+PMMA model, although I wish to recall this demanding task "behind the scenes". Our first task was to verify whether the approach of PMMA can perturb the stability of the CNTs in mutual equilibrium. To this aim, we positioned our model polymer as close as possible to the spatial gap between the two CNTs. We observed that while the system seems stable during a microcanonical NVE simulation, the PMMA is departs from the CNTs as soon as finite temperature simulations (NVT) are attempted, while the two CNTs preserve their stable distance discussed above. In summery, we ended up with two CNTs at their equilibrium separation and an independent PMMA polymer far away inside the same simulation cell. This seems to indicate that a direct interaction between CNT and PMMA is not what such a composite would realize. Yet, the experimental procedure of embedding CNTs in a polymer matrix indicate that these two subsystems are forced to coexist. To try to mimic this situation, we considered a second system in which the two (10,10) interacting CNTs obtained above are extended to 400 C atoms each to allow for a sufficiently long unfolded polymeric chain to be commensurate. Then two PMMA polymers are approached to the couple of CNTs, one from the side and one from the top in the empty space separating the two CNTs, as sketched Fig. 4.4. Using an *ad hoc* tuned box size, the PBCs mimic the paired CNTs at the equilibrium distance surrounded by PMMA on both the left and the right sides of Fig. 4.4, close to the situation that a polymer matrix surrounding the CNTs would realize. The increased simulation cell hosting the two CNTs and the two PMMAs

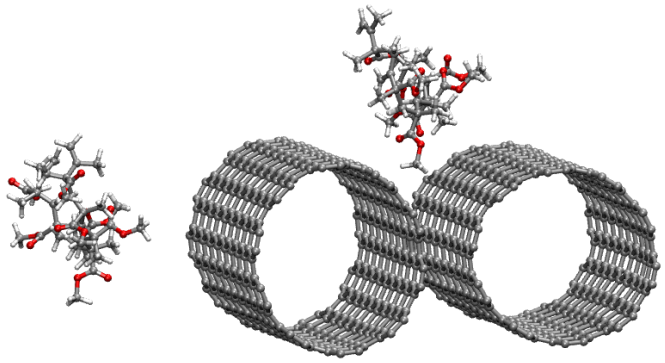

Figure 4.4. Simulated system consisting of two (10,10) CNTs of 400 C atoms each in interaction at a distance of 5 Å, carrying two PMMA polymers on top in the interstitial space between the two CNTs and on the side, where the system is periodically replicated.

is still orthorhombic with sizes $48.68 \times 24.34 \times 25.10$ Å^3. This box size ensures that the PBCs act on the system as follows: (i) the PMMA placed on top of the two CNTs, above the 5 Åinterstitial space, becomes replicated also on the bottom side, and (ii) the one on the side is also replicated on the opposite side of the two aligned CNTs.

4.1.3 computational method and parameters

Simulation Protocol

Following the consolidated approach benchmarked in the previous chapter, we performed dynamical simulations as implemented in the CPMD code, following the protocol described in Section 3.2.2. Each calculation started with an electronic structure optimization for each new system constructed. Then a structural optimization phase, consisting in an annealing via damped dynamics, was used to check for stability and bring the system on its local

minimum. A subsequent stage consisting in a microcanonical NVE dynamics allow to asses the stability of the system (or to discard it in case of negative results). If the system passes this initial set of computational stages, then canonical NVT simulations are performed to inspect the behavior of the model at finite temperature and to extract physical values.

Parameters and preparation

For the systems composed by one (10,10) CNT, the numerical integration of the Car-Parrinello equations of motion was done with a fictitious electron mass of 380 a. u. and an integration step of 4 a. u. (0.097 fs). We checked that these values ensured good numerical control of the constants of motion during both the NVE and the NVT dynamical runs.

The exchange and correlation functionals adopted were the Becke exchange and Lee–Yang–Parr correlation (BLYP). The BLYP functional was complemented by the inclusion of van der Waals interactions according to the maximally localized Wannier functions implementation. The core-valence interaction was described by a norm-conserving numerical pseudo-potential of the Troullier–Martins type for carbons and oxygens, for hydrogen an analytical von Bart-Car pseudo-potential was used. Up to this point, then, the computational set-up does not differ from the one adopted in the previous chapter.

Due to the increased size of the systems modeled in this chapter, amounting to 1035 atoms in the case of two CNTs and two PMMAs, we reduced slightly the PW basis set cutoff energy from 100 Ry (1360.6 eV) to 90 Ry (1224.5 eV) to make the calculations affordable on our HPC platforms. For the same reason, to speed up the simulations, the time step was set to 5 a. u. (0.121 fs). We remark that, while a good separation between electronic and ionic degrees of freedom is kept on the time scale of our simulation, a monotonic increase of both the ionic and the fictitious electronic kinetic energies lasts for about 9 p, as shown in Fig. 4.5. Only after this long initial equilibration time the large systems reach a steady dynamical behavior. This is a clear indication of the difficulty and workload that models including 1000 atoms (or more) represent in a first principles framework. The trend shown in Fig. 4.5 indicates that a careful tuning of the simulation

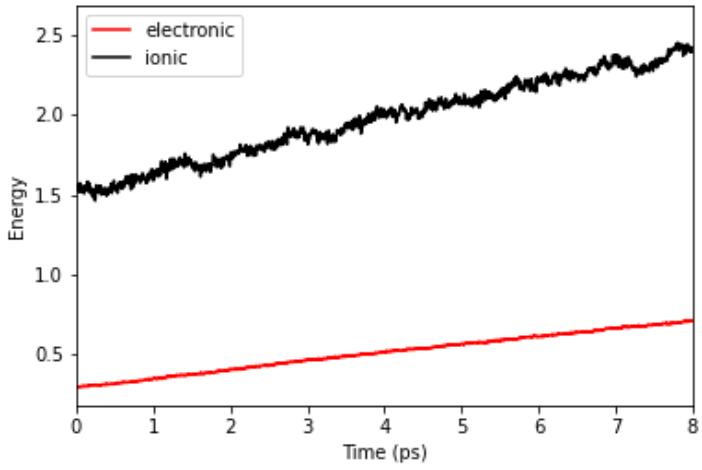

Figure 4.5. Kinetic energies of the ionic subsystem (red curve) and the fictitious one of the electronic subsystem (black curve) for the system composed of two CNTs of 480 C atoms in the NVT ensemble at 300 K, showing a clear energetic separation of the two sets of degrees of freedom and the monotonic increase in the first 8 ps mentioned in the text.

parameters has to be done to ensure a proper conservation of the constants of motion larger systems and longer simulations. According to our experience with this specific system, we needed to use a fictitious electron mass was set to 800 a. u. and, simultaneously, the

wavefunctions PW basis set cut-off was again slightly reduced to 80 Ry (1088.5 eV) to make the simulation feasible. Contrary to the case of the former chapter, where metallic Co atoms were involved, here we do not have semicore states or particularly hard atoms that would require a higher cut-off. I wish also to remind that, according the relation described Section 2.3.3, the choice of the time step is correlated to the electron fictitious mass. Thus, the time step was set to 5 a. u. (0.121 fs). All calculations have been done in a spin-unrestricted approach and the sampling of the Brillouin zone of the reciprocal space of the simulation cell was limited to the Γ point. In all the canonical NVT simulations presented in the ongoing discussion, the temperature was controlled by a Nosé-Hoover thermostat chain. Simulations were performed with the CPMD package.

4.2 Dynamical simulations

To inspect the structural properties and overall behavior of the targeted model systems, we performed FPMD simulations following the described protocol. To give an idea of the computational workload, I bring to the attention the fact that the system composed of two CNT of 480 atoms, simulated on the Strasbourg HPC cluster, required 336 cores to achieve a simulation time of 22.34 seconds per time step, allowing us to obtain a 21 ps trajectory at 300 K in the NVt ensemble. The larger system consisting of two CNTs surrounded by the PMMA polymers, amounting to 1,036 atoms, the local HPC resources of our mesocenter were clearly insufficient and we had to resort to the HPC platform (IRENE AMD-Rome) of the TGCC center. This simulations required 4096 cores to achieve a simulation time of 10.83 seconds per time step, and we could accumulate statistics for about 9 ps, once the system was stabilized at 300 K. This somehow still short time, far below what would be desirable, but on the verge of what we can afford, coudl be compared with the outcome we already have on the isolated CNT to verify to which extent we can extract physically meaningful quantities and what are the fundamental differences of the composite system with respect to a bare CNT.

4.2.1 Structural deformations and geometrical characterization

To analyze and compare our three systems, the stand-alone CNT, the system composed by two CNTs and the two CNTs interacting with PMMA, can start with some general observations. The noticeable feature is that during dynamical simulations, an isolated CNT system does not exhibit any significant structural deformations apart from standard vibrational modes, from C-C stretching to collective modes such as the *breathing* like behavior of the CNT as a whole. This, as expected, does not occur when some other system, either a nearby CNT or PMMA polymers, are present inside the same simulation cell. In fact, the presence of additional macromolecules induces substantial structural deformations. The main one observed, and shown in Fig. 4.6, is a trend to assume a pseudo-elliptical in the diametral section by both CNTs. This process occurs periodically along horizontal and vertical directions, aligned with the axis formed by the cross section of the two CNTs and it is clearly observable during the finite temperature simulation performed. This shape change is also referred to as *ovalization*. To quantify this ovalization we can make use of the specifically designed ovalization parameter, O, defined as :

$$O = \frac{D_{max} - D_{min}}{D_{moy}} \tag{4.1}$$

where D_{max} and D_{min} are the largest and the smallest measured diameters of the CNT, respectively. The denominator $D_{moy} = \frac{D_{max}+D_{min}}{2}$ is the average diameter of the CNT. The frequency of this ovalization is then calculated from the time evolution of this parameter, shown in Fig. 4.7. For our cases, We obtained a value of 552 Hz for the two

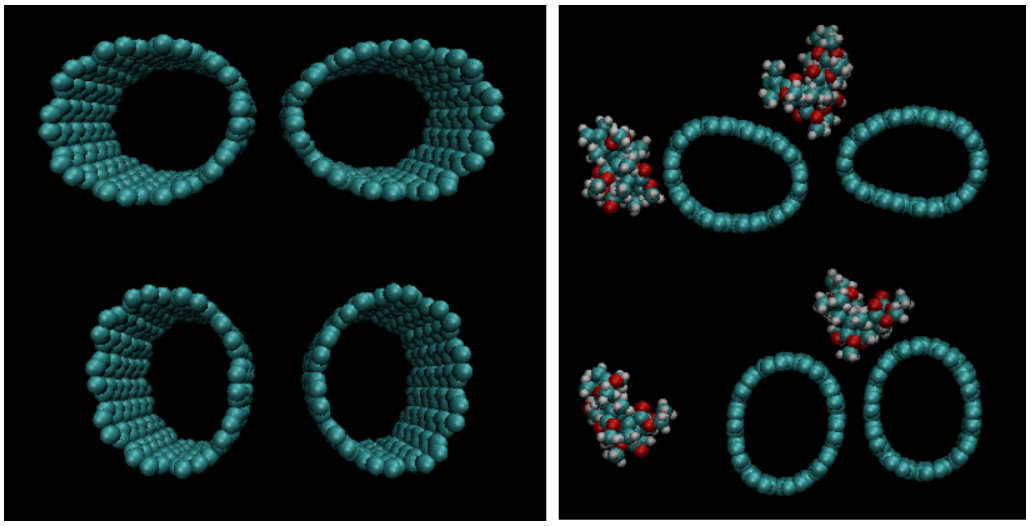

Figure 4.6. Structural deformation occurring during the dynamics when two CNTs are sufficiently close to be regarded as interacting in the sense specified in the text. The left pane shows this feature for two CNTs nearby. The right panel shows the same phenomenon occurring for CNTs in the presence of PMMA.

CNTs, which correspond to 18.4 cm^{-1}, and 447 Hz (14.9 cm^{-1}) for the composite system CNTs and PMMAs. We remark that, in the case of the system composed of two CNTs

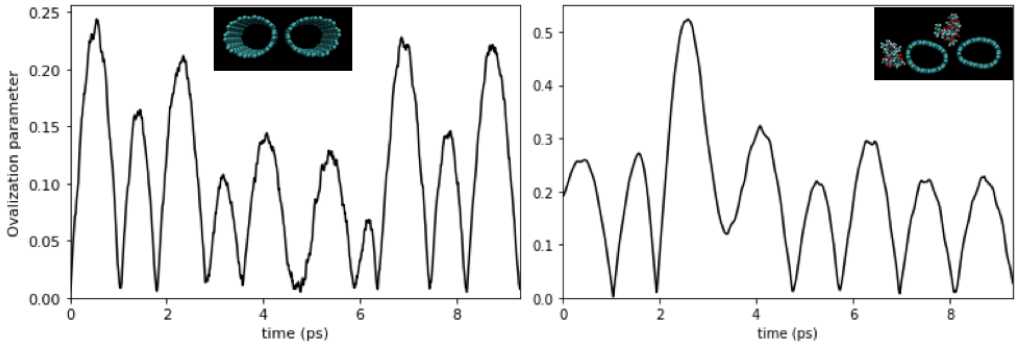

Figure 4.7. Ovalization parameter as a function of the simulation time computed during the NVT dynamics at 300 K. The left panel refers to the two interacting CNTs and the right panel to the composite system of two CNTs and two PMMA polymers.

and two PMMAs, a significant deformation is observed in the time window between 2 and 5 ps. This deformation results from a sudden temperature change introduced during the rescaling procedure adopted, which caused a temporary distortion of the nanotubes, although not inducing permanent effects. The structure equilibrated smoothly and did not depart from its initial configuration.

As highlighted in the previous chapter, a key factor in calculating absorption and dielectric properties is the analysis of the time evolution of the dipole moment of the system. To this aim, two major requirements are needed. First, a well equilibrated structure is needed to accumulate statistics and generating a consistent time series of dipole moment values along the trajectory. Second, the relaxation and equilibration of the internal vibrational modes, such as the C–C bond stretching of CNTs, has to be achieved. While overall structural oscillations at the equilibrium primarily contribute to low-frequency responses, the variations in bond lengths play a crucial role at high frequency (as expected) but, in turn, influence the collective modes at lower frequencies. On one hand, changes in bond lengths directly induce variations in the dipole moment, and are therefore intrinsically linked to

absorption properties in the high frequency range of the spectrum. On the other hand, the strength of these bonds determines the extent to which structural modifications can occur, thus influencing also the low frequency range. To get a better insight into these issues, we computed the interatomic distances of our CNTs systems. To highlight the effects of intermolecular interactions in these systems, we divided our study into three distinct spatial regions. The first region, referred to as the contact zone, corresponds to the area of closest proximity between the two CNTs, where the interatomic interaction forces exerted on nearby atoms on both CNTs are the dominant feature. The second region encompasses the lateral zones aligned along the axis of the two CNTs. The third region includes the more distant atoms of each nanotube, where the influence of inter-tube interactions is minimal. Within this criterion, we obtained average interatomic distances for each region during the dynamical evolution of our systems. The time variation of these distances allow to define a *collective* velocity and from the computed autocorrelation function of the temporal variation of these average distances a Fourier transform provides the spectra reported in Fig. 4.8 for the case of two aligned CNTs in their interacting configuration discussed above. What we observe is that, regardless of the region considered, the spectra exhibit

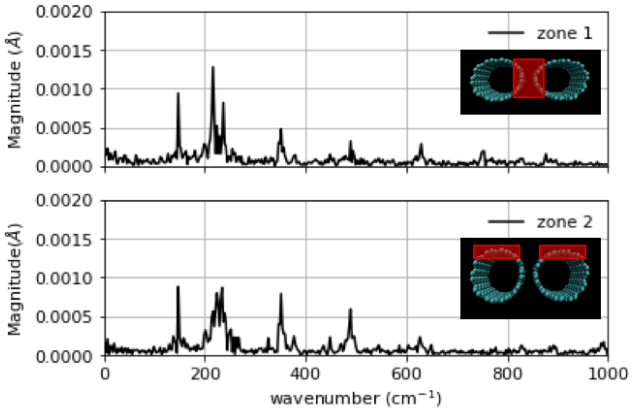

Figure 4.8. Vibrational spectra of the two zones consisting of atoms close to the interacting region between the two CNTs (zone 1) and C atoms away from direct inter-CNTs interactions (zone 2). Further details are provided in the text.

several main frequency peaks: the first at 144.4 cm^{-1}, the second at 239.6 cm^{-1}, the third at 354.2 cm^{-1}, and the fourth at 481.8 cm^{-1}. The intensity of these peaks decreases with increasing wavenumber. In addition, the shape of the 239.6 cm^{-1} peak varies depending on the region. In weakly interacting zones, such as the one labeled as zone 2 in Fig. 4.8, the peak is broader, whereas in the interaction zone (zone 1), it splits into two distinct components, accompanied by a slight enhancement of the amplitude. In this latter case, a secondary peak emerges at 216.6 cm^{-1}, with an intensity larger than that of the other satellite peaks.

One of the questions raised by these results is whether the observed peaks are artifacts of the simulation or if they reflect some important physical feature that could also be detected in other systems under different conditions. To address this issue, I repeated the same analysis for the various systems studied in my project, namely: an isolated CNT, a system of two interacting CNTs, and a system composed of two CNTs and two PMMA polymers. The results are summarized in Fig. 4.9, where the main peaks around the same frequencies seem to be constant feature of all the systems considered. As observed in the previous figure, the shape of the peak around 239.6 cm^{-1} is the one that displays the major modifications depending on the system. For the isolated CNT, this peak appears as a single sharp feature. For the system consisting of two interacting CNTs, the peak splits into two

components and seems to be a signature of a *collective cooperation* between the two CNTs. Finally, for the system consisting two CNTs and two PMMA polymer chains, rather than a distinct peak, we observe a sort of broad band accompanied by general increase in low-frequency range below 100 cm^{-1}. This is an encouraging result in view of the attempts at enhancing a response in the microwave regime and a sign that the inclusion of PMMA polymers helps in slowing down collective modes which can become active in the range of interest. While the physical interpretation of these peaks remains unclear to some extent,

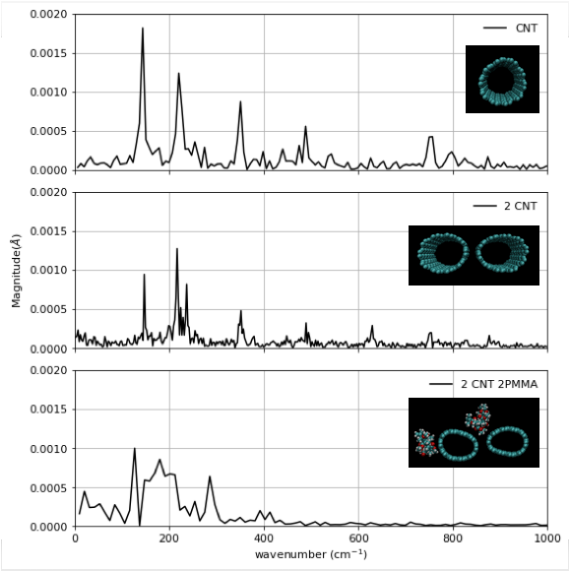

Figure 4.9. Vibrational spectra analogous to the one shown in the former figure computed for an isolated CNT (upper panel), a system of two CNTs at interacting distance (central panel) and a composite system formed by two CNTs and two PMMA polymers (lower panel). Details are discussed in the text.

what can be stated with a certain degree of confidence is that the arising of new secondary peaks, especially in the low frequency range, is a direct consequence of interactions between the various components of the system. In the case of two interacting CNTs, we observe the appearance of intense, localized peaks. Conversely, in the composite CNT–PMMA systems, the addition of the polymer leads to the arising of numerous medium-intensity peaks at low frequencies, indicating that the PMMA does not play only the role of an inert substrate to host the CNTs, but actively acts in decreasing vibrational modes, thus providing a practical way of tuning the response in the low-frequencies range.

We can infer that the observed frequency shifts originate from the spatial proximity of the building blocks that slow down or hinder certain vibrational modes, acting as a sort of local environment constraints. Specifically, the proximity of the CNTs mutually interacting and the approach of the PMMA polymers result in a modification of the low frequencies mode of a bare and isolated CNT. Conversely, the typical C–C stretching modes are less affected by these surrounding constraints. To corroborate this hypothesis, I analyzed the minimum inter-tube distance in each of the systems targeted in this study. This analysis aims at quantifying the extent of mechanical coupling or steric interaction between the CNTs and potentially correlate this with the arising or modulation of specific vibrational peaks. The results are presented in Fig. 4.10. The trend shown by the distance between the two CNTs as a function of the simulation time suggests that the oscillations have a certain periodicity. Hence, given this periodic behavior, it should be decomposable into a sum of sinusoidal functions. To fit the curve, I therefore used a series of test functions of

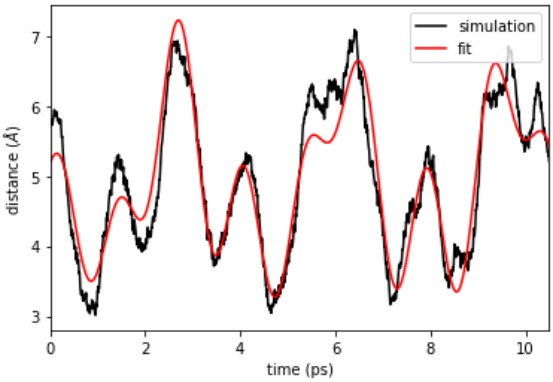

Figure 4.10. Distance between two CNTs as a function of the simulation time (black line) and fitted analytic function (red line) according to the procedure explained in the text.

the following analytic form:

$$f(t) = \sum_i A_i sin(\omega_i t + \psi) + \epsilon \tag{4.2}$$

In the specific case shown in Fig. 4.10, an acceptable fit was obtained by modeling the signal as the sum of three periodic functions. The parameters are: $\omega_1 = 7.4\ cm^{-1}$ and $A_1 = 1.1$ Å, $\omega_2 = 14.5\ cm^{-1}$ and $A_2 = 0.5$ Å, and finally $\omega_3 = 18.8\ cm^{-1}$ and $A_3 = 0.8$ Å. It is worth noting that the frequency component ω_3 closely resembles the characteristic frequency identified in the ovalization analysis of the CNTs. The second significant frequency, ω_1, appears to be associated to the collective motion of one nanotube with respect to a neighbor one, reflecting an inter-tube dynamic mode. Similarly, we identified two dominant frequency components for the CNT–PMMA system: $\omega_4 = 4.3\ cm^{-1}$ and $\omega_5 = 14.6\ cm^{-1}$. Remarkably, ω_5 corresponds to the characteristic frequency observed in the ovalization parameter analysis in a way very similar to what we found for the two coupled CNTs.

While the influence of intermolecular interactions on bond lengths can be easily demonstrated ans ascribed to specific modes, establishing a direct connection between these bond length variations and the observed structural deformations remains challenging. This is mainly due to the significant discrepancy between the characteristic frequencies associated with each phenomenon. We will therefore focus more specifically on the effects of these interactions on the bond characteristics, in an effort to get a deeper insight into the underlying mechanisms. To this aim, we paid special attention to the electronic structure features of the targeted systems.

4.2.2 Electronic structure

As seen in the previous chapter, structural modifications in our system can be induced by interactions with external elements or building blocks (e. g. the added polymers). While certain interactions, such as chemisorption, clearly influence the electronic structure, as shown in the case of CNTs decorated with Co metallic clusters, identifying analogous mechanisms in our current systems made of weakly interacting CNTs and PMMA polymers turn out to be more complex. Yet, the proximity of the two CNTs and the addition of the polymers have already been shown to influence structural and dynamical properties of the composite systems. This has a non-negligible effect also on the underlying electronic structure. Focusing on the regions that I have identified above as contact zones between nanotubes, we can compared their local electronic structure with that of regions distant from any direct interaction. Analogously, in the system composed of two CNTs and two

PMMA chains, the proximity of PMMA polymer to the nanotubes induces a new type of interaction, specifically due to the hydrogen atoms carried by the groups composing the PMMA. This could potentially lead to the formation of hydrogen bonds (H-bonds), or rather pseudo H-bonds between the CNT carbon bonds and the closest H atoms in the polymer chain [118]. Thus, I examined all carbon atoms located within 3.5 Åfrom H atoms belonging to the PMMA. This threshold distance is commonly cited in the literature [119] as the upper limit for considering a H-bond to be potentially effective. To characterize the related electronic structure, I used the MLWF method to characterize their relative distances from the most relevant atoms of the system. The result of this analysis is summarized in Fig. 4.11. In the figures, panel (a) shows that a high electron

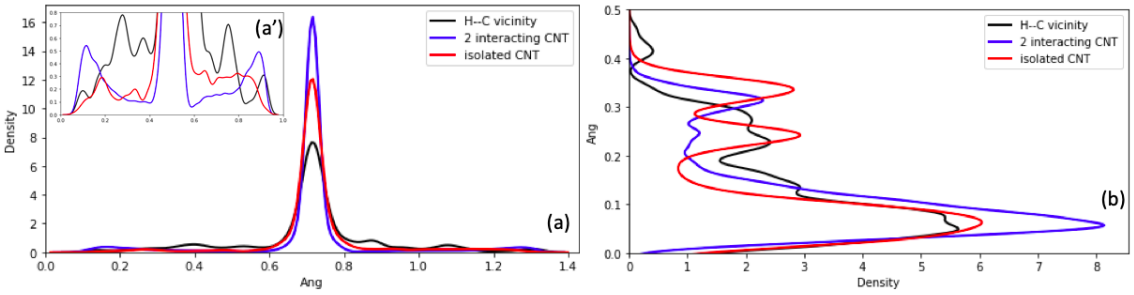

Figure 4.11. Panel (a) shows the distribution of the WFCs for the atoms at the center between the two CNTs, clearly corresponding to chemical bonds of sp^2 type. The inset (a') shows instead the π-electrons, which result clearly more delocalized. Panel (b) shows the distribution of the WFCs in the sense specified in the text.

density, namely WFCs, is present at the center between the two CNTs. These correspond mainly to σ-electrons involved in sp^2-hybridized orbitals, which are strongly localize by their own nature. As highlighted in the inset (a'), π-type electrons show a higher degree of delocalization, a feature not unexpected. In the case of an isolated CNT, the distribution of these delocalized electrons appears relatively homogeneous. In contrast, this same distribution becomes significantly more localized in the other two cases (interacting CNTs and composite systems CNTs+PMMA). When examining the vertical distribution of the WFCs, shown in panel (b) of Fig. 4.11, we observe a first peak corresponding to the localized σ-electrons, situated roughly along the bond axis. Then two broader peaks are visible. These correspond to the delocalized π bonding and π anti-bonding electrons. We can remark that in the regions of interaction between two CNTs or in areas near a (potential) H-bond, the spatial structure of this π-electron distribution undergoes modifications as a consequence of these electrostatic interactions.

These results are consistent with the outcome presented in the previous section and provide additional information on the interactions occurring among the different building blocks. Both the CNT–CNT and the CNT-PMMA affect the electrostatic interactions among the different components at least in the region in which they come in close contact, inducing consequent modifications of the local electronic structure which, in turn, are responsible for the structural modifications observed. In particular, as shown in the analysis of bond length variations, we observed the arising of characteristic vibrational peaks around 226 cm^{-1} in the regions in which two CNTs are at typical interaction distances. Furthermore, in systems where both CNT–CNT and PMMA-CNT interactions occur, modifications in bond length frequencies become more pronounced. This suggests that the proximity of PMMA not only alters the bonding environment but also affects the overall structure and the vibrational response of the composite system. As seen in our analysis of CNT ovalization processes, the presence of PMMA in the contact zone of CNTs tends to slow down the ovalization frequency, thus enhancing the response in the low frequency range.

4.2.3 Maximum entropy derived spectra for the CNTs system

All interactions occurring between CNTs or between CNTs and PMMA affect structure, deformation frequencies and electronic structure of the system, often resulting in an entirely new behavior of the system made of these building blocks with respect to the isolated pristine components. As a consequence, they influence the dipole moment and its time evolution at finite temperature which, in turn, affects the absorption and dielectric response of the material. For the system consisting of two CNTs interacting (in the absence of the PMMA polymer), Fig. 4.12 shows the infrared (IR) absorption spectrum calculated using the fluctuation–dissipation theorem in the same way discussed in the second and third chapters. The IR spectrum shows a broad band primarily in the low-frequency range, contrary to what we observed in the isolated CNTs. The first peak, aligned to the characteristic frequency $\sim$ 1600 cm^{-1} of a CNT, is reminiscent of the pristine isolated nanotube, whereas the rest of the low frequency spectrum is the result of the assembly of the different building blocks that cooperate to the response at low frequencies.

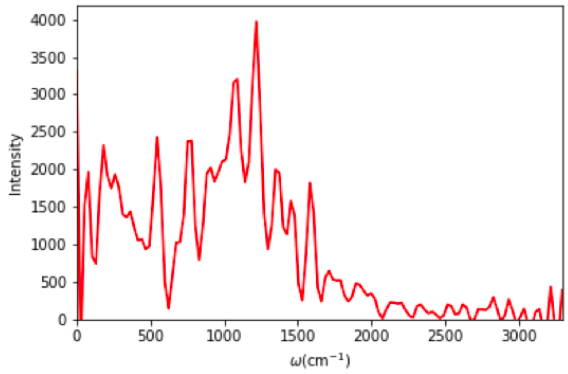

Figure 4.12. Spectrum obtained via maximum entropy Fourier transform of the dipole-dipole autocorrelation function for the system consisting of two interacting CNTs.

4.2.4 Limitations of Dynamical Methods

Although these results are encouraging in terms of both the detection of the main features and the enhancement appearing in the very low-frequency range for the system composed of two CNTs, the dynamic study has quickly revealed its limitations in terms of maximum simulation time (t_{max}) that makes impossible to appreciate frequencies $\omega < 2\pi/t_{max}$. This stumbling block is even more evident in the case of the CNT-PMMA system, amounting to 1036 atoms and 3816 electrons. Indeed, we could simulate these system only exploiting the Tier-1 HPC facility at the TGCC center, one of the top performing platforms in France and in Europe. Yet, as quantified above, we has to resort to 4096 cores to achieve an execution time of 10.8 s per simulation time step. This clearly indicates that very long simulation times (hence very low frequencies) are beyond our reach within this approach.

As shown in Fig. 4.13, the upper bound of the microwave frequency range (300 GHz) is reached after just 3.3 ps of simulation, which translates into a run of approximately three days on the HPC platform indicated here above. Conversely, reaching the a frequency limit of 3 GHz would require 333 ps, translating into approximately 340 days of continuous computation. The microwave regime is then clearly beyond the reach of these dynamical approaches. Summarizing, while first principles molecular dynamics methods provide a wealth of information, ranging from structural modifications to electronic structure evolution, thus disclosing rapid access to absorption spectra in the high-frequency regime, current technological limitations still prevent applications to systems composed of more than 1000 atoms over a sufficiently long simulation times scale. The computational cost

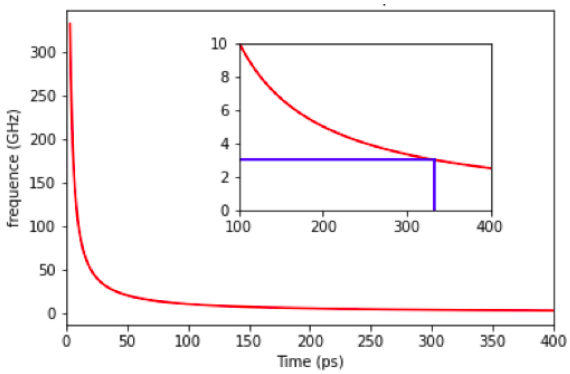

Figure 4.13. Simple plot to show the simulation time needed to reach the micro-wave range, from 300 up to 3 GHz.

remains prohibitively high for the composite materials of interest for the present research project. This pushed us to explore alternative approaches, less computationally demanding (if possible) and able to provide access to the desired frequency range while keeping the size and complexity of the targeted systems.

4.3 Dynamical matrix approach

A possible alternative to the direct numerical integration of the equations of motion, already introduced in the second chapter of this thesis, is the use of the dynamical matrix approach. Contrary to methods that rely on the generation of a time-oriented trajectory exploring the available phase space in the ergodic theory framework, which can be classified as *intensive* in terms of computer time, the calculation of the dynamical matrix is *extensive* in the sense that each atom composing the systems has to be displaced, and the electronic structure recomputed, for given increments around the equilibrium position, resulting in $6 \times N_{at}$ operations (N_{at} being the number of atoms in the system). Thus, one of the key challenges in this section will be to find a suitable compromise between the system size allowing reliable results in the desired frequency range and the computational cost that should remain manageable.

4.3.1 New systems

System selection

Since the dynamical lattice method makes use of static equilibrium configurations on forces derivatives are calculated by finite differences, we had to select carefully conformations of our systems representative of specific interactions (CNT-CNT, CNT-PMMA, etc.) able to provide reliable information. For the systems considered in my doctoral project, this can be summarized into (i) interactions between two CNTs without any PMMA, (ii) interaction between a CNT and a PMMA, (iii) weak interactions between a PMMA and a system composed of two CNTs, and (iii) stonger interactions (meaning presence of pseudo H-bonds) between a PMMA and a system composed of two CNTs. Being this method extensive in the sense given above, the size of the system determines computational workload and the simulation time needed. For this reason, we decided to limit our choice of system sizes to no more than (about) 500 atoms. The system consisting of two CNTs already amounts to 480 C atoms, hence within the affordable limits, and has not been altered consequently. For the second system, a single 400 C atoms CNT in interaction with a fully unfolded PMMA was again regarded as affordable. For the system composed by two CNTs and one PMMA interacting among them, we chose to reduce the size of the system

previously used for the FPMD simulations. the two nanotubes were downsized to 160 C atoms each, respecting the periodicity of the CNTs, and a shorter PMMA polymer chain composed by 5 and 6 monomers to mimic the weak and stronger interactions, respectively. These new systems are are sketched in Fig. 4.14. The new simulation cell for those resized

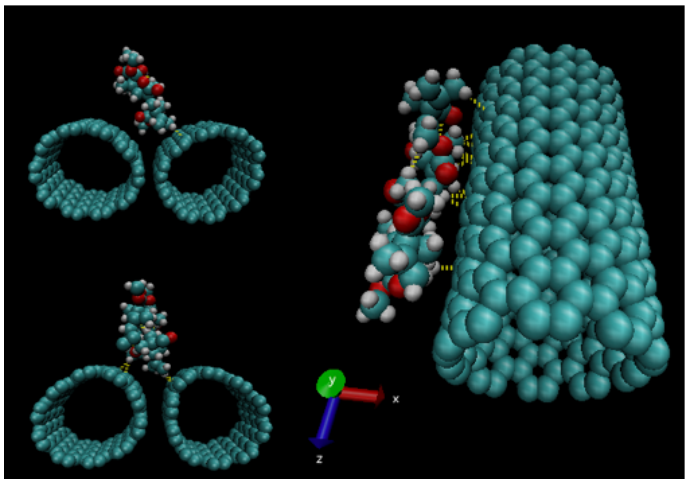

Figure 4.14. Systems used for the dynamical matrix calculations. The panel on the right shows a single CNT in contact with an unfolded PMMA polymer chain. The upper panel on the left is representative of a PMMA polymer in weak interaction with two CNTs aligned and separated by their equilibrium distance. The lower panel on the right shows the same system in which the PMMA has formed the maximum number of (pseudo) hydrogen bonds compatible with the confirmation of the system.

systems is an orthorhombic box of dimension $66.0 \times 46.0 \times 17.8$ Å^3 with periodic boundary conditions ensuring the virtually infinite length of the CNTs.

Simulation Protocol

The resized systems were selected from the dynamical simulation discussed in the previous sections. To apply the new protocol for the calculation of the hessian, its diagonalization and the vibrational modes of our systems, we first need to start with a configuration at the minimum of the potential energy surface, something that is clearly not granted when configurations are extracted from a dynamical trajectory. Thus, we first need to optimize wavefunctions and geometry of the selected snapshot. Then, following the method described Section 2.4.4, we compute the Hessian matrix of this optimized (and resized) system by finite difference method. Finally, the dynamical matrix is computed from the Hessian matrix and diagonalized to get eigenvalues (frequencies) and eigenvectors.

4.3.2 Vibrational analysis, normal modes and their origin

In Section 2.4.4 I gave a general overview of the dynamical lattice method to generate a matrix (Hessian) whose eigenvalues provide directly the vibrational normal modes of a system. This paragraph is dedicated to the application of the method exposed there. In this type of analysis, most of the eigenvalues are real and positive, apart six imaginary modes common to any system and corresponding to translations of the whole system in the three directions x, y and z and the three rotations around the symmetry axes. In some cases, values equal to zero arise and can be interpreted as rigid global modes. Considering the imaginary modes $i\omega$, they enter in the harmonic approximation of the local potential ($(1/2)m\omega^2(x - x_0)^2$) as ω^2 changing the curvature of the parabola, thus resulting in unstable and diverging configuration. To get a better understanding of their meaning, we can give a closer look at the eigenvalues and eigenvectors of the related

Hessian matrix of the system. These steady states represent a zero derivative point of the potential energy manifold, thus real eigenvalues (positive ω^2) mean that we are in a local minimum and the corresponding eigenvector shows stable oscillations of the atoms moving along its direction. Conversely, imaginary eigenvalues (negative ω^2) indicate that we are in a local maximum and the atomic motion along the corresponding eigenvector results in a system moving away indefinitely or breaking apart because of bond cleavage or disassembly in case of weak (H-bond or van der Waals) interactions. In particular complicated systems as the ones we are handling here, imaginary eigenvalues can also result in rearrangements, deformations or folding as in the case of the flexible PMMA chains. In view of these considerations, the geometry optimization phase in our protocol is fully justified because a non optimized configuration extracted from a dynamical run would have a lot of imaginary eigenvalues. As a first test case, we observe that our single CNT does not have imaginary eigenvalues, apart from the usual translations and rotations. This is due to the absence of major deformations or instabilities in our system, partly due to the rigidity of the system and partly induced by the periodic boundaries conditions. In this cases, global rotations are limited to the rotation of the whole CNT around its axis, whereas free translations are limited to the x and y directions as sketched in Fig. 4.15.

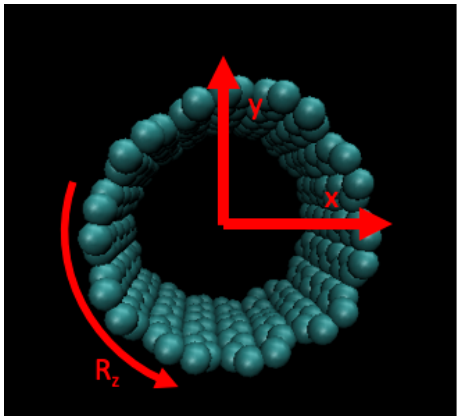

Figure 4.15. Imaginary modes for an isolated CNT. As explained in the text, in this specific case of cylindric symmetry, these modes are limited to rotation around the CNT axis and translations along x and y, orthogonal to the axis. These modes are indicated by the red arrows.

An analogous situation holds also for the two CNTs, and we could argue that an ovalization process, as the one discussed and quantified in Section 4.2.1, would give rise to additional imaginary modes. Yet, since it is a periodic (hence reversible) deformation, it is not an instability of the system, nor C–C chemical bonds are cleaved, and would rather contribute to low frequencies. For the system including PMMA, we got several imaginary and zero eigenvalues, as expected. This is indeed not surprising: a single isolated PMMA has 18 imaginary or zero eigenvalues mainly due to folding modes, formation and cleavage of intra-molecular H-bonds and conformational changes. This is even more evident in the CNT/PMMA systems, where the 40 imaginary or zero eigenvalues are mainly due to the PMMA polymer chains forming and breaking (pseudo) H-bonds with the CNTs, changing their conformation around the CNTs and approaching or departing from the CNTs external surfaces. These major structural rearrangement occur dynamically in the FPMD simulations and are an intrinsic feature of the composite material.

Positive eigenvalues, as mentioned above, correspond to stable modes not affecting te structural stability of the system, but representing its response in different frequency ranges. These modes include IR-active modes, Raman-active modes, as well as modes that are inactive in both spectroscopies. However, certain methodological challenges arise also in the use of this technique. Specifically, the finite difference vibrational analysis requires

the eigenvalues to be computed from normalized eigenvectors. As a result, it becomes difficult to retrieve the actual intensities of individual peaks in a post-processing analysis. Furthermore, determining whether a given mode is IR or Raman-active, or inactive in both, poses a challenge since the dynamical matrix approach make use only of the atomic displacement instead of the dipole evolution. In this respect, it provides a vibrational spectrum that only *a posteriori* and with several difficulties can be interpreted as IR, Raman, etc. A typical example is the case of a biatomic molecule (H_2, O_2, etc.) having always a vibrational stretching mode, but since the center of charge of the positive component (atomic charges) and negative one (electronic charge) does not vary, the stretching mode is IR silent. To overcome these limitations appropriate selection rules have to be applied. To avoid unnecessary burden to the ongoing discussion, I will proceed without distinguishing between active and inactive modes with respect to IR or Raman spectroscopies. This is also justified by the fact that our targeted range lies below the IR and Raman frequencies.

PMMA

I began my vibrational mode analysis with the isolated PMMA system. As shown in Figure 4.11, three main frequency regions can be identified in which vibrational peaks are concentrated. The first lies between 3000 and 4000 cm^{-1}, the second between 2500 and 2000 cm^{-1}, and the third below 2000 cm^{-1}. While these results are generally consistent with those reported in the literature, certain differences can be noted, particularly the presence of a central peak. These discrepancies can be ascribed to the limited size of the simulated polymer chain and the simplifications introduced for computational feasibility. Experimentally, PMMA is composed of a longer chains, whose actual length is not always under perfect control, thus resulting in different number of monomer units also within a same "product". Here, we have a PMMA chain limited to only seven monomers. Moreover, as mentioned, we have two methyl terminal groups that we were force to guess from available data and that may well differ from the ones present in industrially produced PMMA. As a result, these terminal groups are likely to influence and be overrepresented compared to experimental conditions.

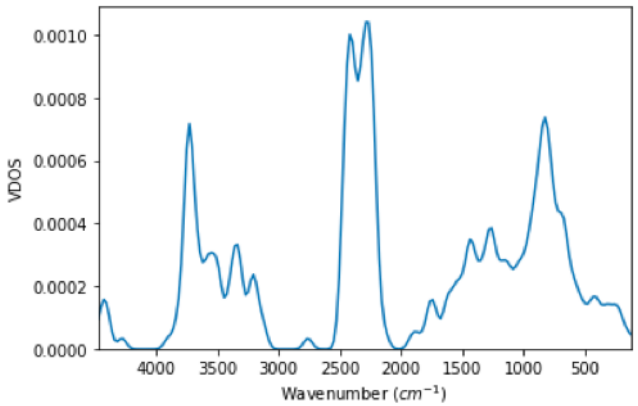

Figure 4.16. Vibrational spectrum of our simulated PMMA model consisting of seven $(C_5H_8O_2)_n$ monomers (n=7) carrying two methyl functional groups as terminal moieties of the polymer chain.

On our local Tier-2 HPC platform of the Mesocenter of my University, the geometry optimization and vibrational analysis stages required 1 hour and 37 minutes, and 2 hours and 55 minutes, respectively, on 336 computing cores. Although this result is not the ultimate target of my project, it was a necessary investigation in view of the scarce information mentioned. Moreover, it serves as an indicator of the computational workload that the dynamical matrix approach and DFT-perturbation methods require to extract the desired data. Particularly, is provides indications about affordable shape and size of

the molecular systems under investigation.

The bare CNT system

Starting with the isolated CNT of 240 atoms and using the same HPC architecture of our local Mesocenter, the calculation phase required 3 hours and 47 minutes to be completed. The resulting vibrational density of state (VDOS) is shown in the left panel of Fig. 4.17. The simplicity of the system and the extensive attention that isolated CNTs have received over the year in the scientific literature make this calculation a useful bechmark for any computational approach [120]. Several studies have demonstrated that results obtained using empirical models are consistent with those obtained here via ab initio methods. In particular, the broad peak observed above 1600 cm^{-1} is a constant feature in experimental and theoretical works. However, while the general presence of the central peak is consistent with the literature, its detailed structure differs depending on the model size and level of the theory used. Additional complications arise from the fat that is is difficult to select and control experimentally the symmetry and chirality of the produced nanotubes. In our modeling, numerous vibrational modes appear between 1200 and 1400 cm^{-1}. This vibrational activity can be attributed to the ab initio nature of our calculations, rooted in quantum chemistry as opposed to classical modeling, which reveals modes that may not be captured by simplified empirical potentials. For this system the minimal vibrational frequency calculated is 697 $^{-1}$ For the interacting CNTs, the first question I addressed

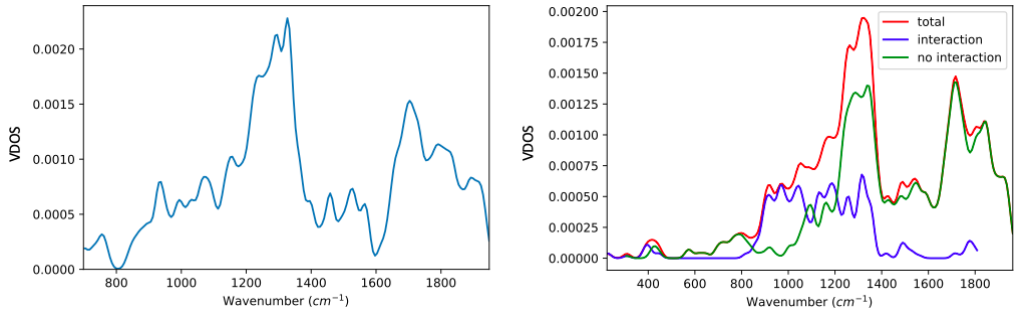

Figure 4.17. Left panel: vibrational density of state (VDOS) of a single CNT obtained from the vibrational analysis done on a (10,10) CNT of 240 atoms. Right panel: VDOS of three systems composed of two aligned CNTs of the same chirality and sizes. The red curve shows the global spectrum. The blue and green curves, instead, show the contributions of the overall spectrum coming from the interacting atoms of the two CNTsi and the non-interacting ones, respectively, as discussed in the text.

was whether system size significantly affects the vibrational spectrum. More specifically, I investigated whether it influences the VDOS as well as the minimal vibrational energy state that the system can reach. To this aim, I simulated three systems of increasing size, each representing two interacting CNTs: the first system is composed of two CNTs of 200 atoms each, the second one of two CNTs of 240 atoms, corresponding to the system described in previous sections, and the third one of two CNTs of 480 atoms each, namely twice the size of the previous case. The computation times and the minimal vibrational frequency reached are summarized in Tab. 4.1.

	1 CNT 240 C	2 CNT 400 C	2 CNT 480 C	2 CNT 960 C
computation time	3h47	10h17	39h25	419h
Minimal vibrationnal state (cm^{-1})	697.3	283.0	226.7	971.0

Table 4.1. Minimal frequencies computed for CNT systems of different sizes and CPU time needed for the dynamical matrix calculations in a FPMD approach.

As expected, system size directly influences the computational time required to get the vibrational spectrum. In fact, the results show that the simulation time grows with a dependence in power of 3 with respect to the size of the system. A cubic trend makes then unaffordable large system sizes. However, contrary to intuition, system size is not directly correlated with the lowest vibrational frequqncy reached. Indeed, it seems that the most favorable result, in terms of minimal vibrational mode toward a microwave regime, was observed for the system with two CNTs of 240 atoms. In contrast, both the smaller and larger systems failed to achieve a comparable minimum value. In view of this analysis, this intermediate system size was selected as the optimal configuration, providing the best compromise in terms of vibrational performance and computational efficiency.

The VDOS for the system composed of two interacting CNTs, each containing 240 atoms, is presented in the left panel of Fig. 4.17. The first observation is that the overall shape of the spectrum between 1000 and 1800 cm^{-1} closely resembles that of the isolated CNT, with the exception of a certain number of additional low-frequency modes. One of the advantages of this method is the ability to analyze the eigenvectors of the dynamical matrix, which allows us to identify the specific atoms involved in each vibrational mode. This enables a clear distinction between modes originating from intra-nanotube vibrations and those arising from inter-nanotube interactions. This decomposition is also illustrated in the left panel of Fig. 4.17. As shown, the spectrum corresponding to non-interacting modes, namely those involving atomic displacements within a single nanotube, is remarkably similar to that of the isolated CNT. Instead, new vibrational modes below 800 cm^{-1} are observed, which were absent in the isolated system and originate from the interaction arising from the coupling of the two CNTs. The vibrational modes resulting from inter-nanotube interactions, identified as those involving atomic motion in both nanotubes, are responsible for a strong contribution in the 800–1400 cm^{-1} range, along with some additional a minor peak at lower frequencies ($\sim$ 400 cm$-$1). These results indicate that low-frequency regions of the spectrum are dominated by the interaction between the CNTs. This implies that the presence of another nanotube in proximity of a first one affects significantly the vibrational modes of both, generating low-frequency modes that do not exist in isolated systems.

The distinction between interaction-driven vibrational modes and those independent of inter-nanotube interactions can be visualized at the atomic level by analyzing the corresponding eigenvectors. As illustrated in Fig. 4.18, it is possible to identify which atoms are significantly involved in a given vibrational mode by following the displacement of each atom I, $\mathbf{R}_I \pm \mathbf{e}_\omega$, along the eigenvector $\mathbf{e}_\omega$ corresponding to a given eigenvalue ω of the frequency spectrum. In this type of analysis, we selected atoms whose displacement along the eigenvector is non-negligible, based on a normalized threshold criterion. The selection is made using the formula $\frac{1}{\sqrt{3N}} - \alpha$, which corresponds to the amplitude that each of the $3N$ degrees of freedom would need to have to be equally and fully active in a given eigenmode, being N is the number of atoms in the system and α a parameter set to 10% of $\frac{1}{\sqrt{3N}}$. This allows for a systematic identification of the atoms participating in a non-negligible way to each mode. This analysis shows rather clearly the characteristic structural patterns that correspond to specific frequency domains. The intra-CNT vibrational modes, particularly in the 1200–1400 cm^{-1} range, originates from the atoms evidenced as spheres in the left upper panel of Fig. 4.18, resulting essentially in collective longitudinal oscillations along the axis of the nanotubes. At higher frequencies, specifically around 1800 cm^{-1}, similar longitudinal configurations are observed, but now involving four atomic domains as in the left lower panel of the same figure. For the inter-nanotube modes, specific structural patterns are also discernible and localized on specific spatial regions of the nanotubes. One typical case is represented by the frequencies in the 1200–1400 cm^{-1} range, featuring two longitudinal collective motions on one CNT and a radial oscillation on the adjacent one as in the right panel of Fig. 4.18. Depending on the frequency considered, various locations

locations along the CNTs can be identified as responsible for a specific vibrational mode.

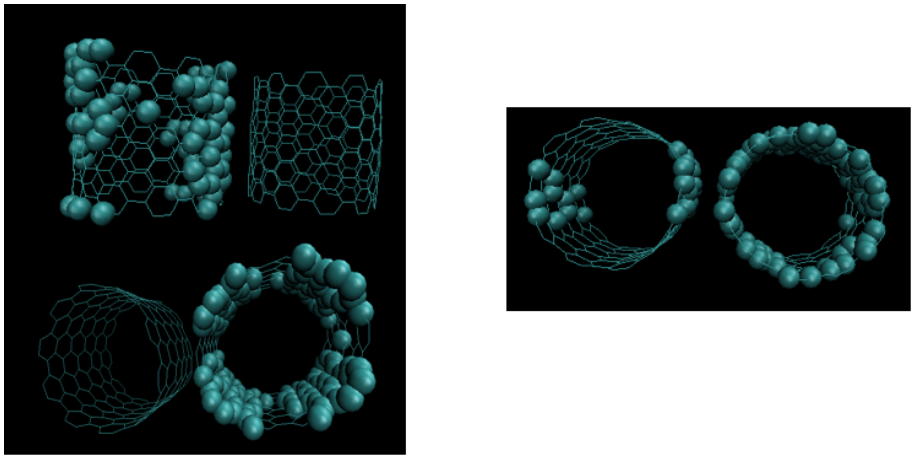

Figure 4.18. Main atoms contributing to frequencies of the vibrational spectrum generated by two coupled CNTs. The left upper and lower panels show collective modes due to groups of atoms belonging uniquely to one of the two CNTs. The right panel shows a typical vibrational mode that involves regions located simultaneously on both the CNTs. Details are discussed in the text.

As commonly done in the literature, it is possible to determine the direction of atomic displacements for each vibrational mode using the corresponding eigenvectors. This directional information, combined with appropriate selection rules, can in principle be used to identify modes that are active in Raman or IR spectroscopy. However, due to time constraints and being beyond the interest of this work, this analysis was not carried out.

The CNT/PMMA system

The vibrational analyses was done also for the composite CNT/PMMA system. To this aim, three distinct configurations were selected along the dynamically generated trajectory to study the interaction between CNT and PMMA. The first configuration corresponds to a system in which the two CNTs are interacting and the PMMA is located in close proximity, forming numerous (pseudo) H-bonds with both nanotubes. This corresponds to the maximum direct interaction identified via dynamical simulations. A second configuration of this same system consists of the two interacting CNTs in which the PMMA is more distant and forms fewer H-bonds. Hereafter, I will refer to these two systems as 'strong interaction system' and 'weak interaction system', respectively. The third configuration consists of a system characterized by a strong interaction between a single CNT and a nearby PMMA chain, whereas the second CNT is not interacting with the polymer. As noted, the size of the system significantly affects the computational cost. For this reason, the systems involving two CNTs and PMMA were reduced in the number of atoms to make the calculations affordable. Hence, the strong interaction system consists of 394 atoms, while the weak interaction system includes 383 atoms. This resizing was not applied to the single CNT–PMMA system, which is made of 518 atoms. As indicated in Table 4.2, the increase in system size directly impacts the computational time required for the vibrational analysis and, physically more important, the nature of the interactions with the PMMA determine the minimum vibrational frequancy realizable by the composite system. A noteworthy result concerns the vibrational modes realized by the three different systems. For the strongly interacting one composed of two CNTs and one PMMA chain, the minimum vibrational frequency is 29.4 cm^{-1}. In contrast, the weakly interacting system reaches a minimum of 67 cm^{-1}, while the system consisting of one CNT and one PMMA chain reaches a minimum value of 131.8 cm^{-1}. These results are in full agreement with the previous observations and corroborate the conclusion that the

	strong	weak	1 CNT 1PMMA
computation time	17h49	15h08	78h10
Minimal vibrationnal state (cm^{-1})	29.4	67	131.8

Table 4.2. Simulation times and minimum vibrational frequqncies realized by the combined CNT/PMMA systems described in the text.

presence of PMMA in proximity of a CNT surfaces significantly affects both the electronic and vibrational properties of the system. In particular, this interaction leads to a drastic reduction in the number of accessible vibrational states and in a significant shift of the low frequencies toward a few tens of cm^{-1}. This reduction can be modulated by tuning the proximity and extent of the PMMA–CNT interaction, as done, for instance, in the case of a polymer matrix hosting ensembles of CNTs. Strongly interacting polymers slow down significantly the low frequency vibrational modes of CNTs and the effect is emphasized by the amount of polymers, coverage of the CNT external surface and keeping into account that low frequencies are always the result of collective modes, as shown above, and not single interatomic oscillations as simple stretching or bending features.

We can now compute the VDOS for our systems. In the first case, namely the strongly interacting CNTs and PMMA, the result is shown in Fig. 4.19. The first remarkable observation in the total VDOS is that, unlike previous spectra where the vibrational signature of the single CNT dominated, the current spectrum shows a significant increase in the low-frequency range. While the characteristic peaks of isolated CNTs, between 1500 and 2000 cm^{-1}, and to a lesser extent between 1000 and 1500 cm^{-1}, can still be identified, the low-frequency domain now contains many new vibrational modes.

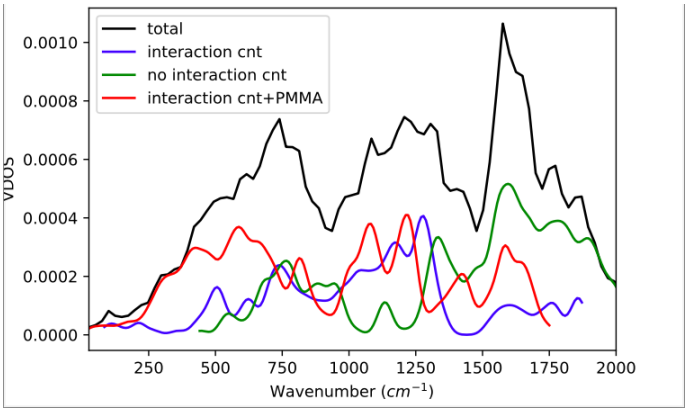

Figure 4.19. Vibrational density of states (VDOS) for the three systems discussed in the text. The blak line is the total contribution of the system composed by CNTs and PMMA. The analysis of the eigenvectors allowed to disentangle different contributions and to identify which atoms are contributing. Hence, the blue curve shows the contribution of interacting CNTs, the green curve the one of non interacting parts of the CNTs and the red one the effect of the CNT–PMMA interaction. Here the enhancement in the range below 250 cm^{-1} is evident.

By decomposing the contributions using the eigenvectors of the dynamical matrix, we can identify the vibrational modes involving atoms from both CNTs, and those involving atoms from CNTs and the PMMA. This analysis reveals that the low-frequency region is now dominated by vibrational modes arising from both CNTs and the PMMA, which are interacting. In contrast, the high-frequency region is primarily composed of modes localized within a single CNT. In the mid-frequency range, a mix of interaction modes is observed, some involving only the CNTs, and others involving both the CNTs and the PMMA.

By examining the vibrational spectrum of the CNT-PMMA system with weak interactions, we can observe that the overall shape of the spectrum remains similar to the strongly interacting case. However, when focusing on the interaction spectrum, the vibrational modes involving atoms belonging both the CNT and the PMMA, we notice a significant decrease in intensity compared to the previous case. This has several consequences. First, the number of low-frequency modes is reduced compared to the strongly interacting system. Second, in the mid-frequency range (between 1000 and 1500 cm^{-1}), the dominant contributions come from CNT–CNT interactions, meaning that the vibrational modes involve atoms from both CNTs. The net effect is an increased spectral intensity in this frequency range. In the case of a single CNT interacting with a PMMA chain, the influence of the PMMA becomes more pronounced. The vibrational spectrum shifts toward higher frequencies, with notable peaks around 1200 cm^{-1} and 1600 cm^{-1}, while still retaining features characteristic of CNT–PMMA interactions in the lower frequency range (200–2000 cm^{-1}). These results highlight the effect of PMMA on the composite system, as well as

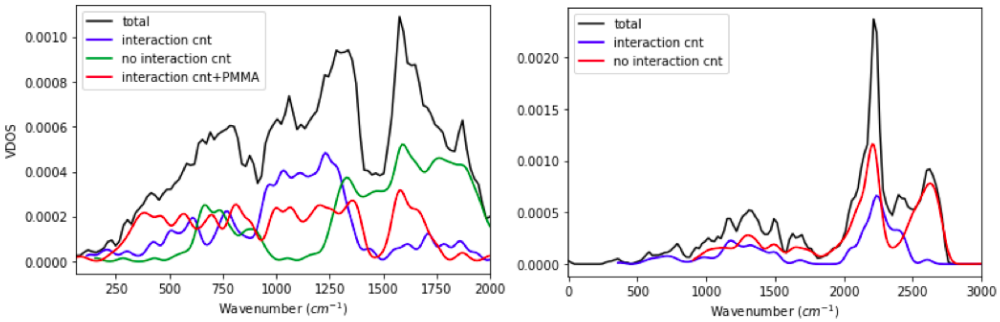

Figure 4.20. Comparison of the spectra obtained for CNTs interacting with the PMMA polymer (left panel) and the one obtained in the case of CNTs only (right panel). The same analysis of the atoms involved in the various contribution done in the case of the former figure has been done also here, resulting in the colored lines whose details are given in the legend provided as inset in the two panels.

the possibility of modulating the dielectric response through experimentally tunable parameters, such as the volumetric density of PMMA or the density of carbon nanotubes. It is particularly relevant to put these findings into perspective with those obtained previously. Indeed, in this last section, we observed that two interacting CNTs can give rise to vibrational modes down to 226 cm^{-1}, a value previously reported in Section 4.2.1 where, we have shown in Fig. 4.9 that the interaction between two CNTs is responsible for bond length fluctuations at frequencies around 216.6 cm^{-1}. Furthermore, in the same figure, I have shown that systems composed of two CNTs and PMMA significantly increase the low-frequency contributions of these same bond relaxation phenomena. This is a trend we once again observe in the current analysis, where numerous low-frequency vibrational modes emerge as a result of interactions between two CNTs in close contact with PMMA as one would expect in a polymer matrix hosting nanotubes.

4.4 Conclusions

Summarizing, the use of FPMD combined with the dynamical matrix methodology enables a comprehensive multi-scale analysis of the phenomena governing interactions within the studied systems. The generation of an equilibrated dynamical trajectory is always a necessary step to produce configurations and polymer conformational changes suitable for subsequent studies. Structural deformations were characterized, followed by an investigation of interatomic distortions through bond analysis. This approach provides valuable

insight into the evolution of electronic structure and its modifications induced by the presence of new interactions. We were able to highlight the presence of characteristic phenomena, both in terms of magnitude and frequency scale, with the study of molecular ovalization that are characterized by frequencies in the microwave range. This would ot be accessible without a dynamical approach. Furthermore, the absorption spectrum we obtained demonstrated that the interaction between two CNTs and, more broadly, the interactions present systems composed of molecular building blocks tend to lower the absorption frequencies of the system as a whole. On a strictly technical standpoints, I wish to stress the fact that even with the most advanced high-performance computing architectures currently available, the calculation of absorption spectra have still difficulties, within a reasonable computational time, in reaching the microwave frequency range via purely dynamical approaches. A possible workaround, with all the size limitations discussed in this chapter, consists in perturbative approaches such as the dynamical matrix method. This approach provides a precise identification of the atoms involved in vibrational modes and allows to disentangle the various contributions. However, this method inherently sacrifices both the multiscale perspective and the dynamic information captured by time-resolved simulations. Moreover, we also needed to scale down the number of atoms to reach tractable system sizes. In a sense, if the first principles molecular dynamics is time consuming, perturbative methods are memory consuming in terms of computational resources.

I wish to emphasize also the fact that the approach we used revealed that interactions within the system lead to structural modifications and a slowing down of vibrational modes, resulting in characteristic modes at frequencies approaching the microwave regime. The dynamical matrix method is not capable of describing certain periodic modes. In particular, the modes associated with structural ovalization, which were shown to lie within the microwave frequency range and emerge from the dynamic behavior of the system; these are not captured by static approaches and perturbative methods because they involve long range and time evolving movement of all the atoms at once. It is therefore essential, when employing a specific method, to carefully select systems for which that method allows to extract the maximum amount of information. This should be accompanied by a beforehand analysis of the targeted energy, frequency or time span to be achieved. In our specific case, a careful coupling of FPMD and perturbative methods could enable a broader spectral analysis and a deeper understanding of the underlying physical phenomena that would escape the attention if only one of the two methods is used. This combined methodology leverages the strengths of both static and dynamic approaches, offering complementary insights into the vibrational behavior and interaction mechanisms in complex systems.

Chapter 5

Graphene and reduced graphene oxide systems

Summary

In this chapter, we did some exploratory calculations, within the same methodologies and protocols developed in the former chapters, toward bidimensional carbon-based materials instead of CNTs. This new direction was proposed and inspired by our experimental coworker as a viable alternative to CNTs-based composite systems in the search for materials easy to synthesize and control for the same microwave applications targeted all along this project. As done in so far in this doctoral project, we did all possible effort to extract the maximum amount of information and to identify limitations inherent to the simulation approaches, extending and implementing new tools capable of describing systems with topologies different from those of CNTs. The first two-dimensional carbon-based system is clearly graphene, a system intensively studied over the years. On a strictly electronic standpoint, summarizing all the results published to date, graphene is a semimetal in which the electrical conductivity is rather high and ensured by both electrons and holes carriers. Electronic properties of graphene result from the interplay between bonding and anti-bonding of delocalized π orbitals. An interesting feature of graphene electronic structure is the presence of Dirac points, consisting in a local zeroing of the bad gap in which the effective mass of electrons and holes becomes equal to zero. This occurs because of the symmetry of the graphene lattice makes the spectrum linear at low energies near the 6 individual corners of the Brillouin zone, where the so-called Dirac points are realized. Actually, because of the zero density of states at the Dirac points, the conductivity is expected to be quite low. Yet, the Fermi level can be tuned by doping (with electrons and/or holes) leading to an increase more or less controllable of the intrinsic electric conductivity. Nonetheless, this does not provide any insight nor hint about the behavior of a pristine (or doped) graphene systems in the microwave range, nor response to incoming electromagnetic signals can be easily extracted from these electronic structure data. An additional complication comes from the size of the graphene sheet, which can influence the vibrational spectrum, particularly at low frequencies, depending on the rippling and long oscillations that the size of the graphene sheet can allow.

For the reasons briefly outlined here, topological studies of graphene are crucial for investigating phenomena such as finite size effects, substitutional defects, and atom vacancies within the structure. In particular, defective graphene seems to be a promising material since upon reduction of *ad hoc* functionalization a response in a specific frequency range could be enhanced or suppressed. These possibilities represent a perspective for graphene engineering and, in this respect, the present chapter provides a first attempt to push atomistic modeling toward this new direction. I started my study focusing on different pristine graphene systems, in an attempt at identifying the most suitable systems for simulation

of defects and reduction, consistently with the experimental indications. Subsequently, I studied two particular systems commonly found in reduced graphene oxide (rGO). The first consists in the substitution of two neighboring carbon atoms by oxygen atoms, thus not affecting the overall number of atoms, but the local chemical composition. The second consists of a graphene sheet carrying a C vacancy and in which two of the three adjacent C atoms on the border of the vacancy are replaced by O atoms. For these systems, I investigated structural, electronic and vibrational properties as plausible template for the applications sought in my research project.
I wish to bring to the attention of the readers of my manuscript that these investigations were conducted during the final stage of my Ph. D. thesis, which limited the time I could dedicate to extended simulations and deeper investigations on graphene=based systems, with the word "time" to be intended as the number of hours I could dedicate to the calculations and available HPC hours on our grants.

5.1 Graphene

5.1.1 Size effects of graphene sheets

As reiterated all along this thesis, first principles approaches pose well known limitations in terms of tractable system sizes. A direct consequence is the fact that the finite size of the simulation cell can introduce artifacts more or less important that, in turn, influence the behavior with respect to a large or virtually infinite sheet. These finite-size effects can become particularly relevant in systems with defects, substitutions, or local deformations, thus influencing the computed properties such as charge distribution, or vibrational modes. Understanding and carefully accounting for these effects is thus essential to ensure meaningful and transferable insights from first principles simulations of graphene and its functionalized forms toward real systems. With this warning in mind, I shall then proceed to the details of my simulation approach and the results obtained on these bidimensional structures.

Simulation Protocol

To probe potential size effects in our graphene systems, I performed a comparative study of two model systems. The first one consists of a graphene network composed of 190 atoms, while the second one was extended to 378 atoms. The simulations of both systems started following the same protocol described in Section 3.2.2. Since the relaxation of a periodically repeated graphene system is relatively smooth, the NVE phase was carried out for just 5 ps, followed by a 15 ps NVT phase. For the system containing 190 atoms, the simulation cell dimensions are $21.14 \times 23.39 \times 7.94$ Å^3. These values ensure good separation from the

repeated images along z and the periodicity on the (x, y) plane since periodic boundary conditions are applied. Analogously, for the graphene system of 378 atoms, the simulation box is $29.66 \times 33.23 \times 7.94$ Å^3. These two systems are shown in Fig. 5.1. Consistently

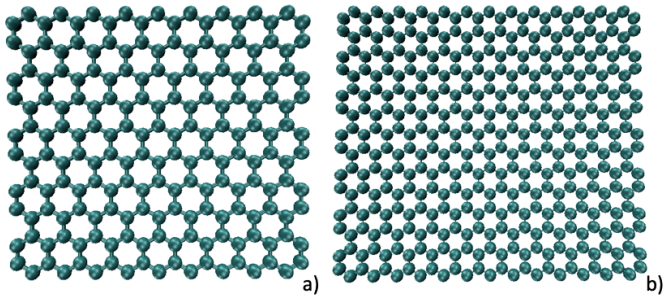

Figure 5.1. Equilibrium configurations of the simulated graphene systems of 190 C atoms (a) and 378 C atoms (b).

with the computational set-up discussed in Section 4.1.3, the BLYP correlation functional is used to describe the exchange and correlation interactions, complemented by the van der Waals interactions within the maximally localized Wannier functions implementation. Since carbon-based materials do not exhibit notable spin-dependent behavior, we chose to perform our calculations in a spin-restricted approach. Norm-conserving numerical pseudo-potential of the Troullier-Martins type were used for the description of the core-valence interactions. Electronic wavefunctions are expanded on a PW basis set with a cutoff energy of 80 Ry (1088.5 eV) with the sampling of the Brillouin zone restricted to the Γ point in view of the relatively large sizes of the sheets (hence including more than a single **k**-point). For the dynamics, te numerical integration of the Car-Parrinello equations of motion was done with a the numerical integration of 5 a. u. (0.121 fs) and a fictitious electron mass of 800 a. u. . In all canonical NVT simulations the temperature was controlled by a Nosé-Hoover thermostat chain.

System topology and characteristics

My first task in dealing with these graphene systems was to identify which topological features could be influenced by the size of the model. To this aim, as illustrated in Fig. 5.2, I monitored the rippling and out-of-plane deformations induced by the temperature during canonical NVT simulations. These thermally induced ripples seem indeed to be affected by system size, particularly because the simulation box is limited and does not allow oscillation lengths longer than the box size. As a result, long-wavelength fluctuations may be artificially suppressed in systems which are too small. The edges play then a central role in these features and must always be kept into account before comparing to experimental systems. This finite size effect can also lead to local tensile or compressive stresses, which are expected to have an impact more evident on smaller systems with respect to larger ones.

This out-of-plane rippling motion observed depends on the system size, in the sense mentioned above. More precisely, in the 190-atom graphene system, the deformation pattern remains relatively simple, often characterized by a dominant single ripple, as shown in the left panel of Fig. 5.2 where the corresponding contour color map shows a major deformation pattern. For the 378-atom graphene system, the deformations observed are clearly more complex, resulting in a superposition of multiple ripples of varying wavelengths and amplitudes, leading to a more intricate and heterogeneous structural response. While this visualization is useful to monitor deformations within the graphene structure, it remains difficult at this stage to determine whether these are primarily driven by the system size or by the influence of periodic boundary conditions.

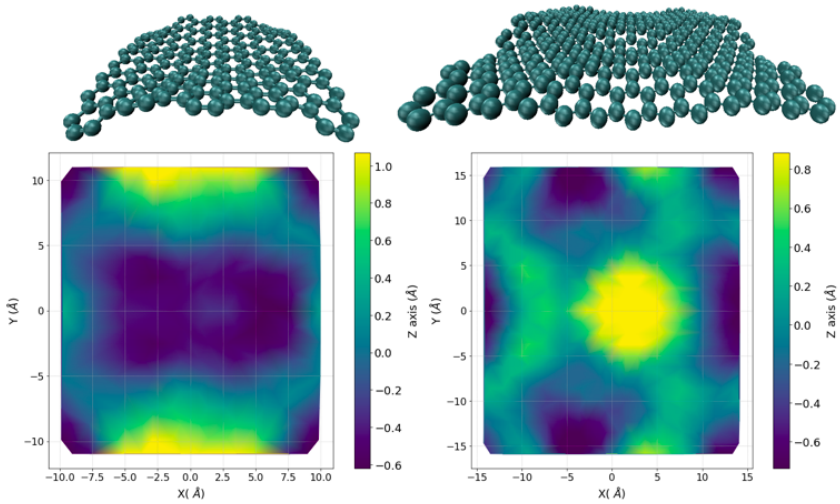

Figure 5.2. Conformations assumed by the two simulated graphene systems during the canonical NVT simulations. The contour color maps indicate the scale corresponding to the height (z-axis) of the structure and the scale from negative (blue) to positive (yellow) is reported on the right in both panels. The left panel refers to the 190 atoms system while the right panel to the 378 atoms sheet. Both graphene layers are reported as snapshots on top of the two panels.

A helpful parameter to quantify the deformation of a planar surface is its rigidity. To this aim, assessing the rigidity of a system translates into a characterization of its ability to undergo deformation. Hence, I computed the Gauss curvature maps of the two systems. This can be done by performing a quadratic fitting of the graphene surface by the bidimensional function

$$f(x, y) = ax^2 + by^2 + cxy + dx + ey + f \tag{5.1}$$

This fit is performed using the Delaunay triangulation method on each atom up to its 10th neighbors. To verify the effectiveness of this method and to ensure that it does not yield meaningless results, I calculated, for each atom, the coefficient of determination R^2, plotted in the histogram of Fig. 5.3, which provides a direct measure between the fitted quadratic surface and the actual atomic positions. The fact that the observed values are consistently close to 1, the mean value over all atoms $\bar{R}^2 = 0.96$, indicates that the fits are of high accuracy. From this fitted surface equation, the Gaussian curvature $K(x, y)$ is

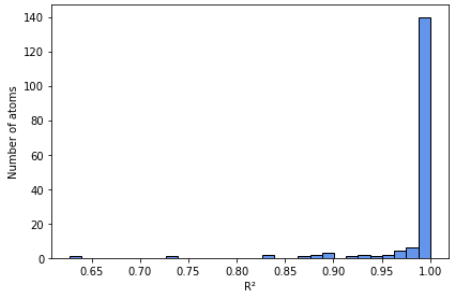

Figure 5.3. Histogram of the coefficient of determination R^2, as detailed in the text, providing an estimation of the difference between the quadratic surface fit and the actual atomic positions for the 190-atom system.

computed at each (x, y) coordinate of the domain, indicating the position of each atom in the graphene network. This surface curvature is then represented by a quadratic function

as

$$K(x,y) = \frac{4 \times ab - c^2}{(1 + d^2 + e^2)^2} \tag{5.2}$$

The results are graphically shown in Fig. 5.4 for the two graphene systems. As observed,

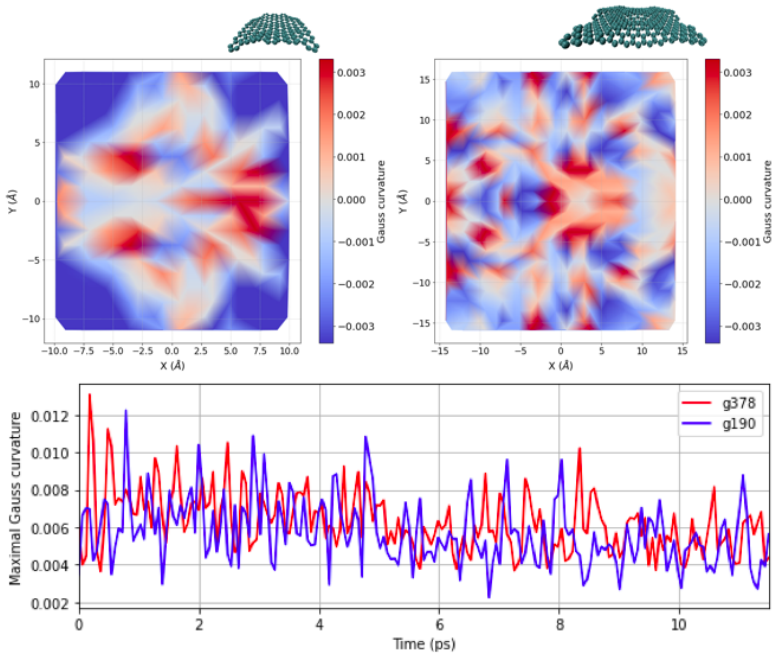

Figure 5.4. The two panels on the top show the contour color maps of the Gaussian curvature (see text for details) as a function of the position in the graphene sheets for the 90-atom system (on the left) and the 378-atom one (on the right). The bottom figure shows the time evolution profile of the mean value of the norm of the maximal curvatures during the dynamics.

the variations within the 378-atom system are more elaborated in comparison with those realized in the 190-atom system. This remains true also for the central regions (where periodic conditions at the border should be less stringent) in an area of about ± 10 Å in both x and y directions. While the central motif of the `g378` system can be compared to that of the `g190` system, its interpretation is not trivial.
The Gaussian curvature at a given point is defined as the product of the principal curvatures at that same point, expressed as

$$K(x,y) = \kappa_{\min}(x,y) \cdot \kappa_{\max}(x,y) \tag{5.3}$$

where $\kappa_{\min}$ and $\kappa_{\max}$ are the minimal and maximal principal curvatures, respectively. A negative value indicates that these two curvatures have opposite signs, corresponding to a saddle point. A positive value means that both principal curvatures have the same sign, namely, the surface is elliptical and can have either a convex or a concave shape. This parameter provides a useful quantification of the deformations occurring in our system and complements the data presented in Fig. 5.2. We observe that the zones of extreme deformation are more localized in the `g378` system. In contrast, for the `g190` one, significant deformations appear at the corners of the simulation cell, where the stress due to the finite box size is more pronounced, hence being a potential source of undesired distortion effects. This is supported by the observation of the average of the maximal Gaussian curvature trend shown in the lower panel of Fig. 5.4. In fact, the average combined curvature is higher for the `g378` system, with a numerical value of

$$\overline{K^{378}_{\max+\min}} = 0.0063$$

compared to

$$\overline{K^{190}_{\max+\min}} = 0.0057$$

for the `g190` system.

However, when considering the average of the absolute Gaussian curvature values, we find

$$\overline{|K^{378}|} = 0.0019$$

versus

$$\overline{|K^{190}|} = 0.0023.$$

indicating that the two are roughly equivalent. We can infer that, although the `g378` system exhibits higher peak curvatures, the `g190` system is more uniformly curved across its whole surface, suggesting that the `g190` system experiences additional strain throughout its structure.

As a final investigation aimed at quantifying the observed behavior of the two systems, I focused on the temporal behavior of the observed out-of-plane ripples. To this aim, I applied a Fourier transform to the time series data provided by the molecular dynamics simulations to extract the characteristic frequencies associated with these deformations and to get a deeper insight into their evolution over time. Although tracking the displacement of a single atom over time can provide useful insights, such information is still incomplete to fully characterize collective vibrational modes. Therefore, I selected all atoms lying at a fixed y-coordinate, specifically $y = 0$, for both the 190-atom and 378-atom graphene systems. On these groups of atoms, a Fourier transform was performed on the trajectories generated by FPMD. The resulting spectra were subsequently convoluted into a single comprehensive plot and the result is the one presented in Fig. 5.5.

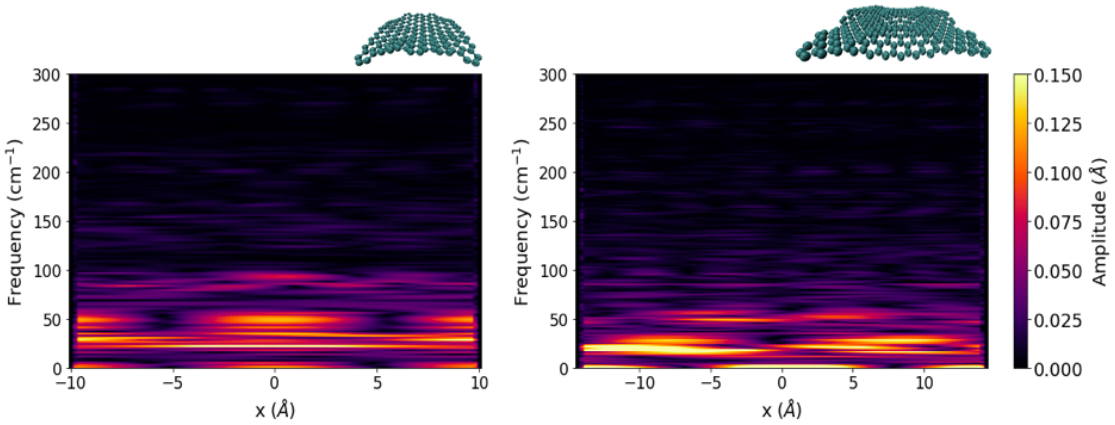

Figure 5.5. Result of the Fourier transforms of the set of atoms at $y = 0$ as explained in the text. The left panel shows the spectrum of the 190-atom system and the right right one the analogous spectrum for the 378-atom system.

These bidimensional plots show rather clearly the nodes in the out-of-plane undulations of the system, thereby allowing us to identify the waveforms and determine the corresponding frequency range involved. We can conclude that, at very low frequencies, namely between 6 and 7.3 cm^{-1}, a second harmonic wave arises, characterized by the presence of nodes at positions around $\pm 0.25\ \text{L}_x$, for a wavelength of L_x in both systems. Furthermore, in the frequency range between 20 and 35 cm^{-1}, we can identify a first harmonic wave. In the case of the 190-atom system, this mode is marked by minima at the boundaries of the system's length. And for the 378-atom system it is the maxima at the boundaries. What is particularly noteworthy is that, at higher frequencies, while the 190-atom system allows for clearer identification of individual vibrational modes, the

378-atom one exhibits discernible higher-order harmonics, observable up to frequencies of about 250 cm^{-1}.

Summarizing, this section has provided evidence for a significant influence of system size on the physical phenomena responsible for the behavior of the simulated model both in terms of topological deformation and spectral response. While the phenomena of interest are reproduced in both models, we clearly observe a loss of information in the smaller system, primarily due to size-related limitations. For instance, edge-related artifacts, revealed through the analysis of Gaussian curvature, are more pronounced in the smaller system, along with a reduction in mechanical rigidity.

Moreover, the Fourier transform analysis highlights a loss of spectral information in the frequency range between 100 and 200 cm^{-1} for the smaller system (g190). This loss has also consequences in the lower frequencies part of the spectrum, where distinct vibrational regimes are clearly identifiable in the g378 system, but remain ambiguous, thus difficult to unravel, in the g190 case. For these reasons, we will proceed with the larger 378-atom graphene system in the remainder of our study, despite the increased computational workload that this implies. This choice will ensure a more reliable analysis of the vibrational and structural dynamics of our systems.

5.1.2 Graphene Nanoplatelets

In our modeling protocol, consistently with the rich literature on the subject, we made use of a somehow ideal graphene systems, specifically monolayer graphene consisting of a single atomic layer. As mentioned at the beginning of this chapter and in the general introduction of Chapter 1, this two-dimensional carbon-based material has been intensively targeted because of its exceptional mechanical, electrical, and thermal properties. However, in laboratory realizations and industrial applications, where large-scale implementations are sought, graphene-based nanocomposites are typically not fabricated using isolated 2D graphene sheets. Instead, they are made with stacks of graphene layers, commonly referred to as graphene Nanoplatelet (GNP), although recently graphene monolayers seem to be potentially obtained by thermal treatments [121–123]. GNPs consist of multilayer graphene, typically including a variable number of layers from 5 to 100 layers,depending on the synthesis conditions, this resulting in thicknesses ranging from approximately 1.5 to 30 nm [124]. Even in the case of actual graphene monolayers, they are obtained on solid bulk substrates, such as SiC. This poses and additional challenge to our simulations, because it means that these graphene sheets are not free to float and ripple, but are anchored to a rigid support that limits the deformation and fluctuations accessible to a graphene system at finite temperature. We had, then, to look for a way to mimic the presence of such a constraint without adding excessive burden to the simulations.

Modeling the Effect of a Substrate

A key challenge in simulating more realistic graphene-based systems lies in reproducing the limited movement that an increased thickness, as in a GNP, or a substrate, as in SIC grown graphene, induce on a graphene sheet or nanoflake. Adding explicit layers of graphene or a whole bulk substrate is computationally demanding and beyond the reach of my doctoral project. Therefore, to emulate the presence of additional graphene layers by keeping the computational complexity affordable, we chose to modify the potential experienced by atoms within the monolayer adding some restrains to our single graphene sheet as done, for instance, in the case of catalytic nanographene [125]. To avoid overconstraining the degrees of freedom of the simulated graphene sheet, we imposed the restraint potential to four distinct regions in the simulation cell, defined by the (x, y) coordinates (a, a), $(a, -a)$, $(-a, a)$, and $(-a, -a)$ as sketched in Fig 5.7.

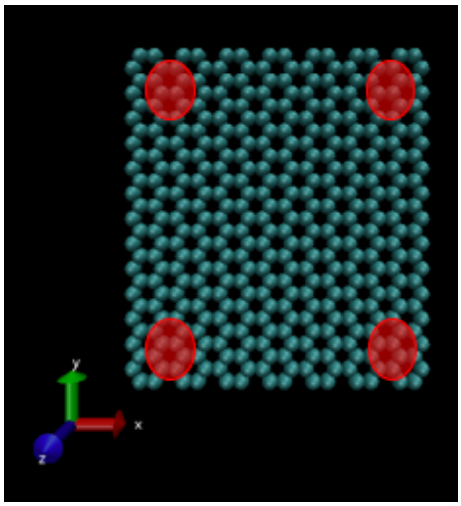

Figure 5.6. Representation of the graphene system with 378 carbon atoms with the harmonic potential restraint regions highlighted by the red circles. This limits the oscillations of the whole system acting as a virtual substrate to which the modeled graphene sheet is bound.

Within these regions, atoms were subjected to a harmonic potential of the form:

$$V(\mathbf{r}) = \frac{1}{2}k(\mathbf{r}(t) - \mathbf{r}_0)^2 \tag{5.4}$$

where $\mathbf{r}(t) = (x, y, z)$ indicates the instantaneous atomic position along the dynamics, whereas $\mathbf{r}_0 = (x_0, y_0, z_0)$ represents the reference crystallographic position of the same C atom at the equilibrium. The parameter k is the force constant of the harmonic potential, which we calibrated based on values reported in the literature [126]. In these studies, interlayer interactions as in GNPs were modeled using a Lennard-Jones potential, allowing to provide a rough estimation of the interlayer cohesive energy E_{coh}, in our specific case ranging from 20 to 50 meV, indicating that a separation of approximately 7 Å between two adjacent layers is required to overcome this interaction and set a graphene sheet free. From these data, we estimated the force constant as $k = \frac{2.E_{coh}}{{z_{escape}}^2}$, taking into account that the equilibrium distance between graphite layers is 3.35 Å, a good approximation for k is 0.0035 Ha.${a_0}^{-2}$ in atomic units.

It is evident that, aside from the restrained potential applied to a subset of atoms, the current system is structurally identical to the one simulated and analyzed in the previous section. Consequently, the simulation protocol and parameters remain unchanged and are those described there. Specifically, the simulations consist of a 5 ps NVE phase followed by a 12 ps NVT phase.

System topology

From a topological standpoint, the presence of constrained atoms in the system results in anchoring points in which the excursions of the atoms way from the crystallographic positions are limited, imposing nodal conditions at their locations. While this limits the displacement of the restrained atoms, it also induces a broad region of deformation in the central part of the system. This is particularly evident when analyzing the system's curvature with the Gaussian curvature method introduced in the former section: the peak curvatures observed in the restrained system are significantly higher than those in the unconstrained identical system. As expected, the major effect occurs in the vicinity of the constrained zones. Quantitatively, the maximum average curvature reached during the dynamical run in the NVT canonical ensemble is $\overline{K^{rest}_{max+min}} = 0.0070$ in the restrained case, compared to only $\overline{K^{g378}_{max+min}} = 0.0063$ for the unrestrained system.

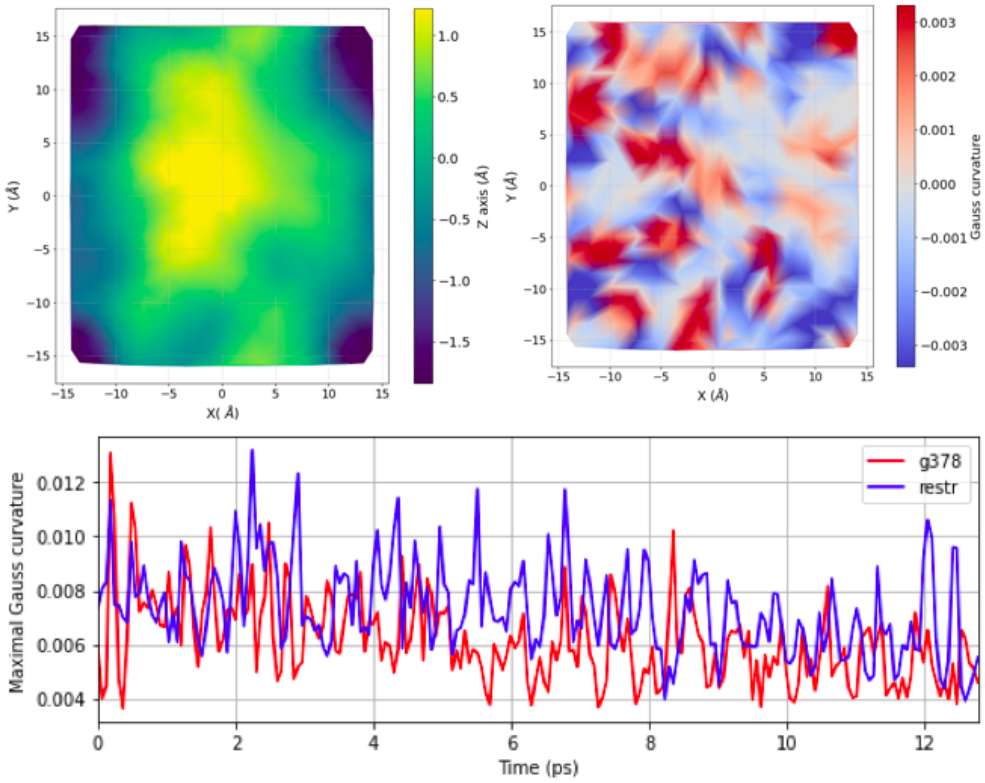

Figure 5.7. Topology of the restrained graphene. Top left panel: Contour color map relative to the atomic displacements along the z-axis (height). Top right panel: Contour color map showing the Gaussian curvature of the system. Bottom panel: Evolution of the average between the maximal Gaussian curvature and the norm of the minimal Gaussian curvature over time, shown in red for the unrestrained graphene and in blue for the restrained graphene.

However, since we are considering the mean curvature over the entire system $\overline{|K^{rest}|} = 0.0020$, its value remains numerically identical to that of the unconstrained configuration $\overline{|K^{g378}|} = 0.0019$. This indicates that while localized regions exhibit stronger curvature due to the atomic constraints introduced, the curvature over the rest of the system remains essentially unchanged. Therefore, the imposed restraints lead to a redistribution rather than an increase in the total deformation. On one hand, this is informative of the fact that we are indeed mimicking the presence of a support on which our graphene sheet is interacting. On the othe hand, it ensures that we are not biasing excessively the system with artifacts that could possibly invalidate the simulations. This interpretation is further supported by the Fourier transform analysis performed on all atoms with a fixed y-coordinate, as done above. This analysis shows that a dominant spectral component at 15 cm^{-1} arises, mainly localized in the central region of the system, with nodal points appear at the edges, as anticipated by the introduction of the restraints. Beside this dominant frequency, secondary components are reduced with respect to analogous contribution in the case of the unconstrained system, indicating a reorganization of the deformation modes rather than an increase in vibrational complexity. To corroborate these observations, I computed the relative mean square displacement (RMSD) of the atoms of both the free and restrained systems, along with the difference between the two datasets. The results of this analysis are summarized in Fig. 5.8.

The analysis reveals that atoms located near the boundaries and in the vicinity of the restrained regions exhibit reduced mobility. which is clearly expected. Conversely, the central region of the system shows an increase in atomic displacements, indicating that the restraints acting at specific locations lead to a redistribution of the system's dynamic

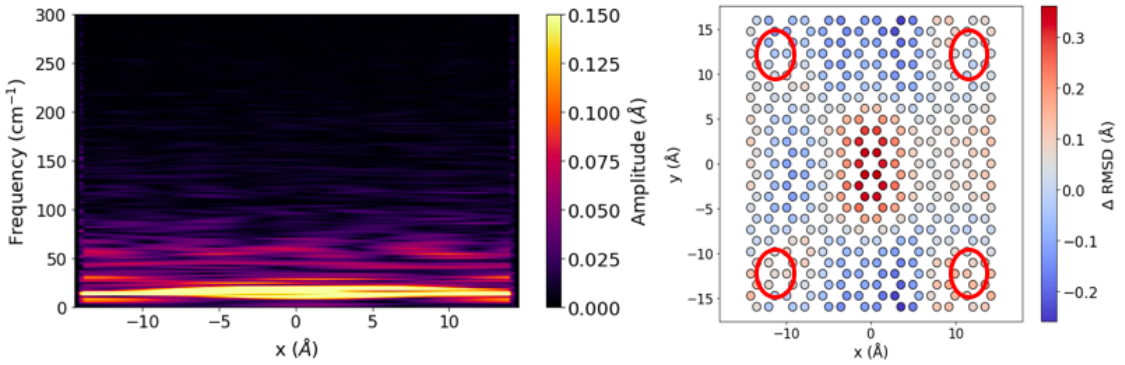

Figure 5.8. Left panel: Fourier transform, from the time to the frequency domain, of each atom of the graphene sheet at $y = 0$. Right panel: Relative mean square displacement, i.e., the difference in the mean squared displacement averaged over the dynamical simulation between the restrained and unrestrained graphene, presented as a color map.

behavior, rather than an abrupt suppression of motion.

Vibrational analysis

For the vibrational study, the computational protocol follows the one described in the preceding chapter. Specifically, the system is initialized by electronic wavefunctions optimization and annealing, followed by an microcanonical NVE dynamics, lasted for 5 ps, to assess the stability. In this case, rather than proceeding to an NVT canonical dynamics, the geometry is directly re-optimized after this NVE phase to bring the system to its local minimum in view of the finite difference analysis. Then the vibrational modes are calculated from the Hessian of the system in standard way.
This methodology was applied to both the constrained and unconstrained 378-carbon graphene systems. The results obtained are summarized by the vibrational spectra presented in Fig. 5.9. The first observation we can do is that the vibrational modes of the system remain essentially unaffected by the introduction of the restraints, the two curves featuring essentially the same peaks and pattern. When comparing this result to the vibrational modes of CNT-based systems discussed in the previous chapter, it becomes evident that the spectral region above 800 cm^{-1} is also identical to that of CNTs.
This suggests that the high-frequency modes (above 800 cm^{-1}) are primarily associated with intrinsic C–C interactions and the characteristic (unperturbed) honeycomb lattice, common to both graphene and CNT structures. An interesting point of comparison is the lowest vibrational mode for the unconstrained graphene system, located at ~ 152.3 cm^{-1}, while for the restrained system it shifts to ~ 272.2 cm^{-1}. Despite some differences due to system size and computational set-up, these results are consistent with those reported in the literature[127]. For instance, as shown by B.G. Johnson and coworkers in the reference quote above, the average absolute deviation for vibrational modes obtained from FPMD simulations using a BLYP functional is approximately 73 cm^{-1}.

5.2 Reduced graphene oxide

As outlined in Chapter 1, it is possible to overcome limitations in the electromagnetic response, challenges posed by aggregation and difficulties of incorporating graphene into polymer matrices by using graphene oxide (GO) instead of a pristine pure graphene structure. Graphene oxide offers the significant advantage of being highly water-soluble, thus allowing for single-layer production in solution. However, GO, consisting of a single atomic layer of graphene functionalized with oxygen-containing groups such as hydroxyl, epoxide,

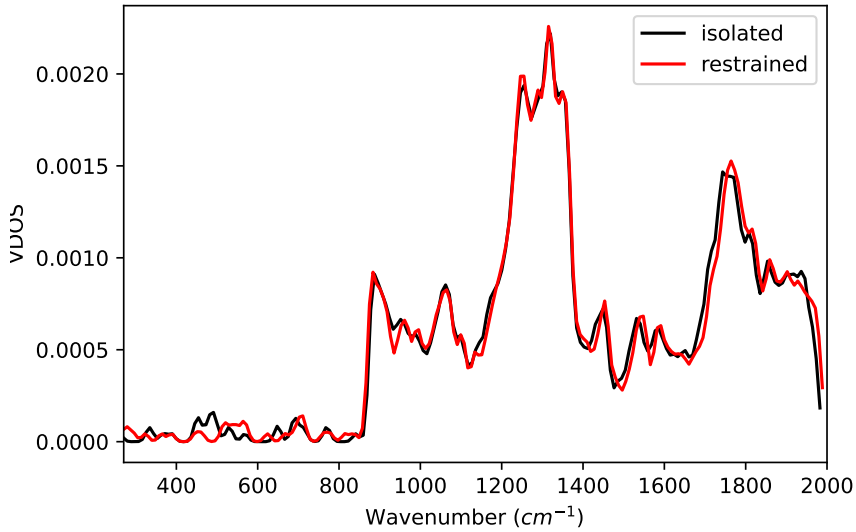

Figure 5.9. Vibrational density of states (VDOS) spectra of the two graphene systems studied. The black curve refers to the free system, while the red one to the same graphene system on whcih the restraint discussed in the text are applied.

and carboxyl, exhibits a pronounced out-of-plane structure due to these functionalizations, due to the formation of sp^3 carbon atoms. To restore a more planar, sp^2-hybridized carbon network, GO is typically reduced to form rGO. This reduction process removes a large proportion of the oxygen-containing functional groups and results in a structure that either retains defects in the form of vacancies or incorporates O atoms replacing some C atoms in the graphene lattice. The systems targeted here have been selected because they are expected to be the dominant one in a graphene sheet or nanoflake. These are shown in Fig. 5.10 and correspond to two typical cases. In the first one, two adjacent C atoms are substituted by O atoms, thus disrupting (locally) the aromaticity of the carbon rings. In the second one, a C vacancy is present amd two C atoms at the border of this vacancy are replaced ny O atoms.

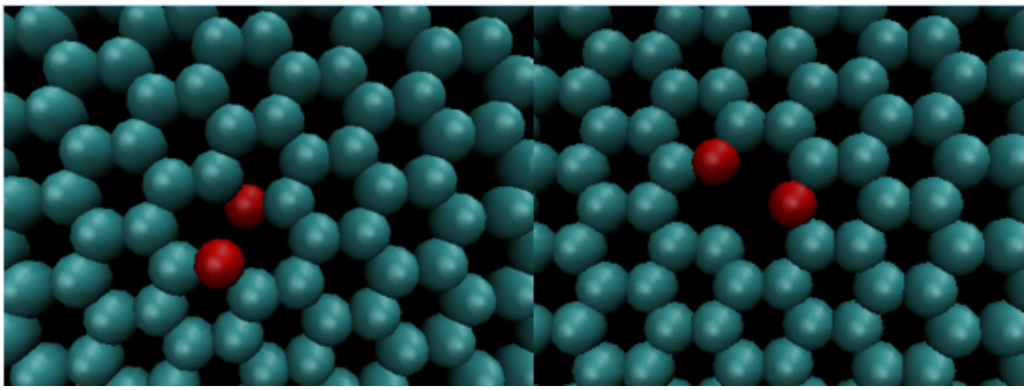

Figure 5.10. Atomic structure of the two type of defects studied in the simulated reduced graphene. The left panel shows two oxygen atoms (in red) substituting two C atoms. As a consequence, one of the two O atoms exits from the plane of the figure (the one less hidden by its neighbors in this figure) and the other one goes slightly below the plane of the figure, resulting partially hidden by its neighbor C atoms in this sketch. The panel on the right shows a C vacancy in which two C atoms are replaced by O atoms at the borders of the empty space left by the removed C.

In the second system, also based on our 378-atom graphene sheet, one carbon atom

is removed, thus creating a C vacancy, and two others at the border of this vacancy are substituted by O atoms in the same figure. These two systems will hereafter be referred to as C376O2 and C375O2 respectively, corresponding to the number of atoms present in their respective structures.
The simulation protocol was therefore slightly changed with respect to what was done for the previous systems. While prior calculations included an NVT phase, here we limit the procedure to the NVE micricanonical dynamics and optimization stages. During the NVE phase, the system was allowed to evolve for a total of 10 ps. With the HPC resources accessible to this project, such a simulation required 3.5 s/step to be executed. The parameters used to integrate numerically the equations of motion and any other additional numerical information were kept identical to those previously described in this chapter. This approach allows for the study of low-temperature dynamics and serves as a template for the subsequent vibrational analysis to be conducted on the system.

5.2.1 Effects of Carbon-to-Oxygen Substitution in Graphene

The first case of reduced graphene system considered is the one shown in the left panel of Fig. 5.10 in which two O atoms replace two C sites. These substitutions disrupt the carbon lattice and introduce topological and chemical changes. These changes are responsible for the geometrical modifications summarized in Fig. 5.11, highlighting the behavior resulting from the introduction of O atoms that, unwilling to form an O–O chemical bond because of the electrostatic repulsion between the adjacent two-fold O atoms, already involved in C-O-C chemical bonds around the vacancy. This means that only O lone-pair electrons are still available around the O sites and these are unfit to generate 3-fold O sites. Thus, the Coulomb repulsion pushes the two O atoms out of the graphene plane, with both oxygen atoms protruding out of it, one above the plane and the other below, realizing the only possible topology able to minimize such a repulsive interaction. This arrangement with

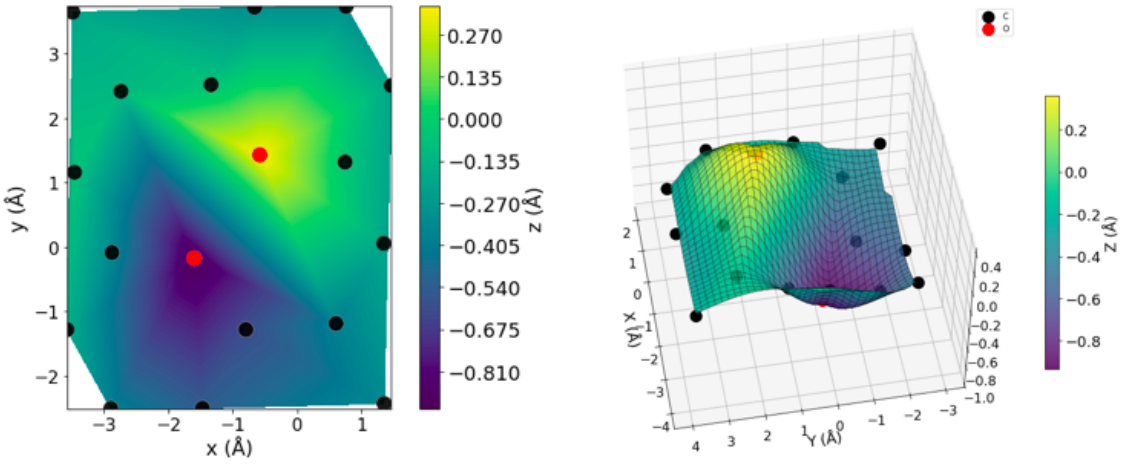

Figure 5.11. Topology of the C376O2 system. **Left**: 2D projection with a color contour map representing the out-of-plane height (z-axis) of the atoms. **Right**: 3D structure of the same topology. C atoms are shown in black and O atoms in red.

O atoms going out of the graphene plane while keeping two C–O bonds is consistent with the electronic structure of oxygen, which realizes two chemical bonds with two of its six valence electrons and two lone pairs with the other four valence states as, for instance, in a H_2O water molecule.. The lone pairs on each O would faces that of its neighboring oxygen atom, resulting in the large electron–electron repulsion mentioned above that pushes out of plane and in opposite directions the two O sites.

Beside the evident out-of-plane deformation occurring during the dynamics, the next issue is the consequences that this repulsion and structural deformation induce on the surrounding lattice. To address it, we examined the evolution of bond angles and bond lengths as a function of the simulation time. To this aim, all relevant angles and bonds in the region of interest have been labeled as in the left panel of Fig. 5.12. The right panel of the same Figure highlights the resulting structural distortions induced by the oxygen substitution within the graphene lattice in terms of color map. The average values of these angles and bond lengths, along with their standard deviations throughout the simulation, are provided in the accompanying Table 5.1.

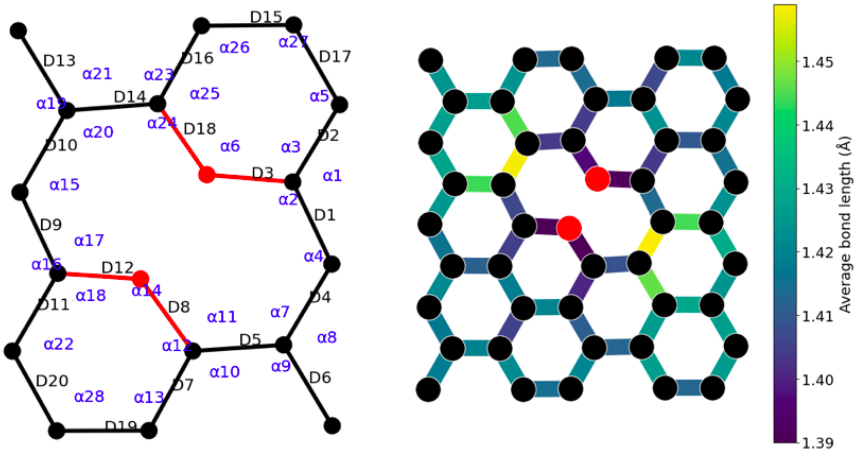

Figure 5.12. Left panel: Local view with bonds and angles labeling in the region of interest of the C376O2 system where deformations occurs as a consequence of the out-of-plane displacements of the O atoms. Right panel: Local representation as color map of bond deformations observed in the vicinity of the substitution sites.

length	**mean (Å)**	σ **(Å)**	**Angle**	**mean (°)**	σ **(°)**	**sum.**
D1	1.417	0.007	α_1	121.9	0.5	
D2	1.403	0.004	α_2	121.6	1.0	360.0
D3	1.392	0.005	α_3	116.5	0.7	
D4	1.460	0.005	α_4	125.7	1.1	
D5	1.408	0.009	α_5	119.9	0.5	
D6	1.448	0.004	α_6	118.7	0.8	
D7	1.399	0.003	α_7	124.4	0.7	
D8	1.389	0.009	α_8	119.4	1.2	359.9
D9	1.407	0.004	α_9	116.1	0.7	
D10	1.459	0.007	α_{10}	122.4	0.6	
D11	1.404	0.003	α_{11}	120.5	1.4	360.0
D12	1.389	0.009	α_{12}	117.1	1.0	
D13	1.446	0.005	α_{13}	119.2	0.3	
D14	1.403	0.005	α_{14}	119.5	0.6	
D15	1.416	0.004	α_{15}	124.5	0.7	
D16	1.404	0.004	α_{16}	122.6	0.7	
D17	1.425	0.006	α_{17}	120.2	0.9	359.9
D18	1.399	0.005	α_{18}	117.1	0.5	
D19	1.419	0.006	α_{19}	118.6	0.5	

length	mean (Å)	σ (Å)	Angle	mean (°)	σ (°)	sum.
D20	1.419	0.003	α_{20}	124.9	0.6	360.0
O-O	2.31	0.02	α_{21}	116.5	0.4	
			α_{22}	119.5	0.6	
			α_{23}	121.9	0.5	
			α_{24}	120.4	0.7	359.9
			α_{25}	117.6	0.7	
			α_{26}	119.2	0.4	
			α_{27}	118.8	0.3	
			α_{28}	119.0	0.4	

Table 5.1. Bond lengths (D_1 to D_{20}) and angles (α_1 to α_{28}), including their mean values and standard deviation complementing the information of Fig. 5.12

An obvious feature that the figure and the table provide is that the sum of the bond angles around these atoms remains on average constant iand equal to 360°, which could indicate that these structures are planar. However, we also note that the standard deviation of each of these angles is quite large. For example, for the adjacent three angles α_{10}, α_{11}, and α_{12}, the average standard deviation is $\sim 1°$. This indicates that, in these regions, the bond angles tend to fluctuate significantly. A similar behavior is seen for the triplet α_7, α_8, and α_9. The overall picture is that although the structure is on average planar, it undergoes alternating local deformations over time, resulting in dynamic distortions.
Another interesting feature is the change in bond lengths that the distortion of the lattice induces. This distortion follows a characteristic pattern: contraction of bonds in the immediate vicinity of the substituting O atoms and relaxation of bonds further away. The major deformations observed on the two bonds, shown on the right panel of Figure 5.12, is a direct consequence of the adsorption site character represented by the O atom, with consequent local electronic structure modifications. The presence of O atoms replacing regular C sites weakens the C aromatic-like bonds up to its second and third neighbors and thus accentuates the distortion. The electronic structure modifications will be discussed in a following section. I can anticipate here that the difference of electronegativity, namely 2.55 for the C and 3.44 for the O, provide a rationale for the explanation of the observed geometrical modifications.
To deepen the present analysis, I plotted in Fig. 5.13 the relative height along the z-axis of the O atoms with respect to the C atoms to which they are bonded. Once the O atoms move out of the plane, this displacement is kept throughout the whole simulation, with their positions fluctuating nearly simultaneously on either side of the structure. While the absolute values observed fluctuate between 0.3 and 0.6 Å, the average O–O distance is found to be 2.31 Å, with a standard deviation of 0.02 Å, indicating that this distance is a constant at least on the time scale of the simulation and that the deformation is a permanent feature. The differences between the z-height values shown in Fig. 5.13 and the actual O–O distance can be rationalized by the fact that the structural deformations resulting from O–O interactions are not transmitted directly through the bonded carbon atoms, but rather through second-nearest neighbors in the graphene lattice. Furthermore, the fluctuation of this distance, reflected by the small standard deviation (0.02 Å), indicates that the O–O distance varies by a factor approximately five times greater than typical interatomic fluctuation within the rest of the lattice.
This observation is corroborated by the analysis of the system deformations reported in Fig. 5.14. The Gaussian curvature map indicates that the majority of the deformations occur around the substitution site.

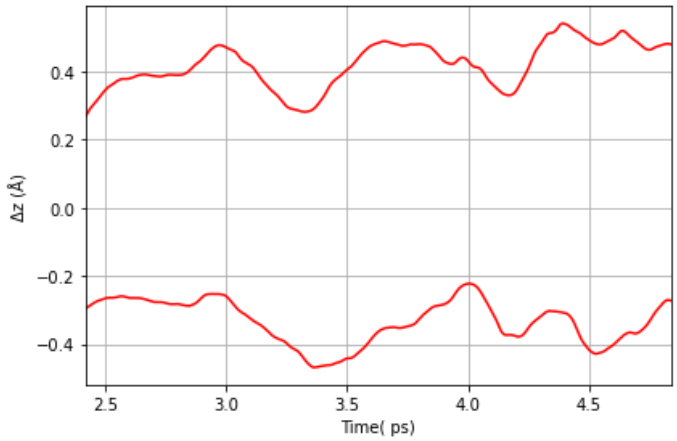

Figure 5.13. Relative height of oxygen atoms with respect to the carbon atoms to which they are bonded. Positive values refer to O atoms displaced above the graphene plane and negative values to the neighbor O atoms displaced below the graphene plane.

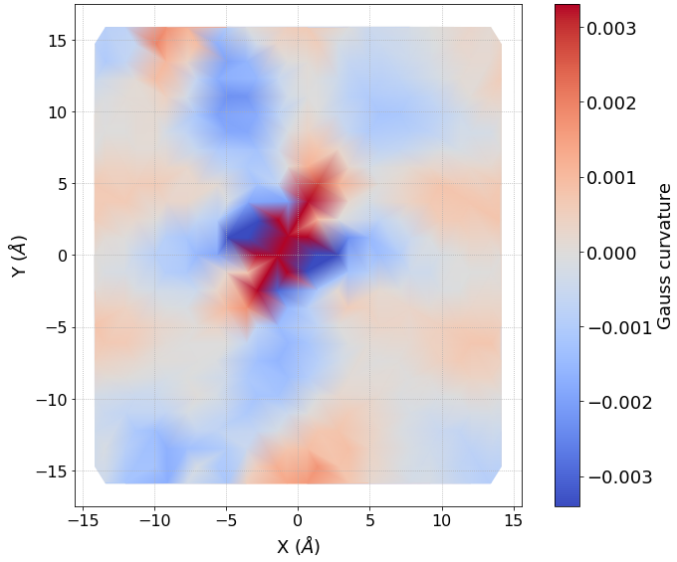

Figure 5.14. Gaussian curvature of the C376O2 system represented as a color contour map. The main values are concentrated around the region carrying the two substitutional O atoms as discussed in the text.

When comparing this system to pristine graphene composed of 378 C atoms in the same NVE ensemble and over the simulation time scale of our modeling, we observe that the average Gaussian curvature is equal to $\overline{K_{NVE}^{g378}} = 0.0006$ for pure graphene, whereas in becomes $\overline{K_{NVE}^{C376O2}} = 0.0009$, thus significantly higher, for the case of O substitution discussed in this section. This increase can be ascribed to the strong local deformation induced by the atomic substitution. For comparison with forthcoming calculations, we estimated the mean value of the RMSD over the NVE dynamic of this system, obtaining $\overline{R^2} = 1.86$ Å^2 for an average temperature of $\overline{T} = 21.7$ K.

5.2.2 Effects of Carbon-to-Oxygen Substitution in the case of a C Mono-Vacancy in Graphene

This system is composed of a graphene sheet identical to the one discussed in the former paragraph but carrying a single C vacancy and where two C atoms bordering this vacancy

are replaced by two O atoms. Contrary to the former case, here the absence of one atom and the consequent empty space created in the graphene lattice give rise to deformations less pronounced and less drastic than the ones seen in the previous section. While some out-of-plane displacements can still be observed, particularly for the O atoms and the undercoordinated C atom that has lost a chemical bond, these distortions are neither extreme nor stable over time. As shown in Fig. 5.15, the structural deformations in the region of interest remain moderate compared to those observed in the case of simple O to C replacement. The mean value of the RMSD computed during the microcanonical NVE

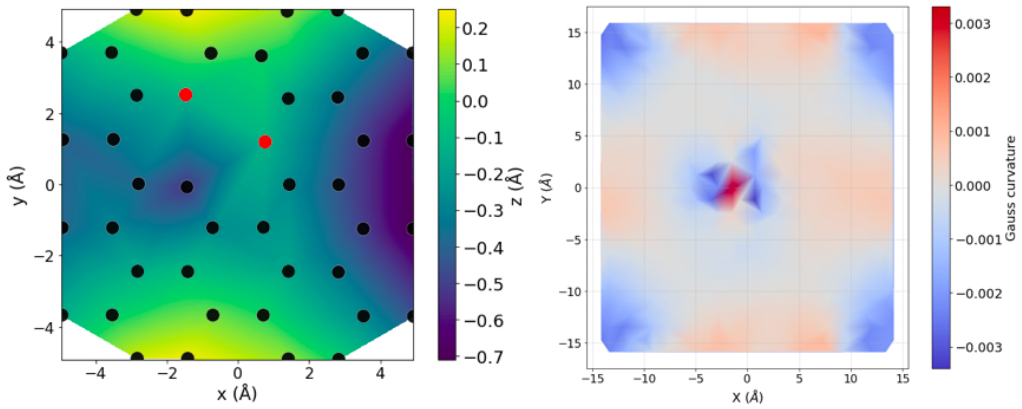

Figure 5.15. Topology of the C375O2 system. **Left panel**: contour color map showing the out-of-plane height. **Right panel**: Analogous map for the Gaussian curvature across the full graphene sheet. At the center, the topological changes induced by the C vacancy and the tw O substitutions are responsible for the increase in color intensity.

dynamic is $\overline{R^2} = 0.86$ Å^2, and the mean value of the Gaussian curvature is 0.0005. In other words, this system displays lower deformations upon the changes, i. e. C vacancy creation and two O replacements. This is reflected by a lower increase in temperature in this system compared to the previous one, the average temperature being $\overline{T} = 2.63$ K.
As in the previous case, each bond angle and bond length around the region of interest was labeled as indicated in Fig. 5.16. The corresponding numerical values are listed in Table 5.2. Compared to the previous system, the angular values are here remarkably stable and centered around 120°, indicating minimal distortion of the local structure. This observation is fully consistent with the conclusions drawn indicating a limited impact of the double substitution and vacancy on the graphene sheet overall topology.

Some notable exceptions are observed for two specific angles: α_{34}, corresponding to the C site representing the vertex between two bonded O structures, has the highest value (125.4°), and α_{15}, associated with the most mobile and reactive C atom in the region. Regarding the angle flexibility, the standard deviations reveal that the most fluctuating angles are those involving the undercoordinated C atoms, the one which is lacking its third bond because of the vacancy, thus becoming less rigid.
As for bond lengths, sketched in the right panel of Fig. 5.16, we observe a shrinking in bonds involving O atoms due to their higher electronegativity compared to C. Similarly, the C atom missing a bond because of the vacancy is characterized by shorter bond lengths with respoect to the rest of regular three-fold C sites. This can be ascribed to electron density redistribution: electrons initially involved in the now missing third bond reinforce the remaining two, thereby shortening their lengths. This local shrink is accompanied by a slight increase (relaxations) in neighboring regions, forming a compensatory pattern in the lattice. Finally, I wish to bring to the attention the fact that both the standard deviations of bond lengths and angles are, on average, lower than those observed in the

Distance	Mean	Deviation	Angle	Mean	Deviation
D1	1.404	0.001	α_1	121.4	0.3
D2	1.400	0.003	α_2	118.5	0.3
D3	1.390	0.002	α_3	120.1	0.1
D4	1.434	0.006	α_4	122.0	0.2
D5	1.426	0.002	α_5	118.6	0.4
D6	1.376	0.003	α_6	119.3	0.2
D7	1.431	0.002	α_7	119.7	0.2
D8	1.374	0.003	α_8	119.8	0.2
D9	1.438	0.003	α_9	120.5	0.4
D10	1.408	0.003	α_{10}	121.4	0.3
D11	1.433	0.002	α_{11}	122.2	0.7
D12	1.414	0.002	α_{12}	119.5	0.2
D13	1.417	0.002	α_{13}	118.2	0.7
D14	1.400	0.002	α_{14}	120.2	0.2
D15	1.419	0.003	α_{15}	124.1	0.8
D16	1.380	0.002	α_{16}	119.0	0.3
D17	1.416	0.004	α_{17}	122.7	0.2
D18	1.423	0.002	α_{18}	117.6	0.4
D19	1.421	0.002	α_{19}	119.7	0.3
D20	1.400	0.001	α_{20}	122.3	0.4
D21	1.379	0.001	α_{21}	121.8	0.3
D22	1.424	0.002	α_{22}	118.7	0.1
D23	1.451	0.002	α_{23}	119.5	0.3
D24	1.401	0.002	α_{24}	119.3	0.4
D25	1.378	0.002	α_{25}	119.9	0.3
D26	1.417	0.004	α_{26}	119.6	0.2
D27	1.421	0.002	α_{27}	119.8	0.3
D28	1.415	0.002	α_{28}	119.2	0.1
D29	1.422	0.002	α_{29}	121.9	0.1
D30	1.421	0.003	α_{30}	119.4	0.2
D31	1.420	0.002	α_{31}	121.8	0.2
D32	1.418	0.003	α_{32}	118.1	0.3
			α_{33}	120.0	0.3
			α_{34}	125.4	0.3
			α_{35}	117.1	0.2
			α_{36}	117.5	0.4
			α_{37}	121.5	0.3
			α_{38}	118.7	0.1
			α_{39}	119.8	0.2
			α_{40}	120.5	0.1
			α_{41}	119.8	0.2
			α_{42}	120.4	0.2
			α_{43}	119.7	0.1
			α_{44}	120.3	0.2
			α_{45}	119.9	0.3
			α_{46}	118.9	0.3
			α_{47}	119.7	0.3

Table 5.2. Bond lengths (D_1 to D_{33}) and angles (α_1 to α_{47}), including their mean values and standard deviation referring to the local geometry shown in Fig. 5.16

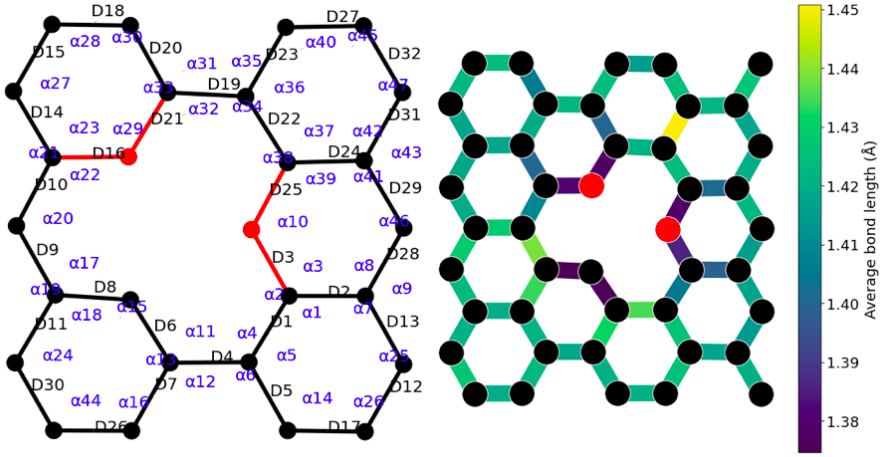

Figure 5.16. **Left panel**: local labeling of bonds and angles around the C vacancy in which two C atoms are replaced by two O atoms (highlighted in red). **Right panel**: Color map indicating the geometrical deformations around the C vacancy carrying two replacing O atoms (in red).

previous system where no vacancies are present. This confirms that the combined effect of defects composed by both missing atoms and chemical replacement.

The dynamical evolution of the O atoms displacements with respect to the two carbon atoms to which they are bonded and the one of the two-fold (because of the vacancy) C atom is what Fig. 5.17 summarizes. The general trend that emerges is that in the case of a vacancy, O atoms at its border deviate less from the planar configuration than in the previous case, keeping relative heights from the two bonded C atoms around 0.1 Å. More importantly, their relative positions are no longer mutually correlated, being the separation between the two O large enough to minimize the repulsive electrostatic interaction. An

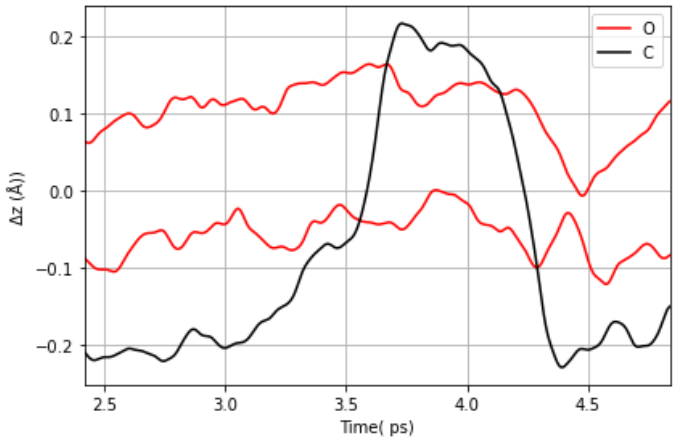

Figure 5.17. Relative height of the two O atoms and two-fold C atom surrounding the vacancy. These heights are measured with respect to the two adjacent carbon atoms. The red lines refer to the two O atoms and the black line to the two-fold C.

additional observation concerns the C atom that has lost one of its bonds and is now left as a two-fold carbon site. Unlike the O atoms, this carbon exhibits a pronounced oscillatory behavior during its time evolution between -0.2 and 0.2 Å. This means that its position periodically shifts above and below the graphene plane, relative to the two remaining C neighbor atoms. This behavior could have significant implications on both vibrational response and local dipole moment.

5.2.3 Vibrational and Dipolar Study

To get a comparative insight into the modifications induced by the presence of oxygen and/or a mono-vacancy in the response of these systems with respect to pristine graphene, I performed a systematic vibrational analysis of the three systems: the pristine graphene system composed of 378 atoms (with restraints), the C376O2 system, and the C375O2 system. The result of this analysis is the message conveyed by Fig. 5.18. Briefly, the vibrational density of states as a function of the wavenumber shows that the C375O2 system closely matches the vibrational spectrum of pristine graphene. In contrast, the C376O2 system displays an increased activity in the low-frequency region, while, simultaneously, showing a shift of its main peaks toward higher frequencies.
These results are in perfect agreement with the observations made in the previous sections, particularly regarding the topological analysis. Indeed, as observed, the C376O2 system exhibits significant out-of-plane deformations in the oxygen substitution zone, which consequently affects the overall structure and the vibrational states of the graphene sheet. Conversely, in the C375O2 system, the removal of one carbon atom creates additional space allowing the O atoms to mitigate the mutual electrostatic repulsion. As a result, the structural planarity of the graphene is preserved and its vibrational states remain largely unaffected. Given the dynamical deformations these structures undergo and the

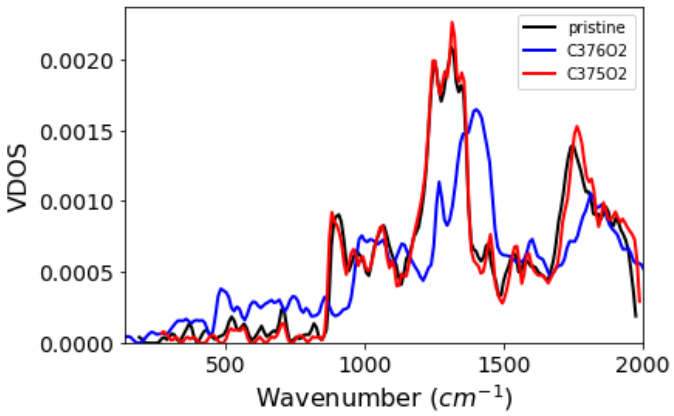

Figure 5.18. Vibrational density of states (VDOS) for the three systems: pristine graphene (black), C376O2 (blue), and C375O2 (red).

consequent response in their vibrational spectra, I undertook and additional analysis exploiting the tools and methods used all across this project, such as Maximally Localized Wannier Functions (MLWFs), to unravel the electronic behavior in these regions and to work out the related modifications. In order to ensure a consistent analysis and avoid edge effects due to either the periodic boundary conditions and/or the restraints, local areas of identical size were defined around each area of interest at the center of the sheet.
More precisely, each zone was delimited along the x and y directions as follows: $x_{min} = x_0 - 4.75$ Å, $x_{max} = x_0 + 4.75$ Å, $y_{min} = y_0 - 4.75$ Å, $y_{max} = y_0 + 4.75$ Å. where the origin (x_0, y_0) is the center of the area of interest. The selection of this area, avoiding the borders of the system for the mentioned reasons, ensures that the results obtained for the different configurations considered remain comparable. In this delimited region, I computed the local dipole moment obtaining the result shown in Fig. 5.19, where the corresponding dipole distribution is reported for the pristine graphene and the two rGO. In the case of the unperturbed pristine graphene the dipole moment distribution is characterized by a narrow peak centered around an average value of $\sim$ 82.1 D. At this stage, it is good to notice that this result is intended as an exploratory calculation to compare the local response of the different systems. Indeed, a direct comparison with experimental data

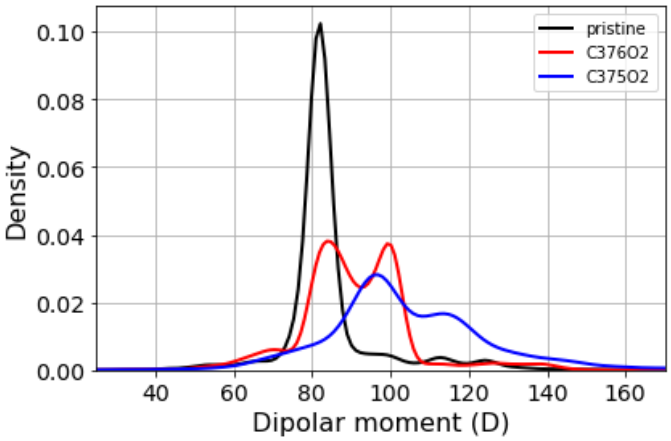

Figure 5.19. Distribution of the absolute value of the dipole moment in the area indicated in the text. The black curve refers to the pristine graphene, the red one to the C376O2 system, and the blue one to the C375O2 system.

is not possible, since the spatial region selected for the calculation of the dipole moment does not carry a net zero charge, which leads to an artificially large dipole moment. In contrast with the CNT dipolar moment calculation, for the system with two substitutional O atoms (C376O2) without vacancy, this peak splits into two distinct contribution at 83.8 and 99.2 D. Although a secondary peak appears due to increased activity around the substitution zone, the electronic structure of the system remains only mildly affected, as only more electronegative chemical species are introduced. In the case of the C375O2 system, where two C atoms are replaced by O and one carbon atom is removed in the same region, the main dipole peak shifts towards higher values ($\sim 96.8D$), accompanied by a broadening, and a secondary peak at 113.7 D arises. The broadening is an effect common to both systems carrying O atoms, but in this latter case, the dipole moment values are widely spread, ranging from 60 to 142 D. This broad distribution indicates a remarkable variability in the dipole evolution during the dynamics, translating into a stronger potential for electromagnetic absorption. Unlike in C376O2, where only electronegative species were added, the C375O2 system combines electronegative O atoms with the effects of a C monovacancy, ultimately resulting into an electronic doping and the possibility to induce free electrons. This substantially alters the system's electronic structure and can become a viable route to carbon-based materials engineering for the applications targeted in this doctoral project.

5.3 Conclusions

The methodology assessment that we did all along this work, particularly in FPMD approaches, has shown to be a powerful tool to capture the key behaviors of our system under realistic conditions and to unravel the underlying atomic-level mechanisms. Limitations due to technological shortcomings (available HPC resources) and fundamental physics (quantum mechanics reachable time and size scales) have been shown to pose some severe stumbling blocks in attaining the microwave regime. In the search for a workaround, perturbative methods have been explored, employing the dynamical matrix formalism alongside the Maximally Localized Wannier Functions method, providing detailed insights into the vibrational response and dipolar properties of the systems. We have already shown, however, that also perturbative approaches have to come to compromises in terms of tractable system size and some global behavior beyond the harmonic or perturbative approximation can still be beyond the reach.

Another important message is that finite size effects of the simulated models can introduce more or less pronounced biases and should be carefully minimized if not avoided. In our case, to mitigate this effect, we kept the system as large as possible, compatible with the available computational resources, and focused on the regions away from the borders. Another important tool is the algorithm used to mimic multilayer graphene stacking and bulk substrates, resulting in the analytical restraint that allowed to avoid increasing the size of the system. This protocol led us to identify two systems of interest: C376O2 and C375O2. We demonstrated that atomic substitutions induce significant local distortions, impacting both bond lengths adjacent to substitution sites and angles in the surrounding lattice. When substitutional O atoms are in close proximity, the resulting strong electrostatic repulsion is the driving force that induces structural perturbations. Conversely, vacancies (not only the mono-vacancy considered here but most likely also multi-vacancies) grant a sufficient separation from O atoms at the border of the empty space left by the C removal, that deviations from planarity become less pronounced with consequent milder effects on structural and vibrational properties. In fact, our vibrational analyses have shown that despite O substitutions inside the graphene lattice, if the overall structure remains preserved and planar, vibrational modes are largely unaffected. Conversely, systems experiencing a proximity of substituting O atoms exhibit remarkable changes in the vibrational spectra with new features arising.
Finally, we have shown that the introduction of hetero-atoms with different electronegativity in the graphene network influences the electronic structure, thereby enhancing electromagnetic absorption activity, which arises from modifications and relaxation phenomena in the dipole moments of the system.

Chapter 6

General conclusions and perspectives

This thesis is part of the broader effort to develop carbon-based nanomaterials for electromagnetic absorption applications in the microwave frequency range, with potential use in electronics and aeronautics. Conducted within the framework of the MOLIERE joint laboratory, this work aims to contribute to a better understanding of the structure–property relationships at the atomic scale. The central research question guiding this study is the following: do we currently possess the simulation tools and computational technologies necessary to predict and understand the real-world performance of these materials at the nanoscale?

Overview of the Conducted Work

This is why, although we focused on three distinct case studies, cobalt-decorated carbon nanotubes (CNTs), CNTs interacting with polymer (PMMA) molecules, and graphene oxide, these systems, while scientifically and industrially relevant, primarily served as platforms to address our central research question. To this end, we employed ab initio simulations using the FPMD method, which enabled us to capture the atomic, electronic, and vibrational behaviors of these systems. From the generated trajectories, we implemented several complementary analytical approaches to gain a deeper understanding of the underlying phenomena, as well as to identify the current limitations of such simulation techniques.

These methodologies, particularly suited to topological studies, allowed the CPMD framework to provide a global view of the systems under investigation, enabling us to assess their structural organization and the role of various components in determining the material properties. By invoking the fluctuation-dissipation theorem, we were able to derive the electromagnetic responses of the systems, including dielectric properties, and thereby test intensive methods on these materials.

In addition, we applied the MLWF formalism to gain insights into local dipole moments and to identify the factors influencing their variations. For the second and third systems, we also employed perturbative approaches, namely vibrational mode analysis using the dynamical matrix method, which further enriched our interpretation of the observed phenomena.

These combined techniques led to several original results. Among the earliest findings, in Chapter 3, we demonstrated that cobalt atoms placed on CNT surfaces exhibit surface mobility by creating and breaking Co–C bounds, inducing modifications to the local dipole moment, affecting the bound length at the vicinity. These alterations, in turn, give rise to a variety of emergent physical effects.

In the fourth chapter, which focused on the interaction between two carbon nanotubes and PMMA, we demonstrated that such interactions induce structural deformations, including ovalization and oscillatory variations in the inter-tube distance, manifestations of various types of collective motion between the nanotubes. Additionally, using the dynamical matrix method, we developed new tools for visualizing the phonon modes of our systems. This allowed us to show that these interactions modulate not only the phonon modes themselves but also the modes responsible for electromagnetic wave absorption.
Finally, in Chapter 5, where we investigated the effects of graphene oxide reduction, we found that structural modifications to the graphene framework resulted in both structural and electronic alterations. These changes significantly influence the system's vibrational modes and, potentially, its electromagnetic absorption properties.

Conclusion

While the relationship between microscopic and macroscopic properties, such as the absorption coefficient, remains complex and requires multi-scale approaches, this study has demonstrated the effects of interactions on local dipole moments and chemical bonding. These effects were particularly highlighted in Chapter 3, where the chemisorption of cobalt atoms onto carbon led to elongation of the first-neighbor bonds and contraction of the subsequent ones. Similarly, in Chapter 5, around the reduced regions of graphene oxide, more complex phenomena were identified, significantly influencing both the local dipole moment and the electron density distributions in those regions.
Indeed, whether in Chapter 3 or Chapter 4, it was shown that the implementation of the fluctuation-dissipation approach did not, within short simulation times, allow us to obtain a complete spectrum in the microwave range, although initial results in these frequency domains were achieved in Chapter 3. Nevertheless, this method enabled us to better understand the influence of cobalt nanoparticles (Chapter 3) and nanotube interactions (Chapter 4) on the absorption spectra. Similarly, the perturbative approach based on dynamical matrix analysis revealed a direct correlation between system size, computational cost, and the accessible time scales.
These findings illustrate that *ab initio* simulation methods can provide detailed insight into phenomena occurring at the atomic scale, helping to clarify questions situated at the interface between theoretical and macroscopic descriptions. While the fluctuation-dissipation method did allow us to probe the electromagnetic response up to microwave frequencies, computational limitations prevented us from accessing the full spectrum. System size and simulation duration remain critical constraints, with current capabilities allowing simulations of up to $\sim$1000 atoms and only over short timescales.
In this regard, current computational tools enable significant progress and offer a fundamental understanding of the underlying mechanisms. Yet, further technological developments and methodological innovations are still required to achieve complete and accurate simulations in the GHz frequency domain.

Limits and perspectives

Beyond the limitations directly addressed in response to our initial research questions, our studies also reveal several broader constraints. One significant limitation lies in the partial treatment of collective effects stemming from the global motion of atoms, which are not fully captured within the current computational framework. Systematic investigations—such as those considering the angular configurations between interacting carbon nanotubes or exploring other chemical modifications in reduced graphene oxide—remain to be conducted. Moreover, a more comprehensive integration of experimental conditions,

including the presence of interfaces or variations in material density, was not included in this work.
In particular, the influence of polymer and nanotube density (Chapter 4) and the presence of structural defects across all systems warrant further exploration. For instance, defect-related effects in the cobalt-decorated CNT systems and in the CNT–PMMA interfaces were not examined, and only partially explored in the case of reduced graphene oxide. Other types of chemical or structural modifications should also be systematically studied to better understand their impact on material properties.
The necessity of employing periodic boundary conditions, due to the limited size of the simulated systems, introduced inherent constraints. These include restrictions on the size and wavelength of accessible collective motions, which can limit the fidelity of our description of long-range interactions and macroscopic behavior.

These limitations open several promising avenues for future research. The size constraint of our systems—and, more broadly, the limited system sizes accessible to atomistic simulations, remains a critical issue in computational materials science. Recent developments, such as the use of Machine Learning Interatomic Potentials, notably those based on high-order tensor message passing interatomic potentials (HotPP), have shown great promise [128, 129]. These approaches enable the replacement of first-principles calculations by highly efficient surrogate models, allowing the simulation of significantly larger systems with reduced computational cost.
Future studies could also systematically incorporate doping effects, structural defects, and interfacial phenomena, which, as demonstrated in this thesis, can strongly influence both the local dipole moment and the electronic structure of the system. These factors play a central role in electromagnetic absorption and must therefore be considered essential parameters in the accurate modeling of nanostructured materials.
In order to gain a better understanding of the infrared and microwave absorption of our system, we focused our investigation on the study of the dipole moment dynamics as well as the vibrational (phonon) properties of the material. As discussed throughout this thesis, a crucial aspect lies in the presence of a perturbation and the subsequent relaxation of the system's dipole moment. While such effects are indeed observed in the optical phonon modes, their frequency range typically lies above 800 cm^{-1}.
Regarding the electronic density, the CPMD method allows us to track collective motions in the overall charge density of the system. However, some phenomena are poorly described within the CPMD framework. Nonetheless, we observed non-negligible variations in the dipole moment that suggest the involvement of additional mechanisms. Among these are exciton and plasmon effects, which, at well structured geometry, these electronic excitations can occur at much lower frequencies than phonons, potentially reaching the GHz range [130]. These effects merit further investigation.

Finally, the goal is to compare the simulation results with experimental data in order to validate the predictions made by the method or its improved variants, and thereby guide further methodological development. The overarching objective of such studies is to enable the use of inverse design approaches for the conception of optimized nanostructures tailored to specific absorption spectra.

Appendix 1: Python post processing

```python
centre =[0,0]
xy_zone = [centre[0]-4.75, centre[0]+4.75,centre[1]-4.75, centre[1]+4.75]  # Zone d'étude : [x_min, x_m
output_file = "dipole_local_xy_debye375.txt"
CONVERSION_DEBYE = 4.80320427  # Conversion : 1 e·A = 4.80320427 Debye
Z_values = {'C': 4, 'O': 6, 'X': -2}
Z_SHIFT_THRESHOLD = 4.0
Z_SHIFT_VALUE = 7.937658735  # Correction si z > 4 A

# ==== LECTURE DU FICHIER XYZ MULTIFRAME ====
def read_xyz_multiframe(filename):
    frames = []
    with open(filename, 'r') as f:
        while True:
            try:
                n_atoms = int(f.readline())
                _ = f.readline()  # ligne de commentaire
                atoms = []
                for _ in range(n_atoms):
                    line = f.readline()
                    if not line:
                        raise ValueError("Fin du fichier inattendue.")
                    parts = line.strip().split()
                    symbol = parts[0]
                    x, y, z = map(float, parts[1:4])

                    # Appliquer le décalage sur z si nécessaire
                    if z > Z_SHIFT_THRESHOLD:
                        z -= Z_SHIFT_VALUE

                    atoms.append((symbol, np.array([x, y, z])))
                frames.append(atoms)
            except:
                break
    return frames

# ==== CALCUL DU MOMENT DIPOLE LOCAL ====
def compute_local_dipole(frame, xy_zone):
    x_min, x_max, y_min, y_max = xy_zone
    dipole = np.zeros(3)
    for symbol, pos in frame:
        if symbol in Z_values:
            x, y, z = pos
            if x_min <= x <= x_max and y_min <= y <= y_max:
                Z = Z_values[symbol]
                dipole += Z * (pos-np.array([(xy_zone[0]+xy_zone[1])/2, (xy_zone[2]+xy_zone[3])/2,0]))
    dipole *= CONVERSION_DEBYE
    return dipole
```

Figure 1. part of the python program used to calculate the local dipolar moment in graphen.

During the Ph.D. work, all post-processing was carried out using Python programming. Consequently, all the figures presented in the thesis, except those obtained via the Maximum Entropy Method, were generated during the course of the project as the one presented Figure 1. These programs are available and can be provided upon request.

Bibliography

[1] R.R. Romanofsky FA. Miranda, F.W. Van Keuls and G. Subramanyam. Tunable microwave components for ku- and k-band satellite communications. Technical report, NASA, 1998.

[2] Dominik Maximilian Soliman. *Augmented microscopy: Development and application of high-resolution optoacoustic and multimodal imaging techniques for label-free biological observation.* PhD thesis, Fakultät für Medizin Institut für Biologische und Medizinische Bildgebung, 2017.

[3] N.D. Xuan T.A. Ho P.T.V. Ha L.T.Q. Trang N.Q. Tuan D.H. Manh T.D. Thanh N. Tran C.T.A. Xuan, P.T. Tho. Microwave absorption properties for composites of cofe2o4/ carbonaceous-based materials: A comprehensive review. *Journal of Alloys and Compounds*, 2024.

[4] Abdelnour Benzair Abdelouahed Tounsi Lakhdar Boumia, Mohamed Zidour. A timoshenko beam model for vibration analysis of chiral single-walled carbon nanotubes. *Physica E*, 2014.

[5] Jianguo He Juanjuan Wang Rong Li Jiantai Ma Zhengping Dong, Kun Ma. Decorating carbon nanotubes with cobalt nanoparticles. *Materials Letters*, 2008.

[6] Ahmed S. Abo Dena Craig E. Banks Samuel J. Rowley-Neale, Edward P. Randviir. An overview of recent applications of reduced graphene oxide as a basis of electroanalytical sensing platforms. *Applied Materials Today*, 2018.

[7] Qi Zhou Ruoxia Chen Kai Yang Zhe Wang Longwen Tang Han Liu, Zhangji Zhao and Mathieu Bauchy. Challenges and opportunities in atomistic simulations of glasses: a review. *Comptes Rendus Géoscience*, 2022.

[8] Jamal Saeedi. Feasibility study and conceptual design of missile-borne synthetic aperture radar. *IEEE TRANSACTIONS ON SYSTEMS, MAN, AND CYBERNETICS: SYSTEMS*, 2017.

[9] N.D. Mermin N.W. Ashcroft. *Physique des solides.* EDPSciences, 2002.

[10] Charles Kittel. *Introduction to Solid State Physics.* John Wiley Sons, Inc., 2005.

[11] J. D. Jackson. *Classical Electrodynamics.* John Wiley Sons, Inc., 1992.

[12] S. Dubourg O. Acher. A generalization of snoek's law to ferromagnetic films and composites. *Phys. Rev. B*, 2008.

[13] Changzhou Hua Fangxin Li, Yangong Zheng and Jiawen Jian. Gas sensing by microwave transduction: Review of progress and challenges. *Front. Mater.*, 2019.

[14] Frederick W. Van Keuls Robert R. Romanofsky Joseph D. Warner Félix A. Miranda, Guru Subramanyam and Carl H. Mueller. Design and development of ferroelectric tunable microwave components for ku- and k-band satellite communication systems. *IEEE TRANSACTIONS ON MICROWAVE THEORY AND TECHNIQUES, VOL. 48, NO. 7*, 2000.

[15] Makoto Nakajima Tohru Suemoto Kazuyuki Matsumoto Masahiro Goto Shinya Sasaki Asuka Namai, Shunsuke Sakurai and Shin ichi Ohkoshi. Synthesis of an electromagnetic wave absorber for high-speed wireless communication. 2008.

[16] FAN Xiao-Long WEN Fu-Sheng XUE De-Sheng, LI Fa-Shen. Bianisotropy picture of higher permeability at higher frequencies. *CHIN.PHYS.LETT.*, 2008.

[17] Matsumoto M and Miyata Y. Thin electromagnetic wave absorber for quasi-microwave band containing aligned thin magnetic metal particles. *IEEE Transactions on Magnetics*, 2002.

[18] Yuanyuan Liu Xuefeng Zhang and Gaowu Qin. Break snoek limit via superparamagnetic coupling in fe3o4/silica multiple-core/shell nanoparticles. *Applied Physics Letters*, 2015.

[19] Xianghua Han Yong Ren-Qingfang Liu Longgang Yan, Jianbo Wang1 and Fashen Li. Enhanced microwave absorption of fe nanoflakes after coating with sio2 nanoshell. *Nanotechnology*, 2010.

[20] Zo Raolison. *Synthèse et caractérisations de matériaux compositesà inclusions magnétiques lamellaire pour l'absorption micro-onde.* PhD thesis, Université de Strabourg, 2013.

[21] E. M. Eldesouki W. A. Abd El-Ghany W. M. Abd El-Gawad. Development of high performance microwave absorption modified epoxy coatings based on nano-ferrites. *scientific reports*, 2024.

[22] F. Qin and C. Brosseau. A review and analysis of microwave absorption in polymer composites filled with carbonaceous particles. *J. Appl. Phys.*, 2012.

[23] J.; Lou J.; Young R. J.; Ajayan P. M. Kinloch, I. A.; Suhr. Composites with carbon nanotubes and graphene: An outlook. *science*, 2018.

[24] S. V. Morozov D. Jiang M. I. Katsnelson I. V. Grigorieva S. V. Dubonos A. A. Firsov K. S. Novoselov, A. K. Geim. Two-dimensional gas of massless dirac fermions in graphene. *nature*, 2005.

[25] C Vallés A Liscio V Palermo M A Bissett R J Young A J Marsden, D G Papageorgiou and I A Kinloch. Electrical percolation in graphene–polymer composites. *2D Materials*, 2018.

[26] Sumio Iijima. Helical microtubules of graphitic carbon. *Nature*, 1991.

[27] Irum Rafique Bakhtiar Muhammad Ayesha Kausar. Review of applications of polymer/carbon nanotubes and epoxy/cnt composites. *Polymer-Plastics Technology and Engineering*, 2016.

[28] Lei Shi Huiju Cao. sp1-hybridized linear and cyclic carbon chain. *Chinese Chemical Letters*, 2025.

[29] Ruixin Wu Hua Zhu, Ping Chen and Hui Zhang. Microwave absorption properties of carbon fibre containing nonwovens. *Indian Journal of fibre Textile Research*, 2007.

[30] M. ENDO A. OBERUN and T. KOYAMA. Filamentous growth of carbon through benzene decomposition. *journal of Crystal Growth*, 1976.

[31] David TILVE MARTÍNEZ. *3D printing and electromagnetic properties of conductive nanocarbon based composites*. PhD thesis, UNIVERSITÉ DE BORDEAUX, 2023.

[32] S. Motahari A. Abolghasemi Mahani and V. Nayyeri. Electromagnetic and microwave absorption characteristics of pmma composites filled with a nanoporous resorcinol formaldehyde based carbon aerogel. *RSC Advances*, 2018.

[33] Lu-Chang Qin. Determination of the chiral indices (n,m) of carbon nanotubes by electron diffraction. *Physical Chemistry Chemical Physic*, 2006.

[34] P. M. Ajayan and T. W. Ebbesen. Nanometre-size tubes of carbon. *Rep. Prog. Phys.*, 1997.

[35] L. Lewis Y. Zhou, F. Pervin and S. Jeelani. Experimental study on the thermal and mechanical properties of multi-walled carbon nanotube-reinforced epoxy. *Materials Science and Engineering A*, 2006.

[36] Josef Z. Kovacs Wolfgang Bauhofer. A review and analysis of electrical percolation in carbon nanotube polymer composites. *Composites Science and Technology*, 2009.

[37] Alexander Markevich Er-Xiong Ding Mukesh Tripathi Aqeel Hussain Clemens Mangler Esko I. Kauppinen Toma Susi Heena Inani, Kimmo Mustonen and Jani Kotakoski. Silicon substitution in nanotubes and graphene via intermittent vacancies. *J. Physical Chemistry*, 2019.

[38] L. Yang L. Dong D. Wang X. Xu D. Wang J. Huang M. Lv H. Wang H. Chen, W. Wang. A review of cobalt-containing nanomaterials, carbon nanomaterials and their composites in preparation methods and application. *Nanomaterials 12*, 2022.

[39] D. P. Randall V. Kotzeva P. C. P. Watts, W. K. Hsu and G. Z. Chen. Fe-filled carbon nanotubes: Nano-electromagnetic inductors. *Chem. Mater.*, 2002.

[40] Xiaofeng Duan Qing Chen Renchao Che, Lian-Mao Peng and Xuelei Liang. Microwave absorption enhancement and complex permittivity and permeability of fe encapsulated within carbon nanotubes. *Advenced Materials*, 2024.

[41] R. C. Che; C. Y. Zhi; C. Y. Liang; X. G. Zhou. Fabrication and microwave absorption of carbon/spinel nanocomposite. *Appl. Phys. Lett. 88, 033105*, 2006.

[42] C. T. Hsieh and J.Y. Lin. Electrochemical capacitance from carbon nanotubes decorated with cobalt oxide nanoparticles in alkali electrolyte. *ECS Transactions*, 2008.

[43] W.Z. Chen H.I. Elim W. Ji G.L. Chong C.H. Sow A.T.S. Wee K.C. Chin, A. Gohel. Gold and silver coated carbon nanotubes: An improved broad-band optical limiter. *Chemical Physics Letters*, 2005.

[44] Yan Lin Peixin Cui Kaian Sun Yunqi Liu Yuan Pan, Yinjuan Chen and Chenguang Liu. Cobalt nickel phosphide nanoparticles decorated carbon nanotubes as advanced hybrid catalysts for hydrogen evolution. *Journal of Materials Chemistry A*, 2016.

[45] Jinjun Qiu Towchong Chong Yihong Wu, Peiwen Qiao and Teck-Seng Low. Magnetic nanostructures grown on vertically aligned carbon nanotube templates. *Nano Letters*, 2002.

[46] H.I. Elim W. Ji G.L. Chong K.Y. Lim C.H. Sow A.T.S. Wee K.C. Chin, A. Gohel. Optical limiting properties of amorphous sixny and sic coated carbon nanotubes. *Chem. Phys. Lett. 383 (1)*, 2004.

[47] Jing Li Zhiliang Yu Wei Cai Jiehe Sui, Cheng Zhang. Microwave absorption and catalytic activity of carbon nanotubes decorated with cobalt nanoparticles. *Materials Letters*, 2012.

[48] S.J. Oh S.C. Lim K.H. An Y.H. Lee J.-H. Son C. Kang, I.H. Maeng. Terahertz optical and electrical properties of hydrogen-functionalized carbon nanotubes. *Phys. Rev. B 75*, 2007.

[49] A. K. GEIM and K. S. NOVOSELOV. The rise of graphene. *nature materials*, 2007.

[50] L. Colombo P. R. Gellert M. G. Schwab K. Kim K. S. Novoselov, V. I. Fal9ko. A roadmap for graphene. *nature*, 2012.

[51] James M. Tour Ayrat M. Dimiev. Mechanism of graphene oxide formation. *ACS Nano*, 2014.

[52] Hui-Ming Cheng Songfeng Pei. The reduction of graphene oxide. *Carbon*, 2012.

[53] Zunfeng Liu Randall M. Stoltenberg Zhenan Bao Héctor A. Becerril, Jie Mao and Yongsheng Chen. Evaluation of solution-processed reduced graphene oxide films as transparent conductors. *ACSnano*, 2008.

[54] D. C. Allan T. A. Arias J. D. Joannopoulos M. C. Payne, M. P. Teter. Iterative minimization techniques for ab initio total-energy calculation : molecular dynamics and conjugate gradientd. *Rev. Mod. Phys. 64, 1045*, 1992.

[55] W. Kohn. Nobel lecture: Electronic structure of matter—wave functions and density functionals. *Rev. Mod. Phys. 71, 1253*, 1 October, 1999.

[56] Elliott H. Lieb. Thomas-fermi theory. *Kluwer Encyclopedia of Mathematics, Supplement vol.II, p.455-457*, 2000.

[57] W. Kohn P. Hohenberg. Inhomogeneous electron gas. *Phys. Rev. 136, B864*, 1964.

[58] W. Kohn and L. J. Sham. Self-consistent equations including exchange and correlation effects. *Phys. Rev. 140, A1133*, 1965.

[59] P.A. M. Dirac. Note on exchange phenomena in the thomas atom. *Math.Proc.Cambridge Phil.Soc. 26*, 2008.

[60] A. Zunger J.P. Perdew. Self-interaction correction to density-functional approximations for many-electron systems. *Phys. Rev. B, 23:5048–5079*, 1981.

[61] J. P. Perdew and al. Prescription for the design and selection of density functional approximations: More constraint satisfaction with fewer fits. *J. Chem. Phys. 123, 062201*, 2005.

[62] M. Ernzerhof J. P. Perdew, K. Burke. Generalized gradient approximation made simple. *Phys. Rev. Lett. 77, 3865*, 1996.

[63] A.D. Becke. A new inhomogeneity parameter in density-functional theory. *The Journal of Chemical Physics*, 1998.

[64] R. G. Parr C. Lee, W. Yang. Development of the colle-salvetti correlation-energy formula into a functional of the electron density. *Phys. Rev. B 37, 785*, 1988.

[65] C. Adamo; V. Barone. Toward reliable density functional methods without adjustable parameters: The pbe0 model. *J. Chem. Phys. 110, 6158–6170*, 1999.

[66] A. D. Becke. Density-functional thermochemistry. iii. the role of exact exchange. *The Journal of Chemical Physics 98, 5648*, 1993.

[67] M. Elstner, D. Porezag, G. Jungnickel, J. Elsner, M. Haugk, Th. Frauenheim, S. Suhai, and G. Seifert. Self-consistent-charge density-functional tight-binding method for simulations of complex materials properties. *Phys. Rev. B*, 58:7260–7268, Sep 1998.

[68] Wijnand T. M. Mooij, Bouke P. van Eijck, and Jan Kroon. Transferable ab initio intermolecular potentials. 2. validation and application to crystal structure prediction. *The Journal of Physical Chemistry A*, 103(48):9883–9890, 1999.

[69] Stefan Grimme, Jens Antony, Stephan Ehrlich, and Helge Krieg. A consistent and accurate ab initio parametrization of density functional dispersion correction (dft-d) for the 94 elements h-pu. *The Journal of chemical physics*, 132:154104, 04 2010.

[70] Grimme S. Semiempirical gga-type density functional constructed with a long-range dispersion correction. *J. Comput. Chem., 27: 1787-1799*, 2006.

[71] Hutter J. Marx D. *Ab Initio Molecular Dynamics: Basic Theory and Advanced Methods.* Cambridge University Press, 2009.

[72] M. Boero A. Bouzid G. Ori P. L. Silvestrelli, E. Martin and C. Massobrio. Atomic structure of glassy gete 4 as a playground to assess the performances of density functional schemes accounting for dispersion forces. *The Journal of Physical Chemistry B*, 2020.

[73] A. Bouzid, C. Massobrio, M. Boero, G. Ori, K. Sykina, and E. Furet. Role of the van der waals interactions and impact of the exchange-correlation functional in determining the structure of glassy gete4. *Phys. Rev. B 92, 134208*, 2015.

[74] P. Schwerdtfeger. The pseudopotential approximation in electronic structure theory. *ChemPhysChem, 12(17):3143–3155*, 2011.

[75] L. Kleinman J.C. Phillips. New method for calculating wave functions in crystals and molecules. *Phys. Rev., 116(2):287*, 1959.

[76] J.L. Martins N. Troullier. Efficient pseudopotentials for plane-wave calculations. *Phys. Rev. B 43 (3)*, 1991.

[77] L. Hedin U. von Barth. A local exchange-correlation potential for the spin polarized case. *J. Phys. C: Solid State Phys. 5 1629*, 1972.

[78] S. Goedecker, M. Teter, and J. Hutter. Separable dual-space gaussian pseudopotentials. *Phys. Rev.B*, 54(3):1703–1710, 1996.

[79] F. Bloch. About the quantum mechanics of the electrons in crystal lattices. *Zeitschrift für physik 52.7*, 1929.

[80] B. Liu K. Zhou. Molecular dynamics simulation: Fundamentals and applica- tions. *Academic Press*, 2022.

[81] Godehard G. Sutmann. *Quantum Simulations of Complex Many-Body Systems : From Theory to Algorithms (chap. Classical molecular dynamic)*. 2009.

[82] B.J. Alder and T.E. Wainwright. Phase transition for a hard sphere system. . *Chem. Phys., 27(5):1208–1209*, 1957.

[83] L. Verlet. Computer" experiments" on classical fluids. i. thermodynamical properties of lennard-jones molecules. *Phys. Rev., 159(1):98*, 1967.

[84] M. Parrinello R.Car. Unified approach for molecular dynamics and density-functional theory. *Phys. Rev. Lett.*, 55:2471–2474, Nov 1985.

[85] Schütte C. Bornemann, F. A mathematical investigation of the car-parrinello method. *Numer. Math. 78, 359–376*, 1998.

[86] F. Buda G. Pastore, E. Smargiassi. Theory of ab initio molecular-dynamics calculations. *Phys. Rev. A*, 44:6334–6347, Nov 1991.

[87] S. Nosé. A unified formulation of the constant temperature molecular dynamics methods. *J. Chem. Phys. 81, 511*, 1984.

[88] W. G. Hoover. Canonical dynamics : Equilibrium phase-space distributions. *Phys. Rev. A 31, 1965*, 1985.

[89] C. Massobrio and al. On the actual difference between the nosé and the nosé–hoover thermostats : A critical review of canonical temperature control by molecular dynamics. *physica status solidi (b) 261.1*, 2024.

[90] T. A. Welton H. B. Callen. Irreversibility and generalized noise. *Phys. Rev. 83, 34*, 1951.

[91] R. Kubo. The fluctuation-dissipation theorem. *Rep. Prog. Phys. 29 255*, 1966.

[92] M. Parrinello P. L. Silvestrelli, M. Bernasconi. Ab initio infrared spectrum of liquid water. *Chemical Physics Letters 277 478-482*, 1997.

[93] E. Gull R. Levy, J.P.F. LeBlanca. Implementation of the maximum entropy method for analytic continuation. *Computer Physics Communications*, 2017.

[94] Valerio Lucarini, Kai Peiponen, Jarkko Saarinen, and Erik Vartiainen. *The Maximum Entropy Method: Theory and Applications*. 01 2005.

[95] E. T. Jaynes. Information theory and statistical mechanics. *Physical review*, 1957.

[96] J.A. JONES and P.J.HORE. The maximum entropy method and fourier transformation compare. *JOURNAL OF MAGNETIC RESONANCE 92,276-292*, 1991.

[97] G. J. Daniell S. F. Gull. Image reconstruction from incomplete and noisy data. *Nature*, 1978.

[98] D. Vanderbilt N. Marzari. Maximally-localized generalized wannier functions for composite energy bands. *Phys. Rev. B 56, 12847*, 1997.

[99] S. Sorella R. Resta. Electron localization in the insulating state. *Phys. Rev. Lett. 82, 370*, 1999.

[100] G. Eckold. *International Tables for Crystallography.* A. Authier, 2014.

[101] E. Targholi, M. Molaei, and S. Mousavi-Khoshdel. (10,10) single walled carbon nanotube consisted of chemisorbed oxygen atoms as a promising supercapacitor electrode material:a first principles study. *Chem. Phys. Lett.*, 664:96–100, 2016.

[102] M. S. Dresselhaus, G. Dresselhaus, R. Saito, and A. Jorio. Raman spectroscopy of carbon nanotubes. *Physics Reports*, 409:47–99, 2005.

[103] T. W. Odom, J. L. Huang, P. Kim, and C. M. Lieber. Structure and electronic properties of carbon nanotubes. *J. Chem. Phys. B*, 104:2794–2809, 2000.

[104] Jamorski. C., A. Martinez, M. Castro, and D. R. Salahub. Structure and properties of cobalt clusters up to the tetramer: A density-functional study. *Phys. Rev. B*, 55:10905–10921, 1977.

[105] Shuangye; Moro Ramiro; Xu, Xiaoshan; Yin and Walt A. de Heer. Magnetic moments and adiabatic magnetization of free cobalt clusters. *PHYSICAL REVIEW LETTERS*, 2005.

[106] Mark B. Knickelbein. Magnetic moments of bare and benzene-capped cobalt clusters. *J. Chem. Phys.*, 2006.

[107] R. Scipioni, M. Pumera, M. Boero, Y. Miyahara, and T. Ohno. Investigation of the mechanism of adsorption of β-nicotinamide adenine dinucleotide on single-walled carbon nanotubes. *J. Phys. Chem. Lett.*, 1:122–125, 2010.

[108] Jonathan R. Yates Ivo Souza Nicola Marzari, Arash A. Mostofi and David Vanderbilt. Maximally localized wannier functions: Theory and applications. *Rev. Mod. Phys. 84, 1419*, 2012.

[109] P. L. Silvestrelli. Van der waals interactions in dft made easy by wannier functions. *Phys. Rev. Lett.*, 100:053002, 2008.

[110] T. Ikeda and M. Boero. Role of van der waals corrections in first principles simulations of alkali metal ions in aqueous solutions. *J. Chem. Phys*, 143:194510, 2015.

[111] W. Betteridge. The properties of metallic cobalt. *Prog. Mater. Sci.*, 24:51–142, 1980.

[112] D. Vanderbilt N. Marzari, I. Souza. An introduction to maximally-localized wannier functions. report.

[113] K Sbai, A. RahmaniH, H. Chadli, J.-L. Bantignies, P. Hermet, and J.-L. Sauvajol. Infrared spectroscopy of single-walled carbon nanotubes. *J. Phys. Chem. B*, 110:12388–12393, 2006.

[114] N. Kouklin, M. Tzolov, D. Straus, A. Yin, and J. M. Xu. Infrared adsorption properties of carbon nanotubes synthesized by chemical vapor deposition. *Appl. Phys. Lett.*, 85:4463–4465, 2004.

[115] A. Bigotto, V. Galasso, and G. De Alti. Infrared spectra and normal vibrations of cobalt(ii), nickel(ii) and palladium(ii) complexes with n,n'-ethylenebis(acetylacetoneimine). *Spectrochimica Acta Part A: Molecular Spectroscopy*, 28(8):1581–1591, 1972.

[116] K. Ishisone, G. Ori, and M. Boero. Structural, dynamical, and electronic properties of the ionic liquid 1-ethyl-3-methylimidazolium bis(trifluoromethylsulfonyl)imide. *Phys. Chem. Chem. Phys.*, 24:9597–9607, 2022.

[117] B. V. Potapkin J. M. Kenny K. Yu. Khromov, A. A. Knizhnik. Multiscale modeling of electrical conductivity of carbon nanotubes based polymer nanocomposites. *J. Appl. Phys.*, 2017.

[118] Dongya Ma, Shuzhi Yan, Xinru Xue, Miao Niu, Hongliang Li, Deyu Bao, Chao Zhao, Xiujun Li, Peng Wang, Rong Li, Lei Huang, Miao Yu, Sitong Jia, Yanjiao Wang, Xiao Li, Zhen Zhang, and Tie Wang. Carbon nanotube wrapped hydrogen-bonded organic frameworks towards superior na+ storage in the capacitive deionization process. *Separation and Purification Technology*, 339:126728, 2024.

[119] Bertram R. Korostelev A. Fabiola, F. and M.S. Chapman. An improved hydrogen bond potential: Impact on medium resolution protein structures. *Protein Science*, 2002.

[120] Albert J. Pool, Sandeep K. Jain, and Gerard T. Barkema. Structural characterization of carbon nanotubes via the vibrational density of states. *Carbon*, 118:58–65, 2017.

[121] Neeraj Mishra, John Boeckl, Nunzio Motta, and Francesca Iacopi. Graphene growth on silicon carbide: A review. *physica status solidi (a)*, 213(9):2277–2289, 2016.

[122] Hannes C. Schniepp, Je-Luen Li, Michael J. McAllister, Hiroaki Sai, Margarita Herrera-Alonso, Douglas H. Adamson, Robert K. Prud'homme, Roberto Car, Dudley A. Saville, and Ilhan A. Aksay. Functionalized single graphene sheets derived from splitting graphite oxide. *The Journal of Physical Chemistry B*, 110(17):8535–8539, 2006.

[123] Mauro Boero, Fumihiro Imoto, and Atsushi Oshiyama. Atomistic insight into the initial stage of graphene formation on sic(0001) surfaces. *Phys. Rev. Mater.*, 6:093403, Sep 2022.

[124] L. C. Ferreira F. J. H. Ramos M. Marques L. F. M. Rocha, S. B. Cordeiro. Effect of carbon fillers in ultrahigh molecular weight polyethylene matrix prepared by twin-screw extrusion. *Materials Sciences and Applications*, 2016.

[125] Takashi Ikeda, Mauro Boero, Sheng-Feng Huang, Kiyoyuki Terakura, Masaharu Oshima, and Jun-ichi Ozaki. Carbon alloy catalysts: Active sites for oxygen reduction reaction. *The Journal of Physical Chemistry C*, 112(38):14706–14709, 2008.

[126] R. A. Lad L. A. Girifalco. Energy of cohesion, compressibility, and the potential energy functions of the graphite system. *J. Chem. Phys.*, 1956.

[127] John A. Pople Benny G. Johnson, Peter M. W. Gill. The performance of a family of density functional methods. *J. Chem. Phys.*, 1993.

[128] Haoting Zhang Ziyang Yang Zhixin Liang Jiuyang Shi Hui-Tian Wang Dingyu Xing Jian Sun Junjie Wang, Yong Wang. E(n)-equivariant cartesian tensor message passing interatomic potential. *Nature*, 2024.

[129] Y. Zhangc J. Xia and B. Jiang. The evolution of machine learning potentials for molecules, reactions and materials. *Chem. Soc. Rev.*, 2025.

[130] Garcia-Vidal FJ. Pendry JB, Martín-Moreno L. Mimicking surface plasmons with structured surfaces. *Science*, 2004.

Scientific productions

Scientific publications

1. C. Massobrio, I.A. Essomba, M. Boero, C. Diarra, M. Guerboub, K. Ishisone, A. Lambrecht, E. Martin, **I. Morrot-Woisard**, G. Ori, C. Tugène, S.D. Wansi Wendji 'On the actual difference between the Nosé and the Nosé-Hoover thermostats: a critical review of canonical temperature control by molecular dynamics' *Phys. Status Solids B* 261, 2300209 **(2024)**. DOI: 10.1002/pssb.202300209; HAL: hal-04280276.

2. **I. Morrot-Woisard**, E.K. Nguyen, N. Vukadinovic, and M. Boero. 'Structural, electronic and dielectric properties of carbon nanotubes interacting with Co nanoclusters.' *Carbon Trends* 17, 100410 **(2024)**. DOI: .10.1016/j.cartre.2024.100410.

3. Work on progress for a publication based on the Chapter 4, to be submited to Solid State Science (Elsevier).

Contribution at national/international conferences, workshops, and Schools

1. Participation and oral presentation at the workshop organized by the Joint Research Laboratory MOLIERE to report on the progress of the work, on **Wednesday, November 23, 2022** in Saint-Cloud. Also presented a seminar on the same topic to the AID on **May 11, 2023**.

2. Participation and oral presentation at the workshop organized by the Joint Research Laboratory MOLIERE to report on the progress of the work, on **November 20, 2023** in Nancy.

3. Participation in the summer school organized by the **ModMat** network on the topic of **materials modeling**, held in Banyuls from **August 19 to 23, 2024**.

4. Participation and oral presentation at the **E-MRS** conference, from **September 16 to 19, 2024** in Warsaw, Poland.

5. Participation and oral presentation at the workshop organized by the Joint Research Laboratory MOLIERE to report on the progress of the work, on **November 21, 2024** at IPCMS in Strasbourg. Also presented a seminar on the same topic to the AID on **April 29, 2025** in Saint-Cloud

Résumé détaillé de la thèse en français

Introduction

Depuis leur découverte au XIXe siècle, les ondes électromagnétiques (OEM) ont été largement utilisées dans de nombreux domaines, notamment les télécommunications, l'électronique, le diagnostic médical, la détection par radar et le traitement de l'information. Un tel éventail d'applications implique une technologie en constante évolution pour générer, absorber et manipuler les OEM. Dans l'exemple classique des télécommunications, la plage de fréquences utilisée, appelée bande, correspond à un intervalle situé entre environ 3 et 300 GHz, généralement désigné comme la région des micro-ondes. La nécessité de disposer d'appareils et d'instruments capables de fonctionner dans le domaine des micro-ondes a été la principale motivation qui a orienté le domaine des sciences des matériaux dans cette direction. Dans le cas de l'aéronautique militaire, la réduction de la signature électromagnétique est un enjeu majeur car ça permet de diminuer la détectabilité des avions. Une des notions importantes dans ce domaine est la radar cross section qui est une propriété physique des objets qui permet de mesurer la surface de réflexion de celui-ci et influant sur sa susceptibilité à être détecté. Deux paramètres majeurs influant sur la RCS sont la forme de l'objet, avoir une géométrie permettant de dévier les ondes EM incidente, et les matériaux utilisés pour la fabrication de l'objet dont les capacités d'absorption EM peuvent varier.

Les dispositifs électroniques utilisés dans les applications aéronautiques, où les équipements électroniques sont exposés à des radiations de diverses natures, qu'elles soient naturelles, comme les radiations cosmiques, ou dues à des activités humaines au sol ou via des satellites, représentent une motivation majeure qui pousse la recherche mondiale à développer des matériaux capables de réagir de manière appropriée aux ondes électromagnétiques incidentes. Les tentatives de suppression ou d'atténuation des interférences électromagnétiques (EMI) sont devenues une activité de premier plan, donnant un nouvel élan à la recherche de matériaux possédant des caractéristiques souhaitées et modulables, capables de protéger ou de dévier les radiations entrantes.
Dans ce cadre général, la vaste gamme de systèmes potentiellement capables de répondre aux exigences mentionnées est donc réduite à ceux garantissant l'utilisation d'éléments chimiques accessibles, des coûts de fabrication abordable et une durabilité. Les matériaux nano composites à base de Carbonne font alors l'objet de grand intérêt pour leurs propriétés mécanique, thermique et électronique, mais également pour leurs grandes versatilités d'utilisation et de fabrication qui permet d'obtenir des nano composites de taille et de forme très variées.

Ma thèse prend place dans le laboratoire commun MOLIERE, qui regroupe des laboratoires du CNRS (IPCMS, IJL) et Dassault-Aviation. Ce laboratoire a pour but de résoudre des problèmes soulevés dans le domaine de l'aviation civil et militaire sur le sujet des matériaux pour l'électromagnétisme, afin de développer des nouveaux matériaux

à haute valeur ajoutée, dans le domaine des micro-ondes. Si expérimentalement, des matériaux sont déjà connus et exploités, une zone d'ombre subsiste dans la compréhension microscopique des propriétés macroscopiques observées expérimentalement. Mon but est donc de travailler sur les mécanismes d'absorption EM de nano composite de Carbonne et donc d'identifier et de comprendre ces mécanismes, qui se font à l'échelle atomique de la structure et qui agissent sur les spectres permittivité et perméabilité. Pour cette étude, j'utilise une méthode de simulation appelée dynamique moléculaire, et l'originalité de ma méthode est que je vais le faire ab-initio (AIMD) afin d'avoir une description complète de mes systèmes et ainsi avoir une compréhension fine des mécanismes structurels et électroniques qui entrent en considération. Plus particulièrement, je vais utiliser la méthode de Dynamique moléculaire de Car- Parrinello (CPMD), qui est aujourd'hui la méthode qui offre le meilleur compromis entre précision ab-initio et long temps de calcule. Pour cela il m'a fallu avoir accès à des ressources de calcule à haute performance, j'ai donc eu accès au centre de calcul régional HPC, CAIUS, mais également au trés grand centre de calcul (TGCC) du CEA, IRENE.

La seconde problématique centrale de cette recherche est une question sur les capacitées actulle à entrprendre ce genre de calcul complexe et donc de repondre à la question : *Disposons-nous aujourd'hui des outils de simulation et de la technologie nécessaires pour prédire et comprendre les performances réelles de ces matériaux à l'échelle nanométrique ?*

Pour répondre à ces questions, trois systèmes modèles ont été étudiés :

- Les nanotubes de carbone (CNT) décorés de cobalt.
- Les CNT en interaction avec un polymère (PMMA).
- Le graphène oxyde réduit (rGO).

Méthodologie générale

Notre approche repose principalement sur des simulations ab initio par dynamique moléculaire au première principes (FPMD), en utilisant la méthodologie Car-Parrinello (CPMD), où les systèmes étudiés sont initialement construits à partir des positions atomiques de départ. La première étape du processus consiste à définir les fonctions d'onde électroniques associées au système, puis à les optimiser de manière à atteindre un état électronique stable. Ce n'est qu'une fois cette optimisation réalisée que la dynamique peut être amorcée, permettant ainsi le calcul des trajectoires physiques du système au cours du temps. À partir des trajectoires générées, différentes analyses complémentaires ont été réalisées :

- Études topologiques et structurales (longueurs de liaisons, angles entre atomes, courbures), rendu possible grace à l'evolution en direct des positions atomique au cour de la simulation.
- Analyse de la densité électronique et du moment dipolaire local via les fonctions d'onde de Wannier, ces fonctions sont trouvé grace à la méthode *Maximally located Wannier Function* (MLWF), notament grace à la transformation proposé par Marzari et Vanderbilt qui est une transformtion unitaire entre les fonctions d'onde de Kohn-Sham et les fonctions d'onde de Wannier qui minimise l'étalement des es fonctions, et ainsi suivre de facon pseudo-classique les centre de Wannier.
- Étude des réponses diéléctrique via le théorème de fluctuation-dissipation celon le formalisme de Kubo, appliqué sur le moment dipolaire de notre système, ce qui nous permet d'avoir le spectre d'absorption de notre système, en fréquentiel.
- Étude vibratoire par matrices dynamiques (modes normaux, phonons).

Système 1 : CNT décorés au cobalt

Dans un premier temps, j'ai étudié l'influence de l'interaction entre des nanotubes de carbone (NTC) et des nanoparticules ferromagnétiques de cobalt (Co). De nombreuses études expérimentales ont montré que l'intégration de nanoparticules ferromagnétiques au sein de structures à base de NTC permet d'améliorer les propriétés diélectriques des matériaux composites, tout en préservant de bonnes performances mécaniques. Il a également été démontré que certains paramètres structuraux ou chimiques, tels que la densité de nanoparticules de cobalt par unité de surface du nanotube, permettent de moduler cet effet.

À partir des données issues de la littérature expérimentale sur les systèmes NTC/Co, j'ai construit et simulé trois configurations distinctes :

- Le premier système est un nanotube de type (10,10) composé de 240 atomes de Carbone, isolé dans une boîte périodique étendue selon son axe, reproduisant un fort rapport d'aspect. Ce système de référence a servi à la fois de *point de comparaison* avec les systèmes décorés et de *base de validation* de la méthode de simulation, en raison de sa similarité avec des études ab initio déjà publiées.

- Les deuxième et troisième systèmes sont des nanotubes de type (10,10) décorés par des nano-agrégats de cobalt, composé de 12 atomes de Cobalt, avec deux densités différentes de dépôt, trois et quatres nano-aggregat à la surface des CNT. Ces configurations permettent d'étudier l'impact de la concentration en Co sur les propriétés électromagnétiques.

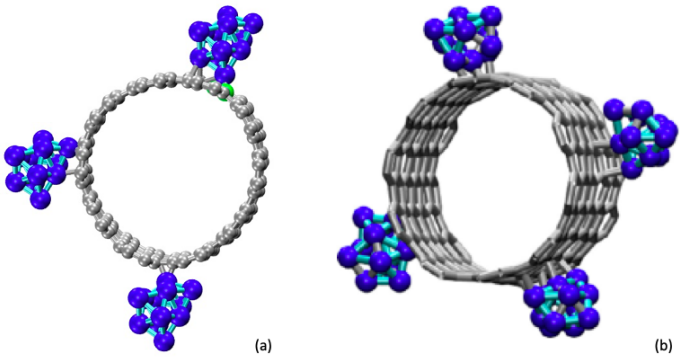

Figure 2. Systèmes simulés de : (a) le nanotube de carbone (10,10) décoré avec trois nanoclusters de Co, et (b) le nanotube de carbone (10,10) décoré avec quatre nanoclusters de Co.

Cette étude a été menée sur l'infrastructure de calcul haute performance **CAIUS**.

Organisation atomique et structure locale

La nature dynamique de la méthode employée permet également d'accéder à des informations sur les structures atomiques. Nous avons alors observé que les atomes de cobalt ont tendance à se déplacer le long de la surface du nanotube, via un processus de creation puis de déstruction de liaison Carbone-Cobalt, ce processus etant apparenté à de la chemisorption, il modifie les structures electronique local autour de ces liaisons, créant des distorsions locales. Ces modifications locales vous ensuite se diffusé au sein de la structure, ce qui va entrainer des modification structurale de nos systèmes. Néanmoins, une limitation apparaît lorsque la densité de cobalt est trop élevée : les agrégats ont tendance à *coalescer* à température ambiante, fusionnant pour former des structures plus massives

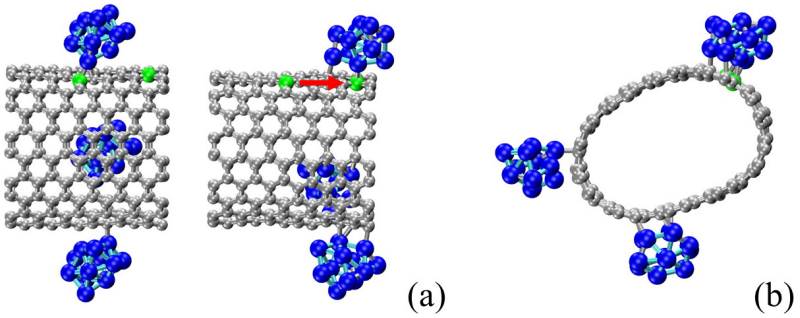

Figure 3. Évolution du nanotube (10,10) décoré avec trois nanoclusters de Co. (a) Déplacement des nanoclusters de Co durant la dynamique NVT. Les atomes de carbone mis en évidence en vert montrent la position initiale de l'un des trois clusters (à gauche), où une liaison chimique C–Co existe, et (à droite) la position déplacée prise par ce même nanocluster de Co après 8,7 ps selon la direction indiquée par la flèche, où une nouvelle liaison chimique C–Co s'est formée avec le site de carbone montré en vert. Le panneau (b) montre un configuration représentatif des déformations radiales subies par le nanotube en raison de la présence des nanoclusters de Co liés à la surface externe et s'y diffusant.

et moins stables. Ces nouveaux agrégats présentent une *mobilité accrue* le long de la surface externe du nanotube, ce qui rend leur comportement difficile à contrôler à l'échelle atomique.

Impact sur les propriétés électroniques et dipolaires

Pour ces systèmes, j'ai mis en œuvre une approche reposant sur la *théorie fluctuation-dissipation* combinée à la *méthode d'entropie maximale* afin d'extraire les spectres de réponse diélectrique. La figure 4 présente les spectres d'absorption infrarouge obtenus pour les trois cas.

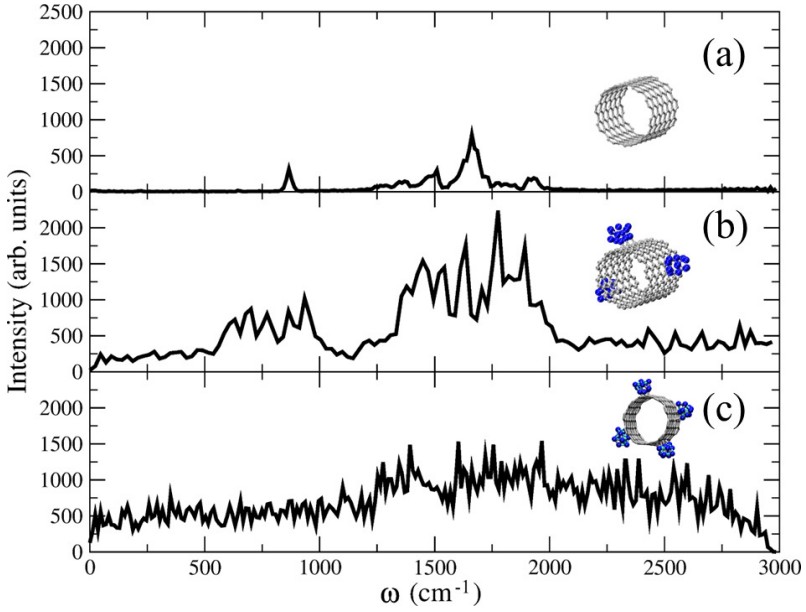

Figure 4. Spectres d'absorption IR simulés pour (a) le nanotube de carbone (10,10), (b) le même nanotube décoré avec trois nanoclusters de Co, et (c) décoré avec quatre nanoclusters de Co. Les figures en encart rappellent graphiquement à quel système correspondant chaque spectre, avec un code couleur gris pour le carbone et bleu pour le cobalt.

L'utilisation de la methode MLWF m'a permis de mettre en évidence une modification de

la distribution spatiale de la densité électronique dans la région des liaisons carbone–cobalt. Cette approche a également révélé une variation locale significative du moment dipolaire autour de ces liaisons. Ces observations sont cohérentes avec les variations observées dans les spectres d'absorption : en effet, l'augmentation du nombre de liaisons C–Co entraîne une perturbation plus marquée du moment dipolaire, ce qui se traduit par une modification plus importante de la réponse optique du système, notamment dans l'absorption électronique.

Enfin, les *limites techniques* de la méthode sont discutées. Bien qu'efficace dans l'infrarouge, son extension à des fréquences plus basses (notamment dans le domaine des micro-ondes) reste aujourd'hui restreinte, en raison du caractère intensif en temps des calculs nécessaires. Le déplacement des cobalts modifie fortement le moment dipolaire local, ce qui influence les propriétés d'absorption.

Système 2 : CNT en interaction avec le PMMA

Dans la deuxième partie de cette thèse, une collaboration a été établie avec une équipe expérimentale travaillant sur l'absorption électromagnétique dans la gamme des micro-ondes de nanocomposites à base de carbone. Ces matériaux suscitent un intérêt croissant en raison de leur excellente résistance à la corrosion et de leurs performances thermiques, mécaniques et diélectriques remarquables.

Afin d'établir un lien direct avec les systèmes expérimentaux, les simulations ont été réorientées vers des structures plus réalistes, composées de nanotubes de carbone (NTC) intégrés dans une matrice polymère de type poly(méthacrylate de méthyle) (PMMA). Diverses configurations ont été explorées : variation du nombre de NTC, modification de la taille de la boîte de simulation et donc des effets périodiques, changement de l'angle d'orientation entre les NTC, ou encore introduction de défauts structuraux (lacunes). Un système stable a été obtenu, composé de deux NTC espacés de 3,4 à 6 Å, reproduisant une situation physiquement réaliste.

Afin d'évaluer l'effet du polymère sur les propriétés dynamiques et diélectriques du système, des chaînes de PMMA ont été introduites. Les simulations ont été initialement effectuées

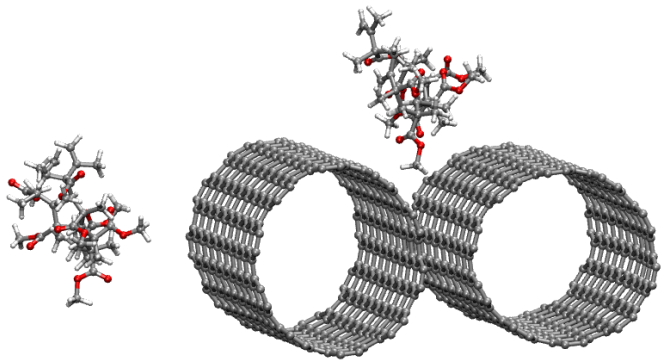

Figure 5. Système simulé composé de deux nanotubes de carbone (10,10) de 400 atomes de carbone chacun, en interaction à une distance de 5 Å, portant deux chaînes de polymère PMMA : l'une dans l'espace interstitiel entre les deux CNTs et l'autre sur le côté, où le système est répliqué périodiquement.

sur le cluster CAIUS, puis étendues sur le supercalculateur TGCC IRENE (CEA) pour le systèmes plus complexes de CNT+PMMA.

Effets structuraux collectifs

Les simulations ont révélé que, tandis que le CNT isolé conserve une structure stable et symétrique, l'ajout d'interactions, soit entre CNTs, soit avec le PMMA, induit des déformations structurelles notables, en particulier une ovalisation périodique de la section des nanotubes. Ces déformations traduisent une réponse collective de la structure à l'environnement local.

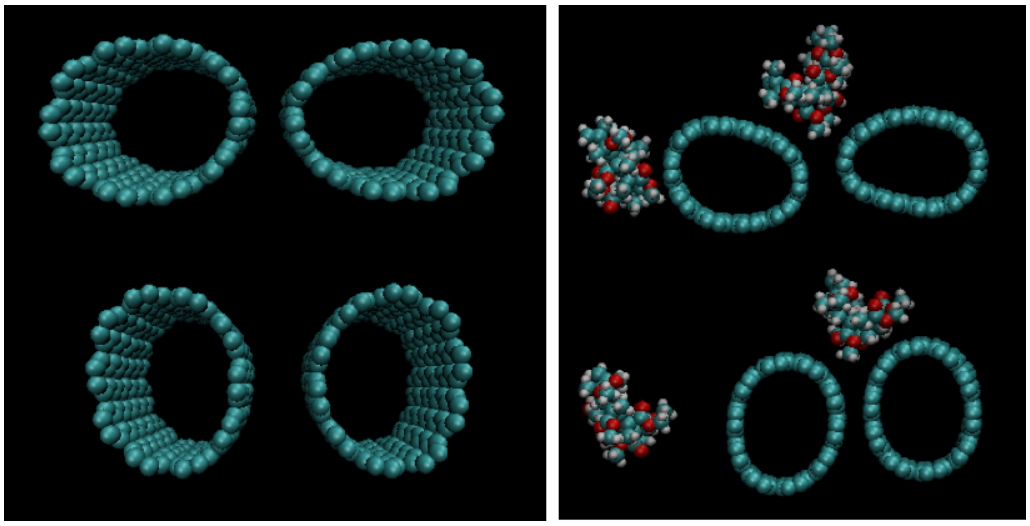

Figure 6. Déformation structurale se produisant au cours de la dynamique lorsque deux CNTs sont suffisamment proches pour être considérés comme en interaction, au sens défini dans le texte. Le panneau de gauche illustre ce phénomène pour deux CNTs proches. Le panneau de droite montre le même phénomène se produisant pour des CNTs en présence de PMMA.

Sur le plan de la variation des distance entre Carbone au sein de la structure, l'introduction d'interactions modifie la dynamique interne des systèmes. Des modes spécifiques apparaissent dans les systèmes couplés, témoignant d'un couplage mécanique et électromagnétique entre les composants. Le PMMA, loin de jouer un rôle passif, contribue à modifier significativement le paysage fréquentiel, notamment en renforçant les contributions à basses fréquences. Cette redistribution spectrale est prometteuse dans la perspective de l'ingénierie de l'absorption dans le domaine micro-ondes.
Ces résultats mettent en évidence le rôle crucial des interactions intermoléculaires dans la modulation des propriétés dynamiques et interatomique des nanotubes de carbone, ouvrant des perspectives pour la conception de matériaux composites aux propriétés électromagnétiques ajustables.

Modes vibratoires modifiés

Grâce aux matrices dynamiques, des visualisations des modes ont révélé une modulation importante des phonons optiques.
D'abord, le spectre d'un nanotube de carbone (CNT) isolé montre les principales caractéristiques attendues, en particulier un pic large au-dessus de 1600 cm^{-1} (Figure 7). Ensuite, l'interaction entre CNT est testé, en comparant plusieurs tailles de systèmes CNT–CNT, on observe que :

- le temps de calcul augmente rapidement avec la taille (loi cubique),
- mais la fréquence vibrationnelle minimale ne suit pas la même tendance : le système optimal (deux CNT de 240 atomes) atteint la valeur la plus basse ($\sim$226 cm^{-1}).

L'analyse des modes montre que les interactions inter-tubes génèrent de nouveaux modes à basse fréquence, absents dans les CNT isolés. Ces modes résultent de mouvements collectifs, et sont localisés selon des schémas spatiaux spécifiques identifiables via les vecteurs propres. Afin d'avoir un représentation des differentes interaction au sein du composite,

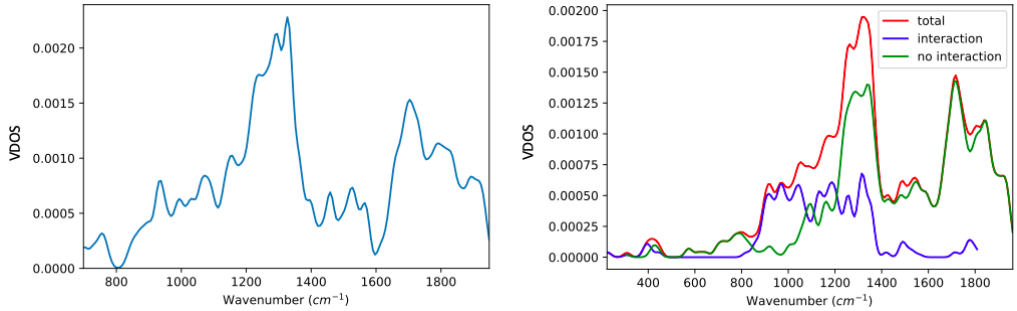

Figure 7. Panneau de gauche : densité d'états vibrationnels (VDOS) d'un nanotube de carbone (CNT) individuel obtenue à partir de l'analyse vibrationnelle réalisée sur un CNT (10,10) composé de 240 atomes. Panneau de droite : VDOS de trois systèmes composés de deux CNTs alignés, de même chiralité et de même taille. La courbe rouge représente le spectre global. Les courbes bleue et verte montrent respectivement les contributions au spectre global provenant des atomes en interaction entre les deux CNTs, et de ceux qui n'interagissent pas, comme discuté dans le texte.

trois configurations ont, pour finir, été étudiées :

1. forte interaction CNT–CNT + PMMA proche,
2. faible interaction CNT–CNT + PMMA plus éloigné,
3. interaction simple entre un seul CNT et le PMMA.

Les résultats montrent clairement que la proximité du PMMA induit de nouveaux modes vibrationnels à basse fréquence, en particulier dans les configurations fortement interactives (fréquence minimale jusqu'à $\sim$29 cm^{-1}). Plus l'interaction est forte, plus la densité d'états vibrationnels à basse fréquence augmente.
Cette modification spectrale résulte de couplages entre les atomes des CNT et du polymère, affectant la dynamique collective du système. À l'inverse, un CNT seul avec du PMMA présente un spectre plus proche de celui d'un CNT isolé.
Donc, les interactions CNT–CNT et CNT–PMMA influencent fortement la réponse vibrationnelle, en particulier dans le domaine des basses fréquences, crucial pour les applications en absorption micro-ondes. Ces effets peuvent être modulés par des paramètres expérimentaux comme la densité du polymère ou la concentration en nanotubes.

Système 3 : Graphène oxyde réduit (rGO)

Dans ce chapitre, nous avons entrepris une série de calculs exploratoires en appliquant les mêmes méthodologies et protocoles développés dans les chapitres précédents, mais en les étendant aux matériaux bidimensionnels à base de carbone, en lieu et place des nanotubes de carbone (CNT). Cette nouvelle orientation, motivée par des considérations expérimentales suggérées par notre collaborateur, vise à explorer des alternatives simples à synthétiser et à contrôler aux composites à base de CNT, tout en conservant des performances compatibles avec les applications dans la gamme des micro-ondes, qui constituent le fil conducteur de ce travail de doctorat.

Si, dans un premier temps, on s'interresse aux effets de taille et à la contrainte appliqué au graphène pour imiter un empillement de graphène, le coeur de se chapitre se situt lors de

l'étude des oxyde de graphènes réduit C376O2 et C375O2 qui sont comparé au graphène pristine de 378 atomes de carbone restrained, ses modifications sont montré Figure 8 .

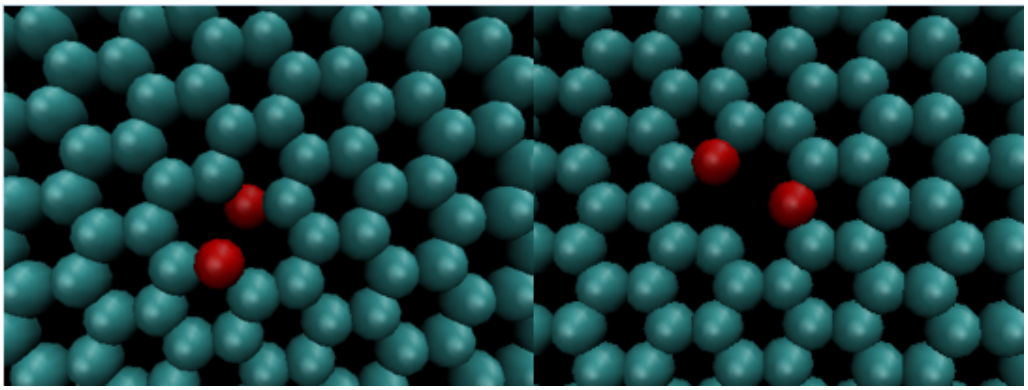

Figure 8. Structure atomique des deux types de défauts étudiés dans le graphène réduit simulé. Le panneau de gauche montre deux atomes d'oxygène (en rouge) remplaçant deux atomes de carbone. En conséquence, l'un des deux atomes d'oxygène sort du plan de la figure (celui qui est le moins masqué par ses voisins dans cette vue), tandis que l'autre passe légèrement en dessous du plan, apparaissant partiellement masqué par les atomes de carbone voisins dans ce schéma. Le panneau de droite montre une vacance de carbone dans laquelle deux atomes de carbone sont remplacés par des atomes d'oxygène situés aux bords de l'espace vide laissé par l'atome de carbone supprimé

effets structuraux

Lorsque deux atomes d'oxygène remplacent deux carbones adjacents (C376O2), la répulsion entre leurs doublets non liants les pousse à sortir du plan du graphène, l'un vers le haut, l'autre vers le bas. Cette configuration minimise l'énergie électrostatique mais induit une déformation permanente et localisée du réseau. Des variations significatives des longueurs de liaison et des angles sont observées autour des sites substitués, bien que la planéité moyenne soit globalement conservée, sur le reste de la structure.

En revanche, lorsque cette substitution est réalisée à proximité d'une vacance monoatomique de carbone (C375O2), les déformations sont plus faibles. L'espace créé par la vacance atténue les interactions répulsives entre oxygènes, réduisant leur déplacement hors-plan et leurs effets structuraux. Les angles et longueurs de liaison restent plus proches des valeurs idéales du graphène, avec une géométrie locale globalement mieux préservée. Les fluctuations dynamiques sont également moindres, et la courbure moyenne reste proche de celle du matériau initial.

Conséquences électroniques

Sur le plan vibrationnel, le spectre de densité d'états (VDOS) montre que le système C375O2 reste très proche du graphène pur, tandis que le système C376O2 présente une intensité accrue à basse fréquence et un déplacement des pics principaux vers les hautes fréquences. Cette différence s'explique par les déformations locales plus marquées dans C376O2, où la répulsion entre O pousse les atomes hors du plan, contrairement à C375O2 où la vacance libère de l'espace et limite les distorsions.
D'un point de vue électronique, l'analyse du moment dipolaire local confirme ces tendances. Dans le graphène pur, la distribution est étroite et centrée (82 D). Dans C376O2, l'introduction d'atomes d'oxygène crée un doublet de pics, signe d'une légère perturbation électronique. En revanche, dans C375O2, le dipôle moyen augmente nettement, avec une large distribution allant jusqu'à 142 D. Cette variabilité témoigne d'un com-

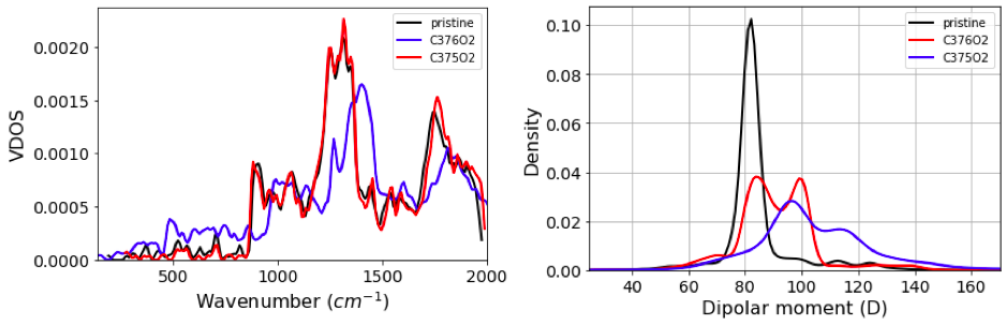

Figure 9. À gauche, la densité d'états vibratoires (VDOS) des trois systèmes. À droite, la distribution de la valeur absolue du moment dipolaire. La courbe noire correspond au graphène parfait, la courbe rouge au système C376O2, et la courbe bleue au système C375O2.

portement électronique plus riche et dynamique, potentiellement favorable à l'absorption électromagnétique.

En résumé, l'ajout d'oxygène seul induit des distorsions structurales notables mais un effet électronique limité, alors que sa combinaison avec une vacance de carbone modifie significativement la réponse électronique du graphène. Cela ouvre des perspectives pour le dopage et l'ingénierie de matériaux à base de carbone dans le cadre d'applications électromagnétiques.